Electronic Supplementary Material (ESI) for Catalysis Science & Technology.

Understanding W/H-ZSM-5 Catalysts for the Dehydroaromatization of Methane

SUPPORTING INFORMATION

*Mustafa Çağlayan[§], Abdallah Nassereddine[†], Stefan-Adrian F. Nastase[Δ], Antonio Aguilar-Tapia[©], Alla Dikhtiarenko[§], Sang-Ho Chung[⁋], Genrikh Shterk[§], Tuiana Shoinkhorova[§], Jean-Louis Hazemann[†], Javier Ruiz-Martinez[⁋], Luigi Cavallo[Δ], Samy Ould-Chikh[Δ], Jorge Gascon[§]**

[§] KAUST Catalysis Center (KCC), Advanced Catalytic Materials, King Abdullah University of Science and Technology (KAUST), Thuwal 23955 (Saudi Arabia)

[†] Institut Néel, UPR 2940 CNRS - Université Grenoble Alpes, Grenoble F-38000 (France)

[Δ] KAUST Catalysis Center (KCC), King Abdullah University of Science and Technology (KAUST), Thuwal 23955 (Saudi Arabia)

[©] Institut de Chimie Moléculaire de Grenoble, UAR2607 CNRS Université Grenoble Alpes, Grenoble F-38000 (France)

[⁋] KAUST Catalysis Center (KCC), Catalysis Nanomaterials and Spectroscopy, King Abdullah University of Science and Technology (KAUST), Thuwal 23955 (Saudi Arabia)

***Corresponding Author:** jorge.gascon@kaust.edu.sa

S1. EXPERIMENTAL PROCEDURES

S1.1. Catalyst Preparation: First, commercially available (ACS Materials) nano-sized ZSM-5 (SiO_2/Al_2O_3=26) was calcined at 550 °C to convert NH_4-ZSM-5 to H-ZSM-5. Before the incipient wetness impregnation (IWI), the calcined zeolite was placed in the vacuum oven at 100 °C for overnight. Then, incipient wetness impregnation was applied to obtain Mo/H-ZSM-5 and W/H-ZSM-5 by using $(NH_4)_6Mo_7O_{24}{\bullet}4H_2O$ (Alfa Aesar) and $(NH_4)_6H_2W_{12}O_{40}{\bullet}xH_2O$ (Sigma-Aldrich) as a Mo precursor and a W precursor, respectively. The impregnated H-ZSM-5 was dried at 100 °C under vacuum and then calcined at 550 °C for 7 hours.

S1.2. Catalyst Characterization: The bulk chemical composition analysis was carried out on an Agilent 5110 ICP-OES, after the samples were digested in acidic solution containing HCl, HNO_3 and HF with the help of Milestone Ethos One Microwave Digestion System.

The textural properties were analyzed by N_2 physisorption, performed at 77 K with a Micromeritics ASAP 2420 high throughput analysis system. Prior to the physisorption measurements, the samples were degassed at 350 °C and 90 °C for 8 and 2 hours, respectively.

Powder X-ray diffraction (PXRD) patterns were acquired on Bruker D8 Advance X-ray diffractometer using Cu-Kα (1.54060 Å) radiation and operated at 40 kV and 40 mA. In order to optimize the count statistics and peak shape profiles, data collection was carried out in the 2θ range of 5–90° using with the step size of 0.03° and scan speed of 7 s/step, and applying low-angle cutting knife to avoid direct beam heating the detector. Le Bail refinements were carried out with FullProf Suite software package[1] using orthorhombic *Pnma* crystallographic model for MFI zeolite.

XPS studies were carried out in a Kratos Axis Ultra DLD spectrometer (Kratos Analytical Ltd) equipped with a monochromatic AlKα x-ray source (hν = 1486.6 eV) operating at 150 W, an acquisition of spectra was performed under an ultra-high vacuum condition (10^{-8} – 10^{-9} mbar). Measurements were carried out in hybrid mode using electrostatic and magnetic lenses. The high-resolution spectra were collected at fixed analyzer pass energy 20 eV. Charge neutralization with low energy electrons was applied for all samples. Spectrum line of C1s (285.2 eV for sp^3 carbon species) was used for a binding energy correction. Typically, powder samples was immobilized on the Cu conductive tape (SPI supplies, Structure Probe, Inc.), placed on the sample holder and evacuated overnight until ultra-high vacuum was reached.

Raman spectra were recorded using a confocal Raman microscope WITec Apyron equipped with 473 nm laser line. The maximum power of the laser line used was 25 mW.

The acidity of fresh catalysts was analyzed by NH_3-TPD experiments. These measurements were performed with a Micrometrics ASAP 2920 unit equipped with TCD. Each sample was treated at 100 °C and 550 °C sequentially under Argon flow prior to the ammonia adsorption at 120 °C. After the samples were saturated with NH_3, they were kept at 140 °C to remove physisorbed NH_3 molecules under Ar flow as well. Then, the temperature was increased to 750 °C with a rate of 10 °C/min.

High-angle annular dark-field (HAADF) imaging is performed on a Thermo Fisher Scientific (TFS) Themis Z aberration-corrected scanning transmission electron microscope (STEM) operated at 300 kV. To minimize the electron beam-induced damage to the structure of metallozeolite, the current of the electron probe is set to 20 pA. The convergence semi-angle of 21 mrad and the collection semi-angle of 31-187 mrad , and a pixel time of 1us is used during the HAADF imaging.

Thermogravimetric tests were performed on a Mettler Toledo 1 STAR System. The test conditions were as follows: Prior to the combustion, the samples (ca. 5 mg) were stripped under a N_2 flow (20 mL min^{-1}) for removal of the adsorbed species increasing temperature up to 750 ^{o}C at a 10 ^{o}C min^{-1} rate. Upon that, the temperature decreased to 200 ^{o}C, the gas was switched to dry air flow (20 mL min^{-1}) and stabilized for 15 min. Subsequently, coke combustion was conducted by increasing temperature up to 850 ^{o}C at a 10 ^{o}C min^{-1} rate and then maintaining an isotherm for 15 min to ensure complete coke combustion.

Transmission FTIR spectroscopy using pyridine as a probe molecule was performed on a Nicolet 6700 spectrometer with a DTGS detector. The pellet with a diameter of 0.85 cm was prepared from the sample of interest and activated in vacuum at 350 °C for 1 h to evacuate adsorbed species. Upon activation, the pellet was saturated with pyridine vapor and evacuated at 150 °C for 30 min and 350 °C for 30 min sequentially. Spectra were recorded in 1000–4000 cm^{-1} wavenumber range with a resolution of 4 cm^{-1} and merged from 64 scans. The area of Brønsted (BAS) and Lewis (LAS) acid sites was derived from the bands situated at 1546, 1456, and 1448 cm^{-1}, as described elsewhere using extinction coefficients of 1.67 and 2.22, respectively.[2,3] Counting that one molecule of pyridine is adsorbed on one acid site, following equations were used to calculate the concentration of Brønsted and Lewis acid sites (C_{BAS} and C_{LAS}):

$$C_{BAS} = \frac{1.88 \times I_A(B) \times R^2}{W}$$

$$C_{BAS} = \frac{1.42 \times I_A(L) \times R^2}{W}$$

where $I_{\mathrm{A}}(B, L)$ is the integrated absorbance of BAS or LAS band (cm^{-1}), R is the radius of the pellet (cm), and W is the mass of the catalyst (mg).

Solid-state nuclear magnetic resonance (ssNMR) experiments were carried out on a Bruker 21.1 T wide-bore magnet with Avance III spectrometer using a 3.2 mm triple channel probe. The one pulse ^{27}Al MAS NMR spectra were recorded using 6 kHz π/6 pulse and a recycle delay of 0.5 s. The spectra were accumulated from 6144 scans. The one pulse ^{29}Si MAS NMR spectra were recorded using 51 kHz π/2 pulse and a recycle delay of 20 s. The spectra were accumulated from 2560 scans. Typically, the sample was spun using dry nitrogen at a magic angle spinning (MAS) rate of 20 kHz.

UV-Vis diffuse reflectance spectra (UV-vis DRS) were recorded using a JASCO V-670 spectrophotometer in 200-800 nm range with halogen and deuterium lamps as light sources. $BaSO_4$ and bare ZSM-5 were used as backgrounds.

The DRIFT-IR measurements were carried out on a Nicolet 6700 spectrometer equipped with a MCT detector using a Praying Mantis DRIFT cell attachment (Harrick Scientific Products). The samples were first treated at 350 °C under continuous He flow (50 ml/min) measured for 1 h to remove water and all volatile compounds. After the sample temperature was lowered to 150 °C, the spectra were recorded in 750–4000 cm^{-1} wavenumber range with a resolution of 4 cm^{-1} and merged from 64 scans.

S1.3. Catalytic Activity Test: The catalytic performance tests were carried out in a fixed bed reactor setup manufactured by PID Eng & Tech. 250 mg pelletized, crushed, and sieved catalyst particles (212-425 µm) loaded in a quartz tube reactor (internal diameter 8 mm) were tested at atmospheric pressure. Nitrogen as an internal standard was fed to reactor with ratios CH_4/N_2=15 ($cm^3.min^{-1}$) /2 ($cm^3.min^{-1}$) feed ratio (WHSV: 2.58 h^{-1}). In the case of reaction regeneration cycles, after the 6-h MDA reaction at 750 °C, samples were regenerated at 700 °C under continuous dry air flow (ca. 15 $cm^3.min^{-1}$ at STP) for 5 h. The gas phase product mixture was analyzed online with an Agilent 7890-B GC equipped with FID and TCD. The carbonaceous product yields, total yield and hydrogen volumetric flow ($cm^3.min^{-1}$) at the outlet were calculated as follows:

$$X_{CH_4} = \frac{F_{CH_4,in} - F_{CH_4,out}}{F_{CH_4,in}} \times 100$$

$$Y_x = \frac{F_{x,out} \times (C\ number\ of\ x)}{F_{CH_4,in}} \times 100$$

$$Y_{total} = \sum_{All\ x\ except\ CO,\ CO_2} Y_x$$

$$F_{H_2,out} = y_{H_2,out} \times F_{total,out}$$

$$TOF_X = \frac{F_{x,out}}{mmoles\ of\ metal\ in\ the\ corresponding\ catalyst}$$

S1.4. X-Ray Absorption Spectroscopy under *Operando* MDA: The structural analysis of the W/ZSM5 catalysts was performed under operando conditions at the CRG-FAME beamline (BM30)[4] in the European Synchrotron Radiation Facility (ESRF) in Grenoble. The ring was operated at 6 GeV with a nominal current of 200 mA in 7/8+1 mode. The beamline is equipped with a liquid-nitrogen-cooled doubled crystal Si(220) monochromator surrounded by two Rh-coated mirrors for harmonic rejection. The beam size on the sample was 210x100 µm (HxV, FWHM). Tungsten L_3-edge spectra were collected in fluorescence mode using a CANBERRA 13-elements Ge solid-state detector. The monochromator was energy calibrated measuring the tungsten L_3 absorption edge using a metallic tungsten foil. First maximum of the first derivative of the absorption W L_3-edge was set at 10207 eV. The XAS cell previously described[5] was modified using a sapphire tube reactor i.d. 5 mm. The effluent gas composition was monitored on-line by an EcoCat-P portable mass spectrometer (ESS).

XAS data were analyzed using the HORAE package, a graphical interface to the AUTOBK and IFEFFIT code.[6] The XANES and EXAFS spectra were obtained after performing respective standard procedures for pre-edge subtraction, normalization, polynomial removal and wave vector conversion. The extracted EXAFS signal were Fourier transformed using a Hanning apodization window (dk =3).

For the MDA operando experiments, XAS characterization was performed according to the following protocol (see Figure S42): First, 100 mg of sieved W/ZSM5 catalyst (212-425 µm) was introduced as a packed bed into the reactor. XAS spectra were recorded under inert gas (10 mL/min of He) at room temperature in order to characterize the initial state of the catalyst. The cell was then heated up to 200 °C at 10 °C/min, followed by a plateau at the same temperature in order to dehydrate the sample. The reaction mixture 88.2% CH_4: 11.8% He was subsequently introduced at a total flow rate of 6.8 mL/min (at STP) and the cell was heated up to 750 °C (10°C/min). XANES spectra were recorded continuously during the heating ramp to observe any changes in the metal oxidation state. Once the differences recorded in a series of XANES spectra were estimated to be negligible at 750 °C, the characterization of the metal nanoparticles was supplemented by the acquisition of EXAFS spectra.

After the reaction, a flow of 10 mL/min of He was introduced at a 750 °C and the cell was cooled down to 200 °C during the purge. Then the sample was regenerated by flowing 6 mL/min (at STP) of dry air at 700 °C during 2h with a ramping rate of 8 °C. EXAFS spectra were recorded during this process. After the regeneration process, the cell was purged with He at 200 °C, and the reaction mixture was introduced to the cell and heated up to 750 °C (10 °C/min) for a new reaction/regeneration cycle.

S2. CATALYSIS RESULTS

S2.1. Activity of 2Mo-Z26:

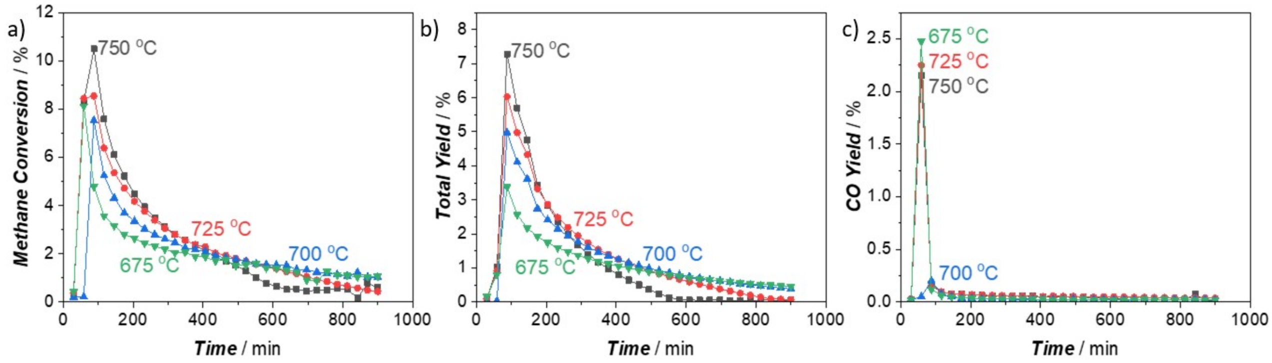

Figure S1. Catalytic activity of 2 Mo-Z26 (2 wt.% Mo/H-ZSM-5 - *250 mg*) at different temperatures: a) Methane Conversion, b) Total Yield (without CO and CO_2), c) CO Yield (Reproduced from our previous publication[7])

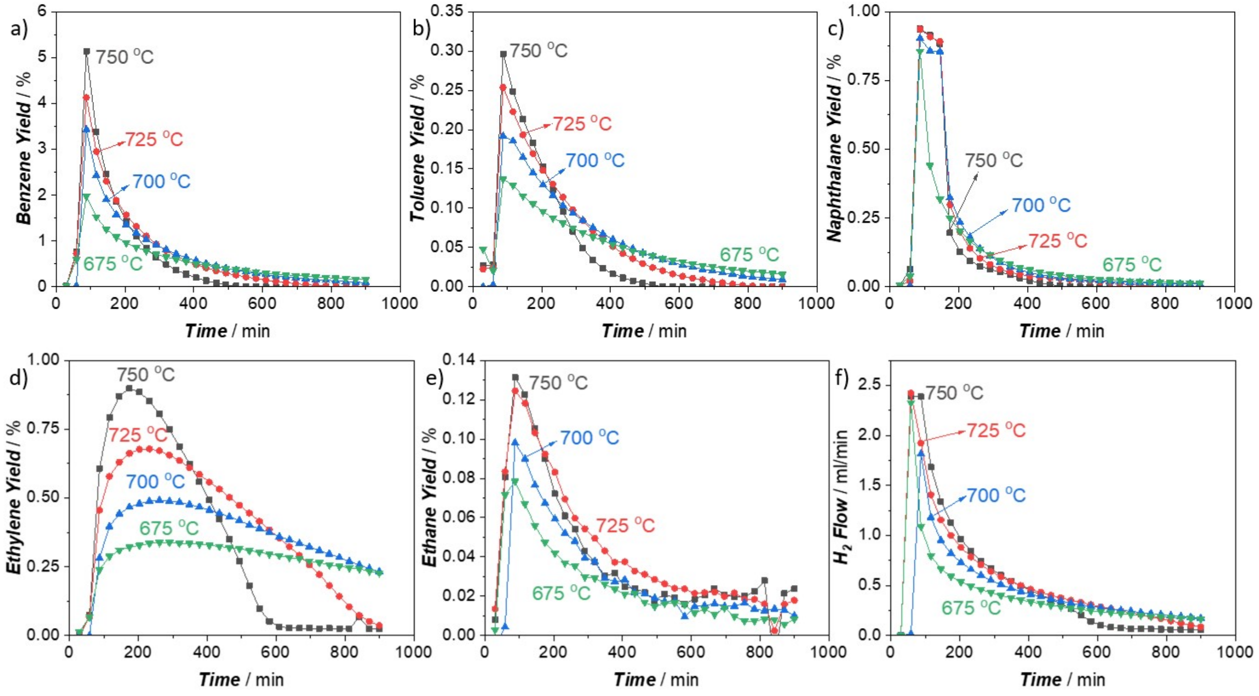

Figure S2. Catalytic activity of 2 Mo-Z26 (2 wt.% Mo/H-ZSM-5 - *250 mg*) at different temperatures: a) Benzene Yield, b) Toluene Yield, c) Naphthalene Yield, d) Ethylene Yield, e) Ethane Yield, and f) H_2 Flow (Reproduced from our previous publication[7])

S2.2. Effects of W Loading on MDA Activity:

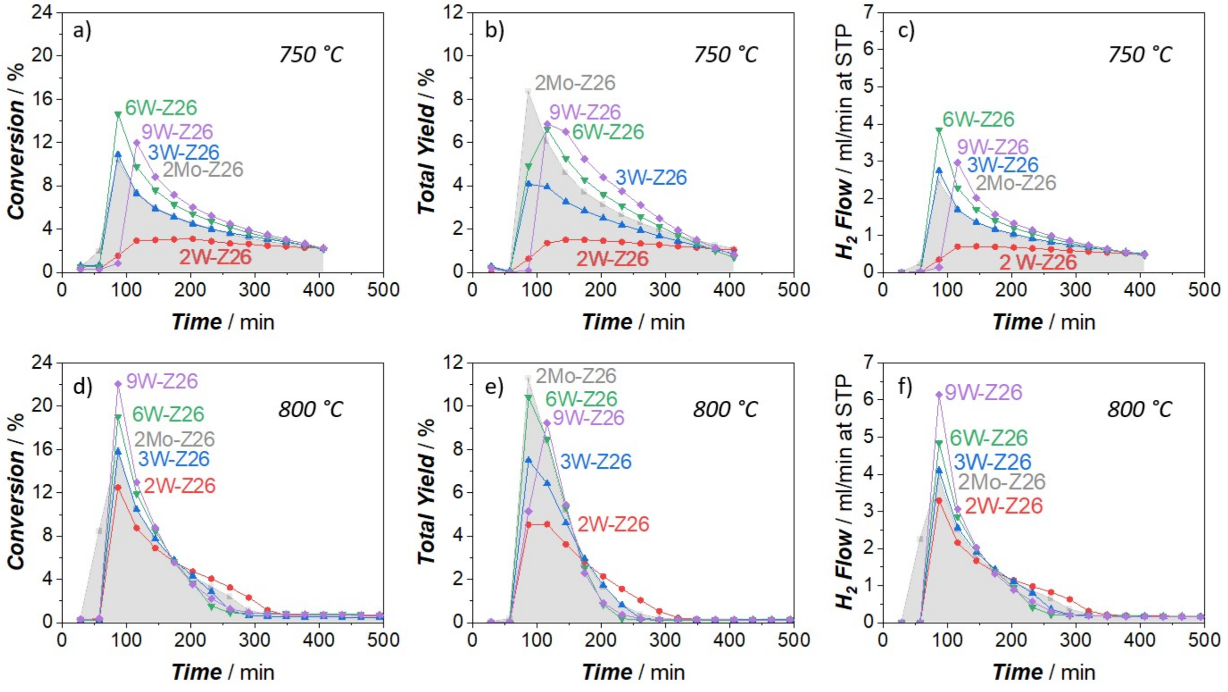

Figure S3. Catalytic activity of the prepared W and Mo catalysts (250 mg) at 750 °C (top: a, b, c) and 800 °C (bottom: d, e, f); a, d: CH_4 Conversion– b, e: Total Yield (without CO and CO_2) – c, f: H_2 Flow (11.8 mol% N_2 and 88.2 mol% CH_4 in the inlet, Total Gas Flow= 17 ml/min at STP)

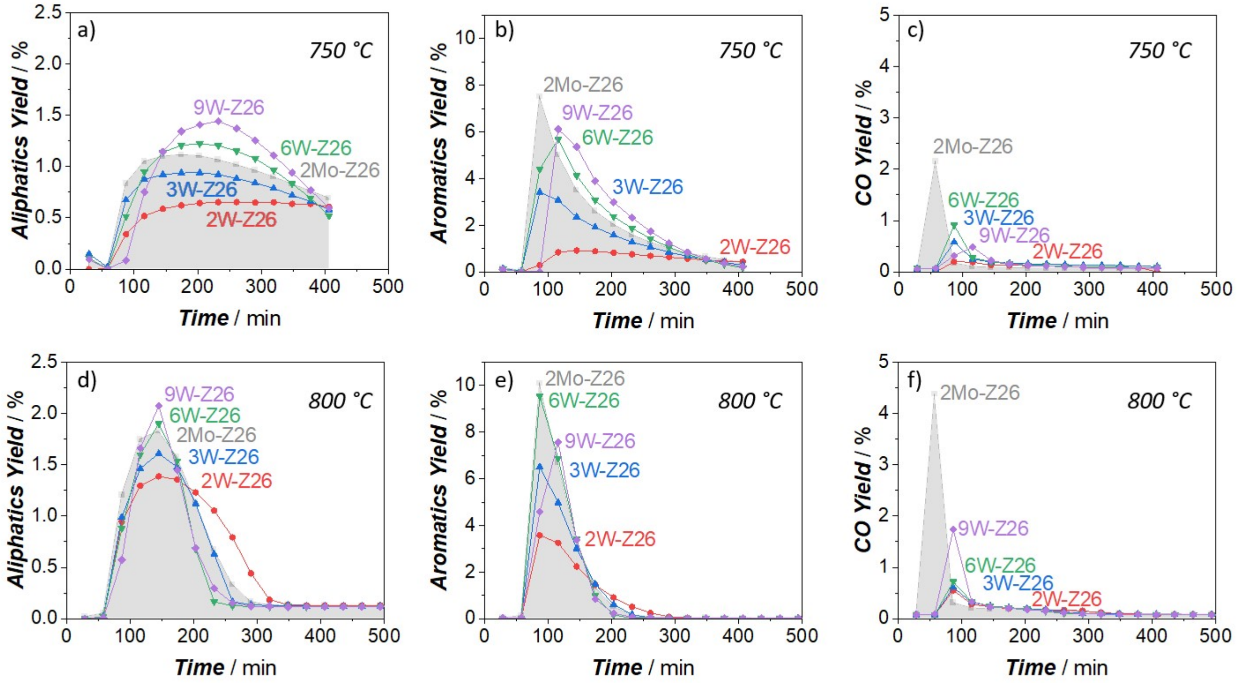

Figure S4. Catalytic activity of the prepared W and Mo catalysts (250 mg) at 750 °C (top: a, b, c) and 800 °C (bottom: d, e, f); a, d: Total Aliphatics Yield – b, e: Total Aromatics Yield – c, f: CO Yield (11.8 mol% N_2 and 88.2 mol% CH_4 in the inlet, Total Gas Flow= 17 ml/min at STP)

S2.3. Reaction-Regeneration Cycles-Original Pathway:

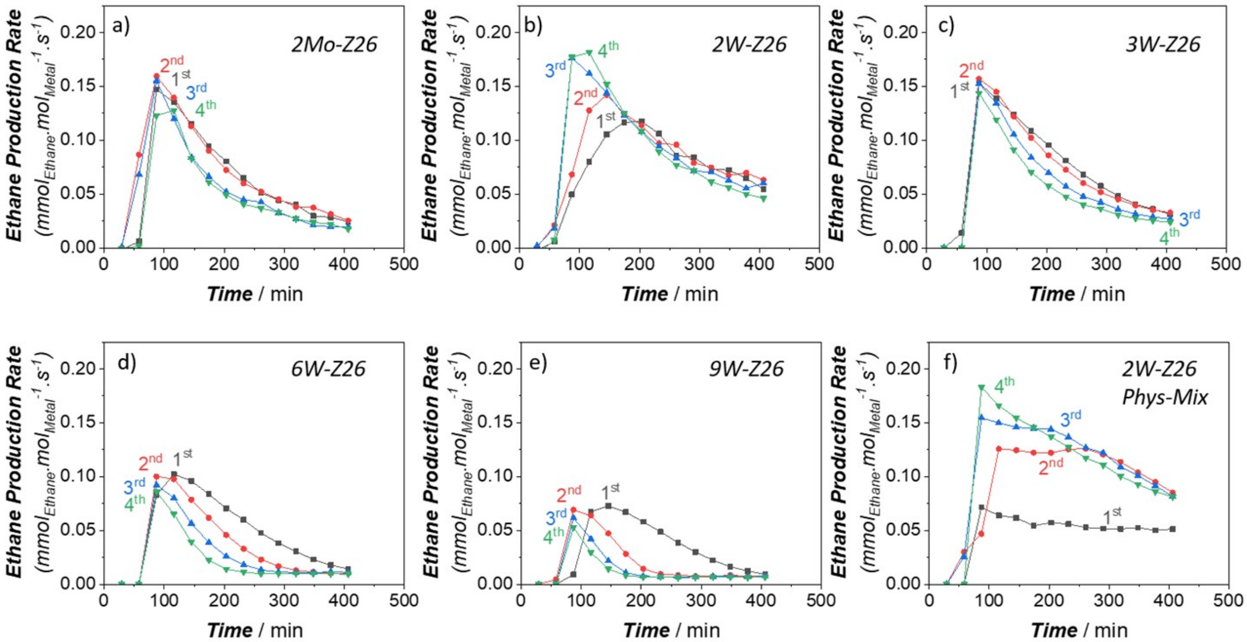

Figure S5. Ethane production rates (TOFs) of the prepared W and Mo catalysts (250 mg) during the reaction-regeneration cycles: a) 2Mo-Z26, b) 2W-Z26, c) 3W-Z26, d) 6W-Z26, e) 9W-Z26, and f) 2W-Z26 Phys-Mix (Reaction at 750 °C: *11.8 mol% N_2 and 88.2 mol% CH_4 in the inlet, Total Gas Flow= 17 ml/min at STP* – Regeneration at 700 °C: *Dry Air Flow= 15 ml/min at STP*)

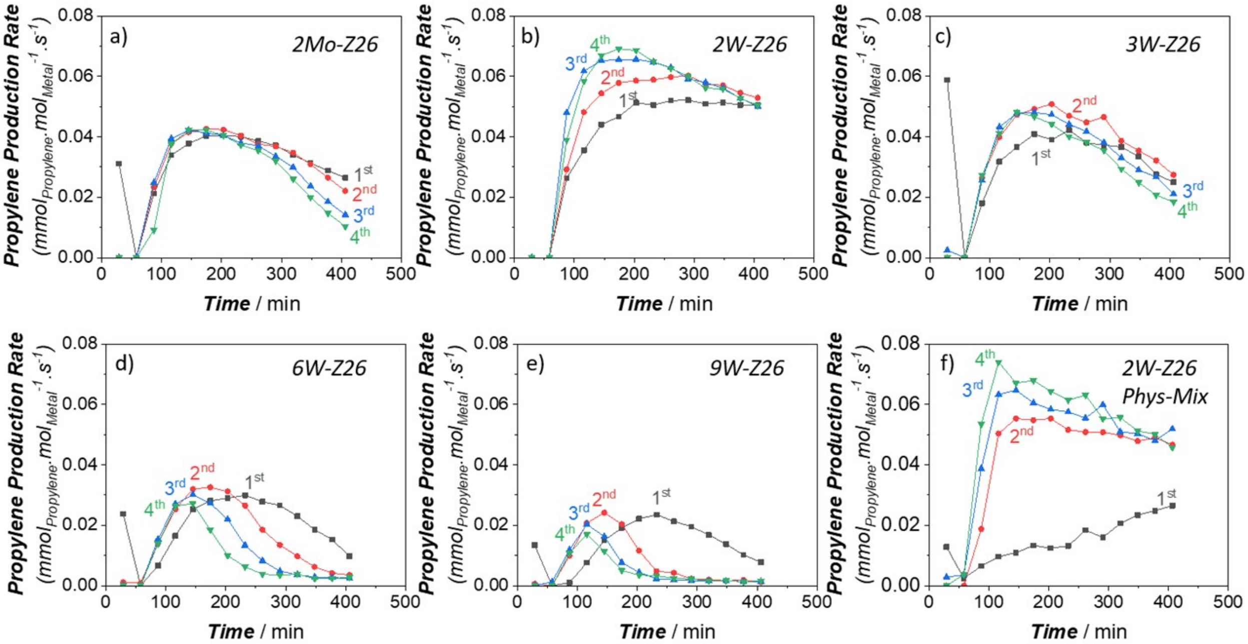

Figure S6. Propylene production rates (TOFs) of the prepared W and Mo catalysts (250 mg) during the reaction-regeneration cycles: a) 2Mo-Z26, b) 2W- Z26, c) 3W-Z26, d) 6W-Z26, e) 9W-Z26, and f) 2W-Z26 Phys-Mix (Reaction at 750 °C: *11.8 mol%* N_2 *and 88.2 mol%* CH_4 *in the inlet, Total Gas Flow= 17 ml/min at STP* – Regeneration at 700 °C: *Dry Air Flow= 15 ml/min at STP*)

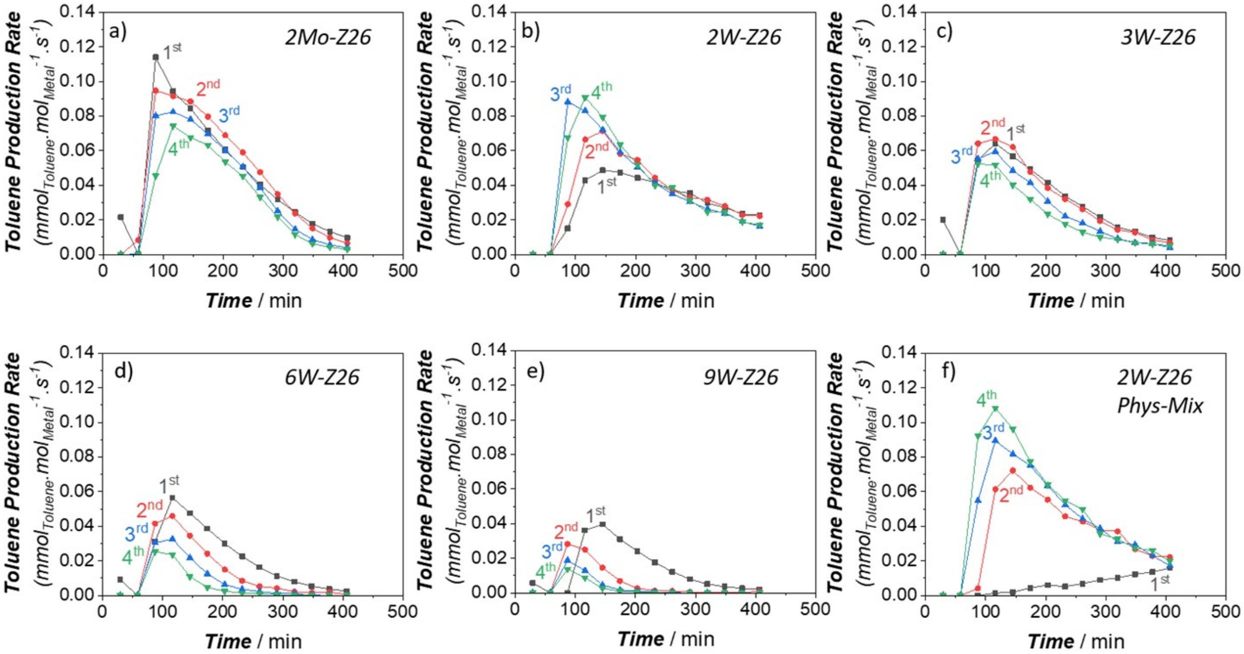

Figure S7. Toluene production rates (TOFs) of the prepared W and Mo catalysts (250 mg) during the reaction-regeneration cycles: a) 2Mo-Z26, b) 2W-Z26, c) 3W-Z26, d) 6W-Z26, e) 9W-Z26, and f) 2W-Z26 Phys-Mix (Reaction at 750 °C: *11.8 mol%* N_2 *and 88.2 mol%* CH_4 *in the inlet, Total Gas Flow= 17 ml/min at STP* – Regeneration at 700 °C: *Dry Air Flow= 15 ml/min at STP*)

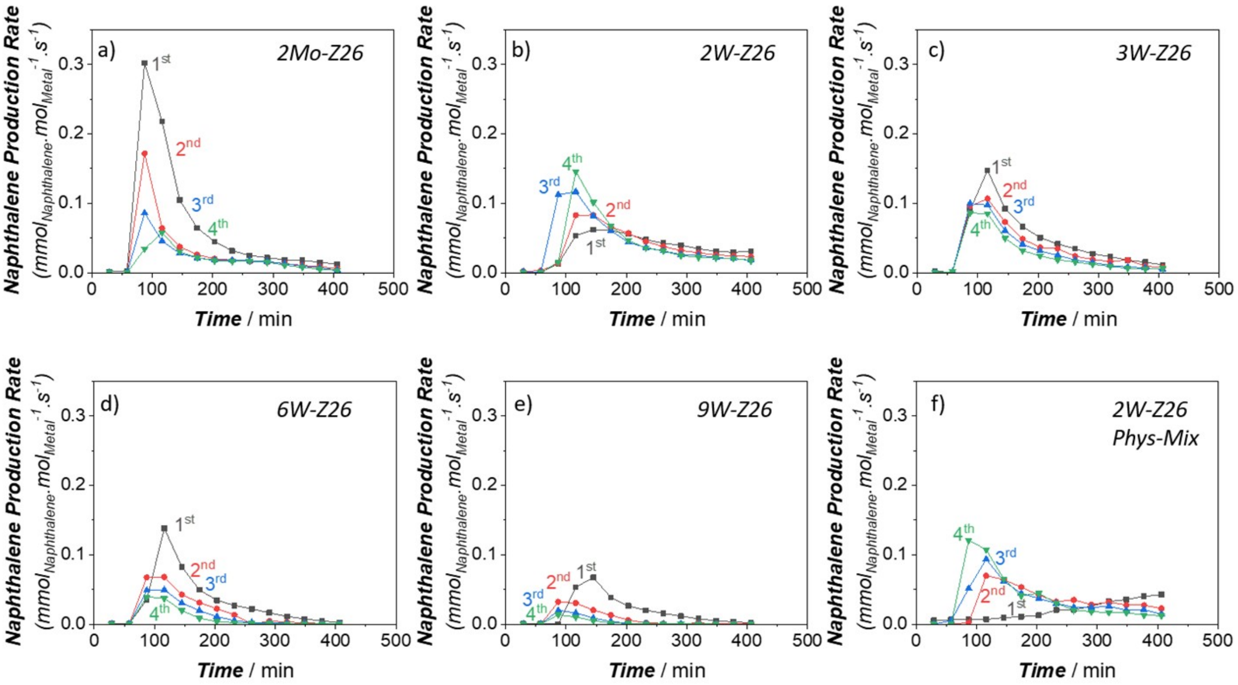

Figure S8. Naphthalene production rates (TOFs) of the prepared W and Mo catalysts (250 mg) during the reaction-regeneration cycles: a) 2Mo-Z26, b) 2W-Z26, c) 3W-Z26, d) 6W-Z26, e) 9W-Z26, and f) 2W-Z26 Phys-Mix (Reaction at 750 °C: *11.8 mol% N_2 and 88.2 mol% CH_4 in the inlet, Total Gas Flow= 17 ml/min at STP* – Regeneration at 700 °C: *Dry Air Flow= 15 ml/min at STP*)

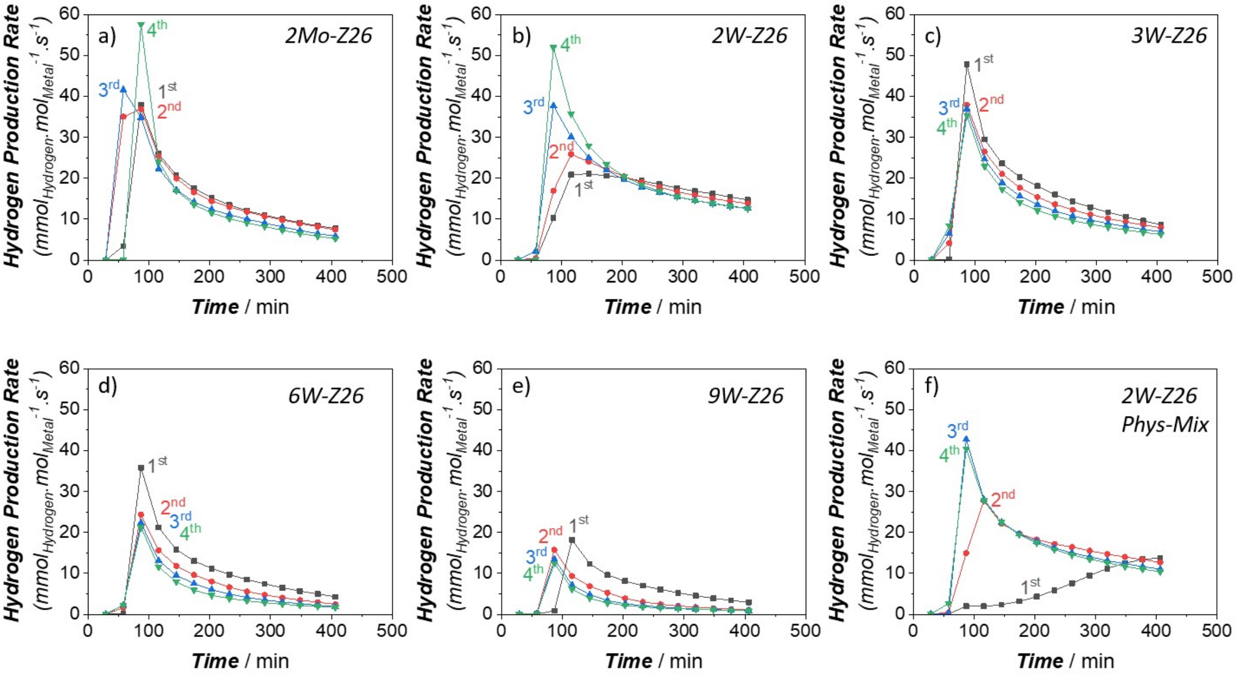

Figure S9. Hydrogen production rates (TOFs) of the prepared W and Mo catalysts (250 mg) during the reaction-regeneration cycles: a) 2Mo-Z26, b) 2W-Z26, c) 3W-Z26, d) 6W-Z26, e) 9W-Z26, and f) 2W-Z26 Phys-Mix (Reaction at 750 °C: *11.8 mol% N_2 and 88.2 mol% CH_4 in the inlet, Total Gas Flow= 17 ml/min at STP* – Regeneration at 700 °C: *Dry Air Flow= 15 ml/min at STP*)

S2.4. Reaction-Regeneration Cycles with 2W-371 and 2W-Z26 pre-calcined at 700 °C

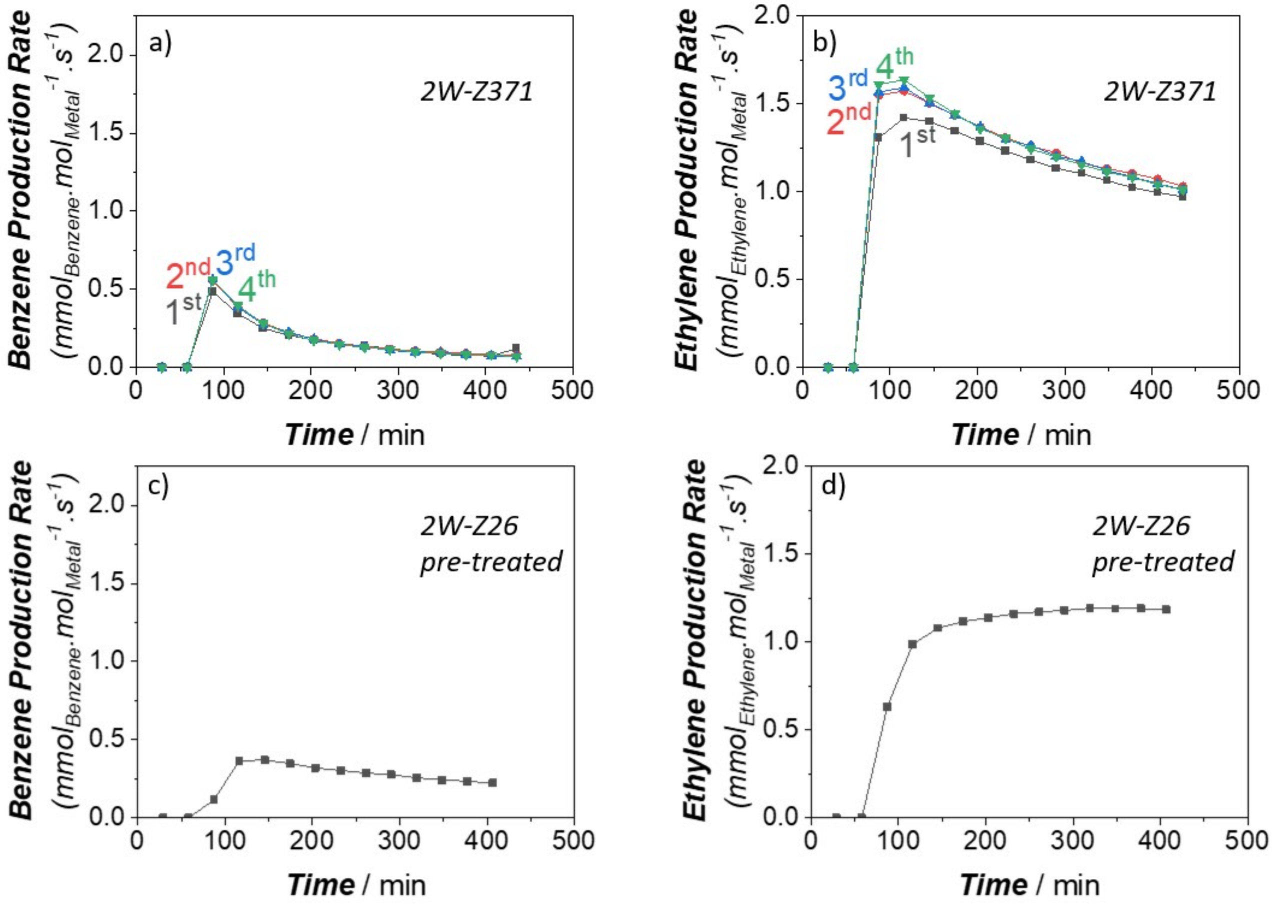

Figure S10. Benzene (a, c) and ethylene (b, d) production rates (TOFs) of the prepared W catalysts (250 mg) during the reaction-regeneration cycles: a, b) 2W- Z371, and c, d) 2W-Z26 pre-calcined at 700 °C for 7-day (Reaction at 750 °C: *11.8 mol% N_2 and 88.2 mol% CH_4 in the inlet, Total Gas Flow= 17 ml/min at STP* – Regeneration at 700 °C: *Dry Air Flow= 15 ml/min at STP*)

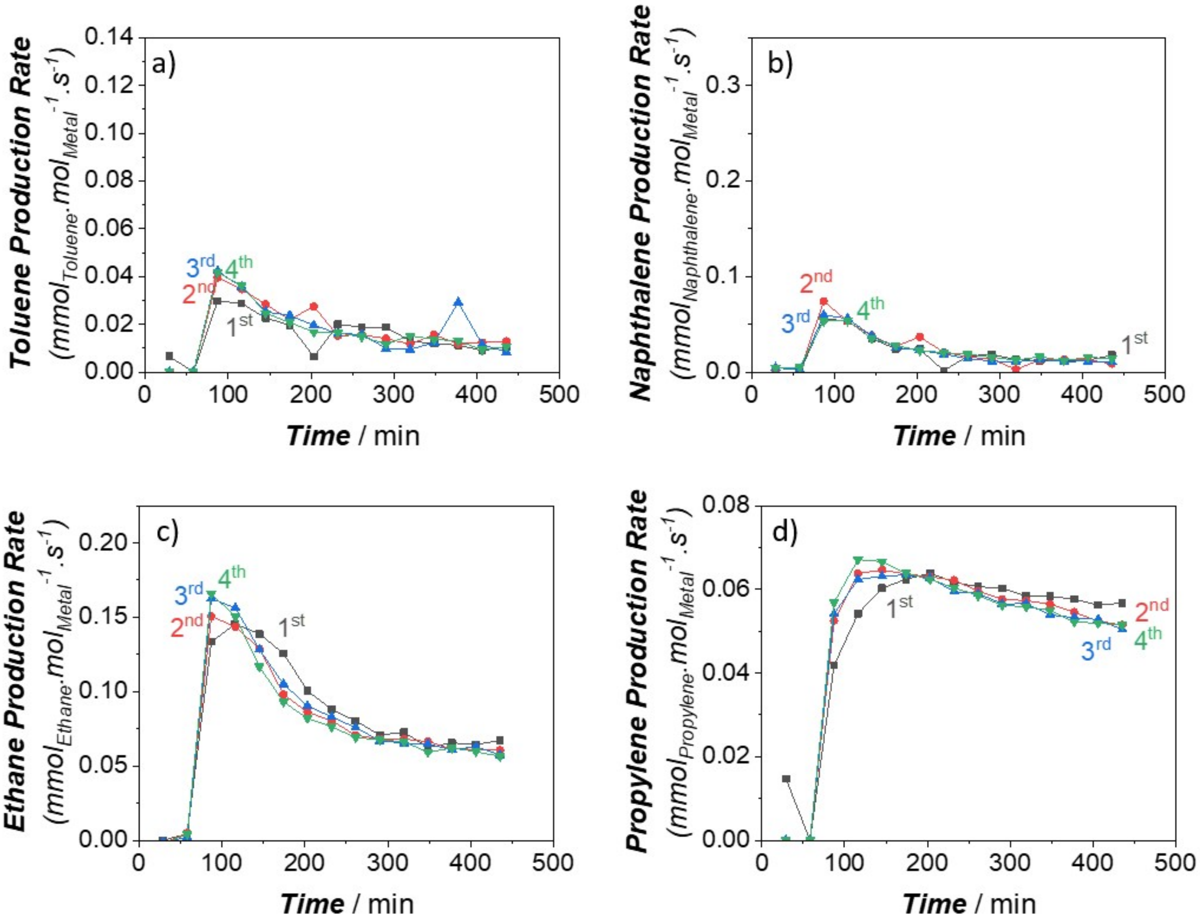

Figure S11. Toluene (a), Naphthalene (b), Ethane (c), and Propylene (d) production rates (TOFs) of 2W-Z371 (250 mg) during the reaction-regeneration cycles: (Reaction at 750 °C: *11.8 mol%* N_2 *and 88.2 mol%* CH_4 *in the inlet, Total Gas Flow= 17 ml/min at STP* – Regeneration at 700 °C: *Dry Air Flow= 15 ml/min at STP*)

S2.5. Changing Parameters in Reaction-Regeneration Cycles:

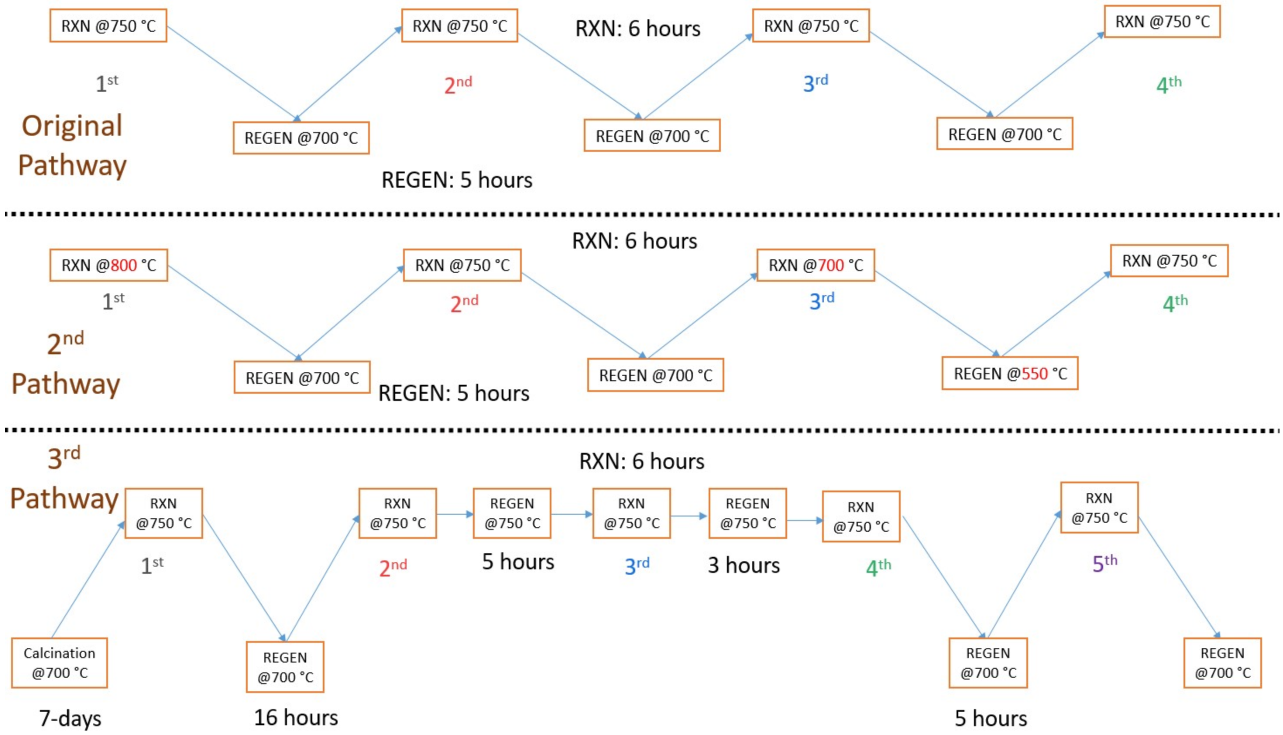

Figure S12. Reaction-Regeneration cycles we followed in this study; three different pathways

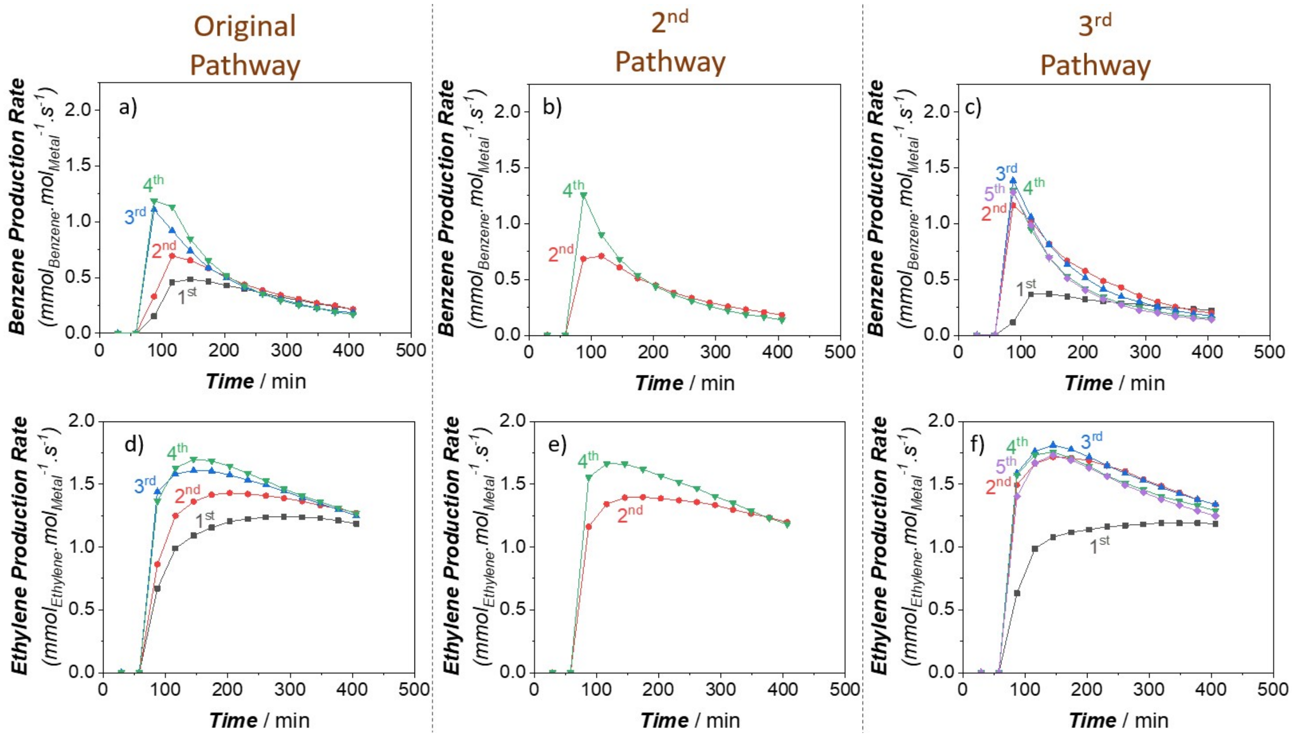

Figure S13. Comparison of 3-pathways: Benzene (a, b, c) and Ethylene (d, e, f) production rates (TOFs) of 2W-Z371 (250 mg) during the reaction-regeneration cycles shown in Figure S12:

(Reaction at 750 °C: 11.8 mol% N_2 and 88.2 mol% CH_4 in the inlet, Total Gas Flow= 17 ml/min at STP – Regeneration: Dry Air Flow= 15 ml/min at STP)

S3. *EX-SITU* CHARACTERIZATIONS

To understand the catalytic activity observed, we examined our W-loaded zeolites with ^{27}Al MAS NMR, PXRD, XPS, N_2 Physisorption, TGA-TPO, DRIFT-IR, UV-Vis DRS, and micro-Raman.

N_2 physisorption analysis (Figures S14a, S15a, and Table S1-S3) revealed a decrease in total pore volume and surface area as the W amount increases, although microporosity is still preserved at the highest loading (ca. 9 wt. %). ^{27}Al MAS NMR (absence of aluminum tungstate species – Figure S31) and PXRD (preserved crystallinity and coherent domain size – Figure S32a and Table S5) analyses support the preservation of the internal structure and crystallinity of the zeolite. We further investigated the dispersion/distribution of W with micro-Raman, UV-Vis DRS, and PXRD. Raman data (Figure S16a and S19a) showed catalysts with W loadings lower than 9 wt. % have mainly ν(O=W=O) stretching (from surface WO_4 species) and ν(W-O-W) stretching at 973 cm^{-1} and 828 cm^{-1}, respectively.[8,9] The observed Raman vibrations could be attributed to the formation of monomeric and polymeric W sites in/on ZSM-5 particles. At 9 wt. % W loading, in addition to the aforementioned vibration modes, the crystalline WO_3-related vibrations (ν(O=W=O) at 811 cm^{-1}, ν(W_2O_6 & W_3O_8) at 717 cm^{-1}, and ν(O-W-O) at 272 cm^{-1}) were detected. However, these crystalline phase vibrations were broader than in the case of bulk WO_3 vibrations, which indicates nanoparticle formation rather than larger particles.[8,9] PXRD patterns are in line with Raman observations: at lower W loadings, no diffraction peaks assigned to crystalline WO_3 or any other W phases could be detected, while the presence of WO_3 could be noticed at higher loadings (Figure S32a).[10] The collected UV-Vis spectra (Figure S20a and Figure S21a) for fresh catalysts were also in line with Raman and PXRD findings. The observed absorption peaks in the range of 200-400 nm could be attributed to mono- and polytungstate structures in/on the zeolite particles.[9] Besides these, XPS spectra (Figure S30a) collected for fresh 2W-Z26 and 6W-Z26 depicted that there are no reduced/carbidic W states as expected. While one-oxidation state (W^{6+}) was observed on 2W-Z26 sample, W^{5+} features were also identified to a small extent on 6W-Z26. These W^{5+} features may play a critical role during the initial stages of MDA reactions (i.e., catalyst activation, generating reactive species) since some studies[11–13] in the literature already showed that W^{5+} has key roles in metathesis, glucose dehydration reactions and catalyst acidity in the case of heterogenous catalysis.

NH_3-TPD analysis (see Table 2, Figure S26) revealed the loss of some acid sites upon 2 wt. % W loading, especially the strong ones. This could be explained by the anchoring of W cations on bridging oxygen sites between framework Al^{3+} and Si^{4+} atoms (i.e., Al-O^--Si). However, this trend seems to be reversed at higher loadings. This implies that some tungsten sites provide some acidity. The decrease of acidity in the case of 9W-Z26 could be associated with accessibility (i.e., nano-sized crystalline WO_3 blocks pore entrances, and low dispersion of WO_x). It is well known that supported WO_x can act as an acid.[14–17] The amount of W, dispersion-distribution, and support type are critical factors defining the W acidity. For instance, when Wachs et al.[15] studied supported (Al_2O_3, Nb_2O_5, TiO_2, and ZrO_2) tungsten oxide catalysts for *methanol-to-dimethylether-dehydration* reaction, they found out that surface WO_x species are less active (less acidic) compared to crystalline WO_3 particles for all supports except Al_2O_3 (which shows the opposite trend). They suggested a correlation between site acidity and electron density of the bridging W-O-Support bonding (i.e., as support (X) cation electronegativity increases, electron density of bridging W-O-X decreases and acidity increases). Also, the support interaction may heavily influence the dispersion of W in some cases. For instance, it is known that W-SiO_2 interaction is very weak compared to W-Al_2O_3, and this could lead to bigger particles (i.e., polytungstates and aggregated crystalline WO_3) compared to highly dispersed species (i.e., isolated tetrahedral) on alumina supports.[15,17] Eventually, the dispersion results in changes in W reduction. For example, it is more demanding to reduce tungsten sites on alumina than tungsten sites on silica support via H_2.[17]

Considering these, we can state that there is a critical relation between tungsten dispersion-distribution (in other words, acidity) and MDA activity at 750 °C. At higher loadings (>2 wt. %), there is a high probability of forming WO_x sites attached to silanol groups and located on the external surface. Therefore, these could be easily activated/reduced in comparison to other tungsten sites located inside the pores. Similar examples could be found in the literature. For instance, Ding and colleagues[18] investigated various tungsten oxide-impregnated catalyst supports (SiO_2, γ-Al_2O_3, SiO_2-Al_2O_3, silica modified γ-Al_2O_3) for 1-butene metathesis. They found that silica modification leads to the moderate aggregation of WO_x on alumina, which is way more active than highly dispersed and large aggregated sites on other supports at 453 K. Furthermore, it is clear that the dispersion-distribution of W sites on ZSM-5 has certain effects on W-induced acidity. This can be correlated with the catalytic activity at 750 °C. In methane-activation chemistry, the acidity of metal sites might be critical in the initial stage of the reaction. It is well-known that Lewis acid-base pairs can activate C-H bonds heterolytically[19]: The electron-deficient/undercoordinated metal site (Lewis acid) can polarize the C-H bond and form σ-bond with CH_3 moieties while pair basic site (i.e., neighboring basic oxygen center) accepts a proton. Therefore, we performed pyridine-IR (Figure S28a and S29a) to investigate the acid sites of fresh

Z26, 2W-Z26, and 6W-Z26. As depicted in Table 3 (at 150 °C – after removing physisorbed pyridine), the number of BASs sharply decreases upon W introduction to zeolite compared to the decrease in the number of Lewis acid sites (LASs). This clearly indicates that W cations replace protons of some BASs. However, 6W-Z26 has slightly higher BASs than 2W-Z26 at 150 °C, which could mean there are more polymeric W sites at 6 wt. % loading and results in more free zeolite BASs. When we further treated the samples at 350 °C and forced some pyridine to desorb, it was noticed that 2W-Z26 and 6W-26 have a similar number of BASs but 6W-Z26 has a higher amount of LASs. These LASs could explain the higher catalytic activity of 6W-Z26 at 750 °C.

The comparison of the benchmark 2Mo-Z26 catalyst with its W counterparts is another vital point in this study. Based on our previous studies (in which we used the same catalyst)[7,20] and characterizations presented here, 2Mo-Z26 catalyst has good metal dispersion/distribution and prevailing microporosity after Mo introduction. For instance, our PXRD, UV-vis DRS, and micro-Raman analyses reveal that no segregated/agglomerated molybdenum oxide phases were formed on the fresh catalyst. However, there are some pronounced differences compared to W-samples when it comes to metal-zeolite interaction and acidity. As depicted in our previous study[7] via ^{27}Al MAS NMR, Mo introduction leads to aluminum molybdate formation (i.e., Anderson-type aluminum polyoxymolybdates) whose tungsten-analogue was not observed in the W cases. Also, the acidity analyses (Table 2 and Table 3) reveal some interesting differences. Based on NH_3-TPD results (Table 2), there is a sharp loss of strong acid sites on 2Mo-Z26 catalyst upon metal introduction compared to W-Z26 samples. Pyridine-IR analyses indicate that these disappeared strong acids are mostly BASs since 2Mo/Z26 has a lower BAS/LAS (B/L) ratio compared to bare ZSM-5 and W-loaded ones (Table 3). Considering these dissimilarities, it could be suggested that

Mo disperses and interacts with zeolite acid sites (especially BASs) much more vigorously. Furthermore, lower acid density on the 2Mo/Z26 catalyst suggests another important insight. As depicted before through the catalysis data, the Mo version of the catalyst is much more effective in aromatics production. Since 2Mo-Z26 has lower acid density and lower B/L ratio, the high aromatization activity could be linked to the active Mo sites rather than the zeolite acidity. However, it should also be noted that these metal sites (W and Mo) have dynamic characters (i.e., detaching from the zeolite pores) during the reaction. So, the fate and role of acid sites are hard to be understood at the moment of reaction.

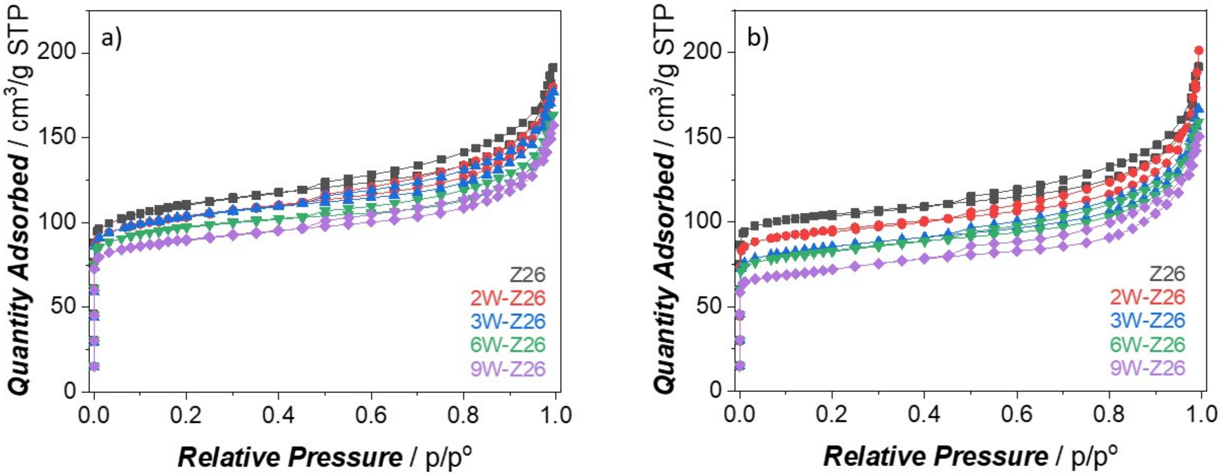

Figure S14. N_2 physisorption isotherms of a) fresh samples (bare ZSM-5 and W loaded ZSM-5) and b) four times regenerated ones (bare ZSM-5 and W loaded ZSM-5)

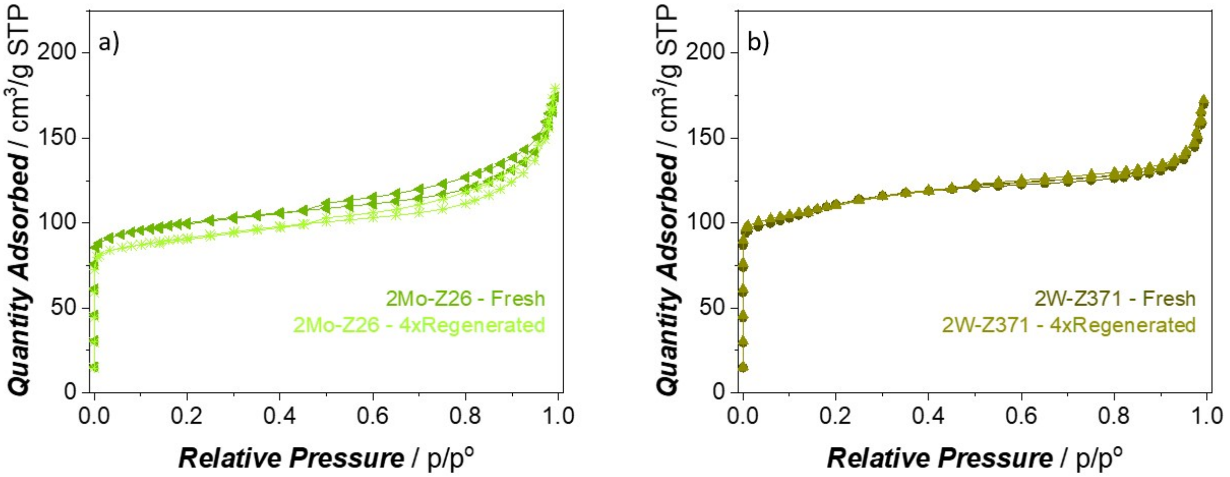

Figure S15. N_2 physisorption isotherms of a) 2Mo-Z26 (fresh vs four-times-regenerated) and b) 2W-Z371 (fresh vs four-times-regenerated)

Table S1. Nitrogen physisorption analyses of fresh samples and four times regenerated ones (bare ZSM-5 and W loaded ZSM-5)

Samples	**S_{BET} (m^2/g)**	**$S_{meso/ext}$ (m^2/g)***	**S_{micro} (m^2/g)****	**V_{total} (ml/g)*****	**V_{micro} (ml/g)****
Z26	419	122	297	0.24	0.12
Z26 *4xRegenerated*	411	72	339	0.23	0.13
2W-Z26	397	104	293	0.23	0.11
2W-Z26 *4xRegenerated*	372	79	293	0.22	0.11
3W-Z26	396	106	290	0.23	0.11
3W-Z26 *4xRegenerated*	330	79	251	0.20	0.10
6W-Z26	372	100	272	0.21	0.11
6W-Z26 *4xRegenerated*	321	81	240	0.20	0.09
9W-Z26	346	85	261	0.20	0.10
9W-Z26 *4xRegenerated*	279	75	204	0.18	0.08

* $S_{meso/ext} = S_{BET} - S_{micro}$ - ** From N_2 adsorption isotherm using the t-plot method - *** Single point adsorption total pore volume @ $p/p^o=0.95$

Table S2. Nitrogen physisorption analyses of fresh samples and four times regenerated ones (Z371 and 2W-Z371)

Samples	**S_{BET} (m^2/g)**	**$S_{meso/ext}$ (m^2/g)***	**S_{micro} (m^2/g)****	**V_{total} (ml/g)*****	**V_{micro} (ml/g)****
Z371	415	159	256	0.21	0.10
2W-Z371	411	183	228	0.21	0.09
2W-Z371 *4xRegenerated*	424	137	287	0.22	0.11

* $S_{meso/ext} = S_{BET} - S_{micro}$ - ** From N_2 adsorption isotherm using the t-plot method - *** Single point adsorption total pore volume @ $p/p^o=0.95$

Table S3. Nitrogen physisorption analyses of fresh samples and four times regenerated ones (Z26 and 2Mo-Z26)

Samples	**S_{BET} (m^2/g)**	**$S_{meso/ext}$ (m^2/g)***	**S_{micro} (m^2/g)****	**V_{total} (ml/g)*****	**V_{micro} (ml/g)****
Z26	419	122	297	0.24	0.12
2Mo-Z26	384	98	286	0.22	0.11
2Mo-Z26 *4xRegenerated*	352	89	264	0.21	0.10

* $S_{meso/ext} = S_{BET} - S_{micro}$ - ** From N_2 adsorption isotherm using the t-plot method - *** Single point adsorption total pore volume @ p/p°=0.95

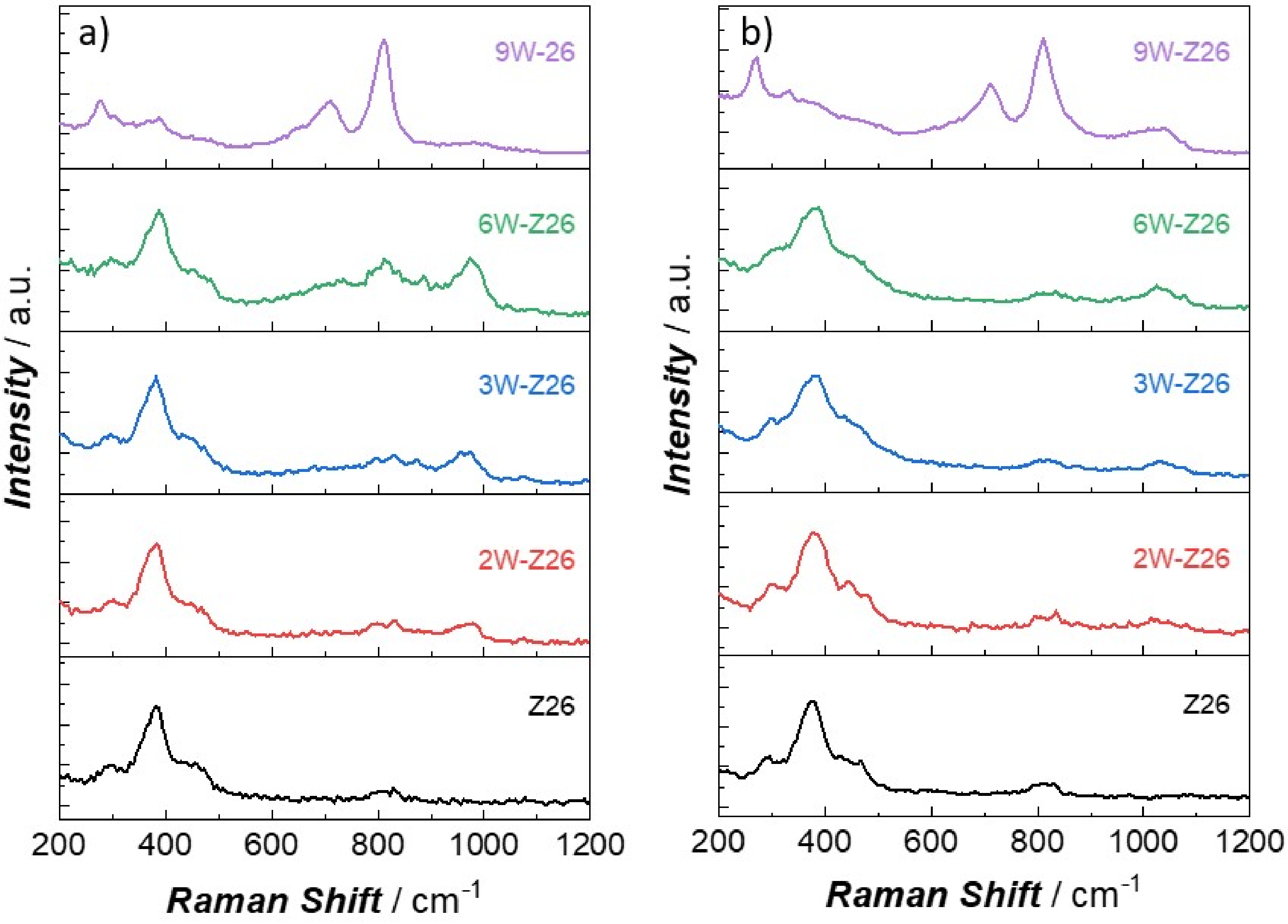

Figure S16. Vis-Raman (473 nm) spectra of a) fresh and b) four times regenerated Z26, 2W-Z26, 3W-Z26, 6W-Z26, and 9W-Z26 samples

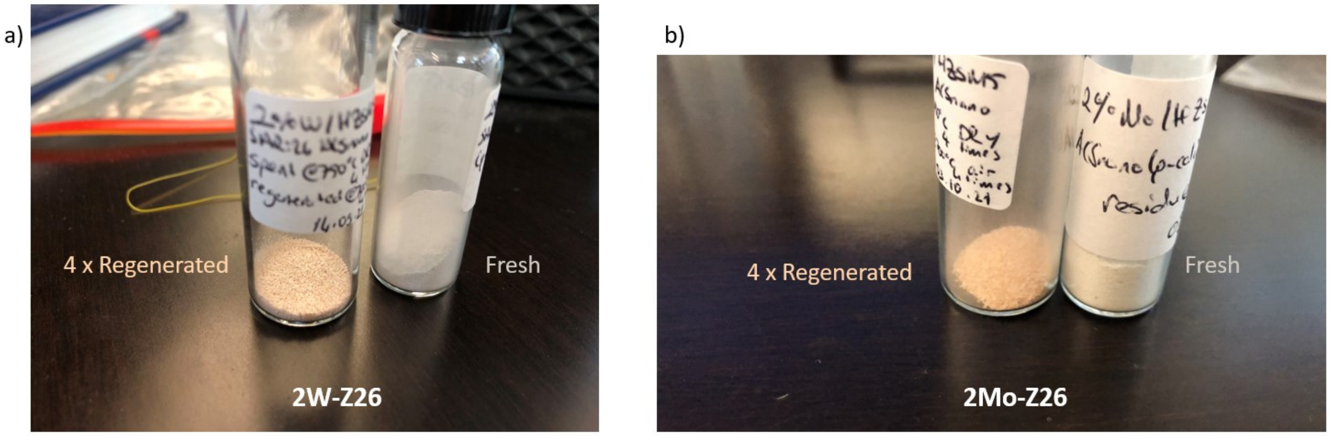

Figure S17. The color change of samples before and after reaction-regeneration cycles: a) 2W-Z26 and b) 2Mo-Z26

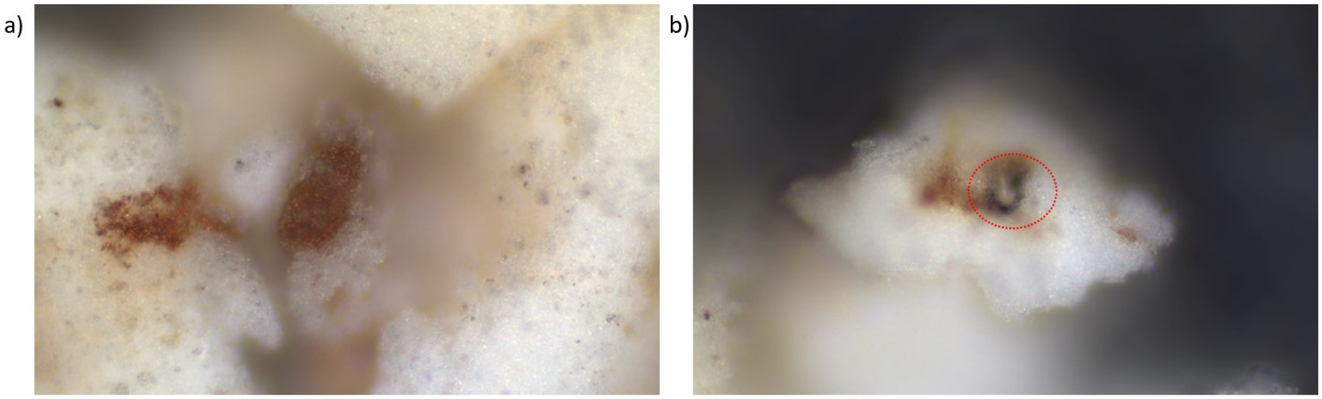

Figure S18. Micro-Raman images of regenerated samples: brown spots a) before and b) after laser irradiation

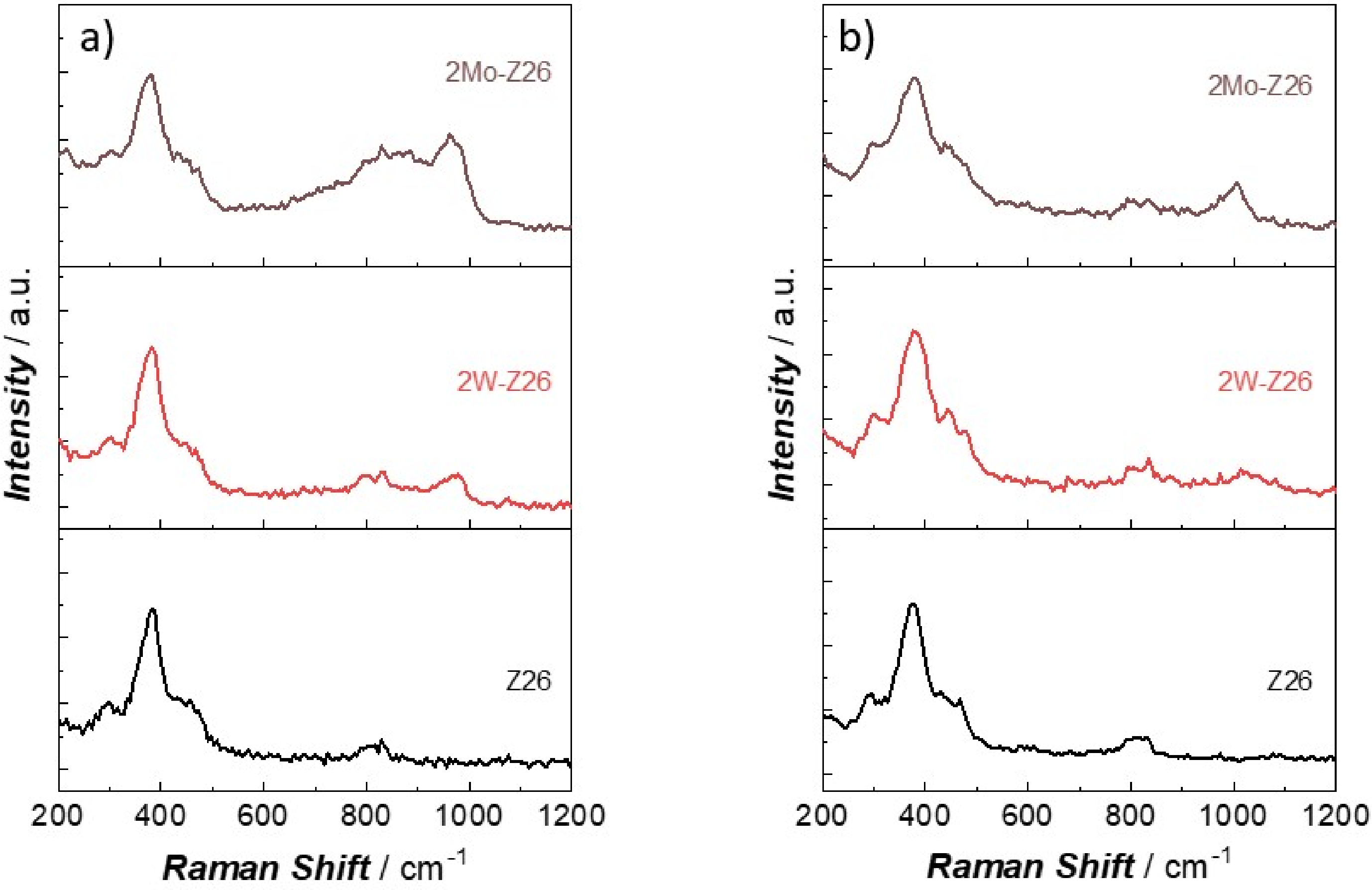

Figure S19. Vis-Raman (473 nm) spectra of a) fresh and b) four times regenerated Z26, 2W-Z26, and 2Mo-Z26 samples

Table S4. ICP-OES data for fresh and four times regenerated catalysts

Sample	Al wt. %	M wt.%	$\text{Metal}_{\text{mmoles}}$ / $\text{ZSM-5}_{\text{gram}}$
2W-Z26 Fresh	2.40	1.83	0.101
2W-Z26 4xRegenerated	2.16	1.88	-
3W-Z26 Fresh	2.24	3.14	0.176
3W-Z26 4xRegenerated	2.29	3.49	-
6W-Z26 Fresh	2.41	5.87	0.339
6W-Z26 4xRegenerated	2.29	5.59	-
9W-Z26 Fresh	2.37	8.91	0.532
9W-Z26 4xRegenerated	2.23	9.90	-
2Mo-Z26 Fresh	2.41	1.85	0.196
2Mo-Z26 4xRegenerated	2.16	1.92	-
2W-Z26 (Physical Mix) Fresh	2.16	1.83	0.101
2W-Z26 (Physical Mix) 4xRegenerated	2.33	1.91	-
2W-Z371 Fresh	0.23	1.70	0.094

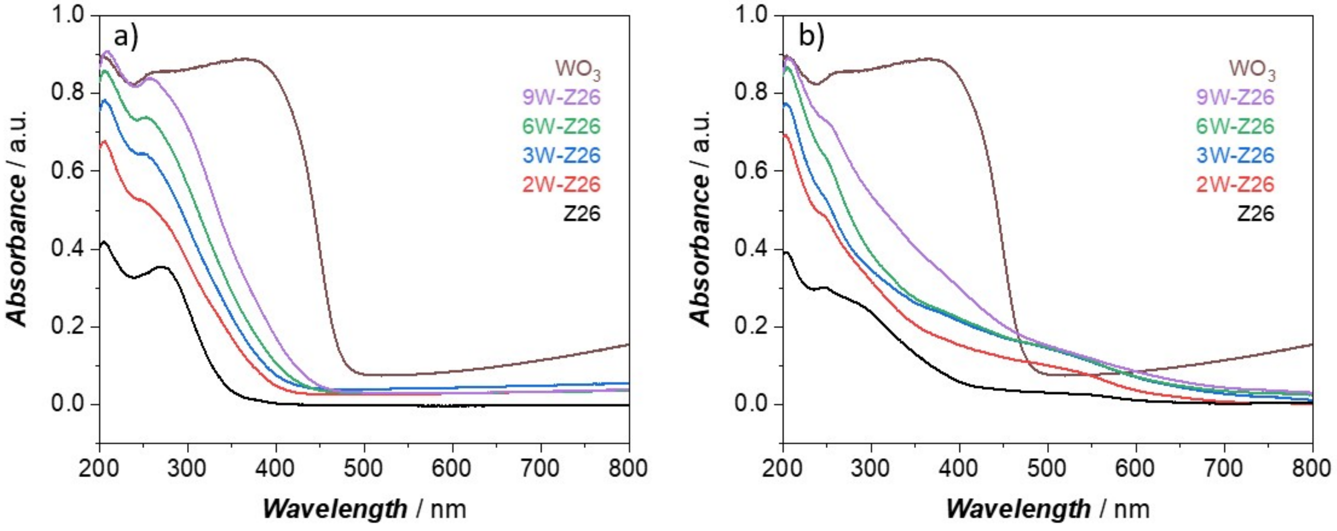

Figure S20. UV-vis spectra of a) fresh and b) four times regenerated Z26, 2W-Z26, 3W-Z26, 6W-Z26, and 9W-Z26 samples (background: $BaSO_4$)

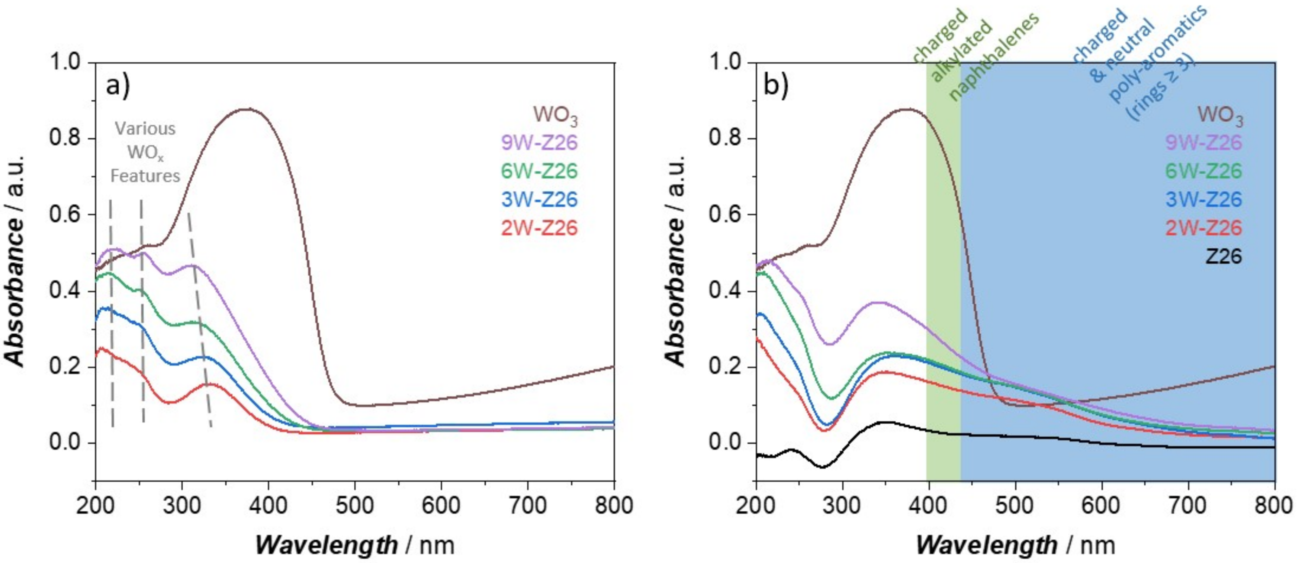

Figure S21. UV-vis spectra of a) fresh and b) four times regenerated Z26, 2W-Z26, 3W-Z26, 6W-Z26, and 9W-Z26 samples (background: fresh Z26)

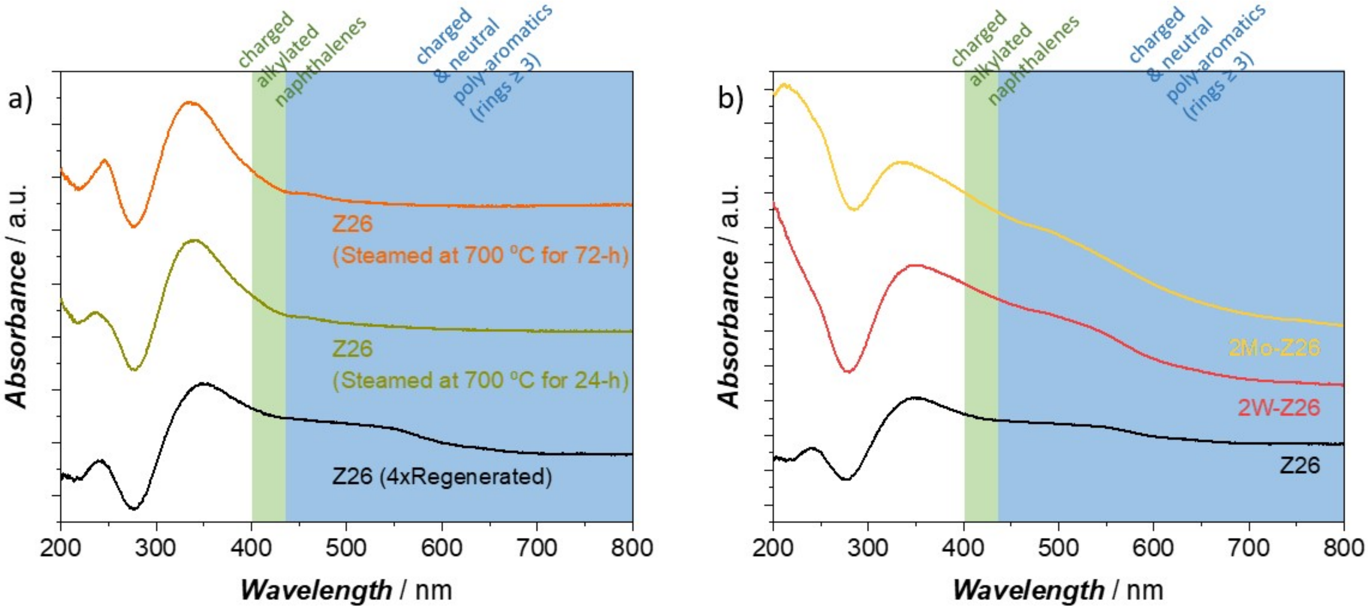

Figure S22. UV-vis spectra of a) four times regenerated Z26, and steam treated Z26 samples and b) four times regenerated Z26, 2W-Z26, 2Mo-Z26 (background: fresh Z26): The absorption peaks centered around ca. 242 and ca. 340 nm wavelength can be attributed to the defects formed in/on ZSM-5. To confirm this, we treated bare ZSM-5 with steam at 700 °C to form defects (i.e., EFAl, silanol, etc.). Same absorption features were detected with steam treated zeolites.

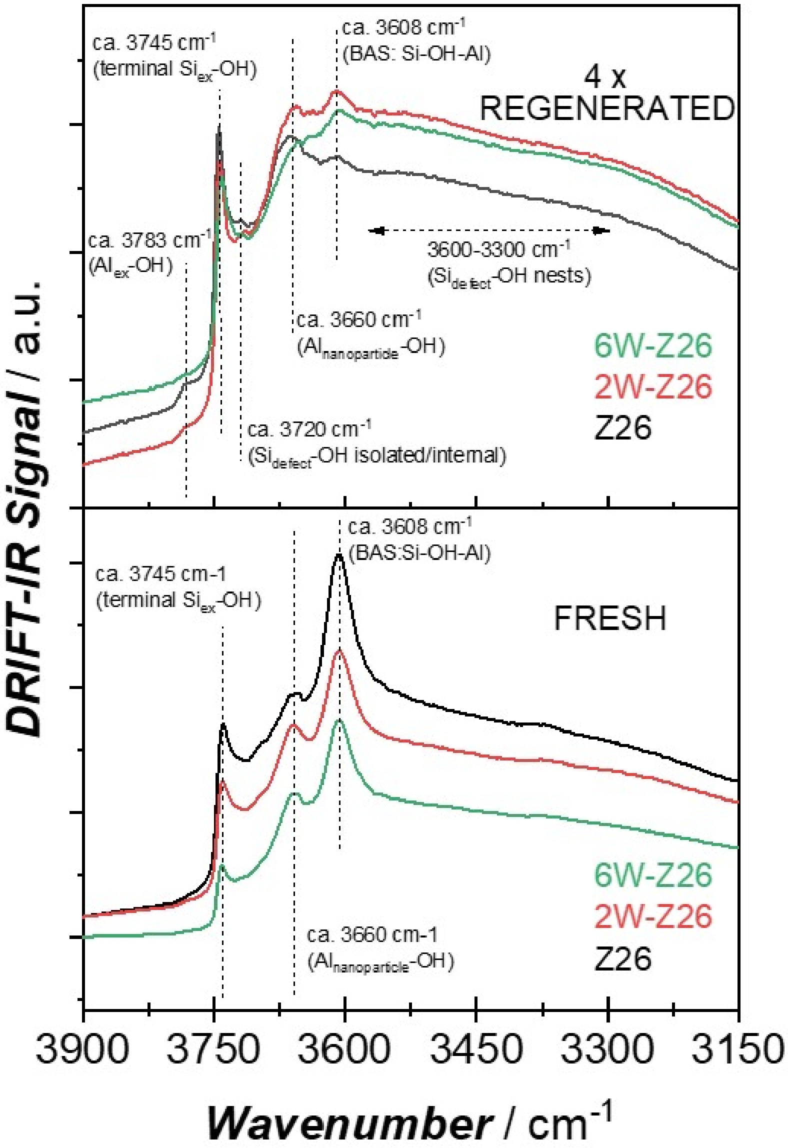

Figure S23. DRIFT spectra of fresh and four times regenerated Z26, 2W-Z26 and 6W-26. The vibrations on the spectra were assigned considering the literature[21,22]

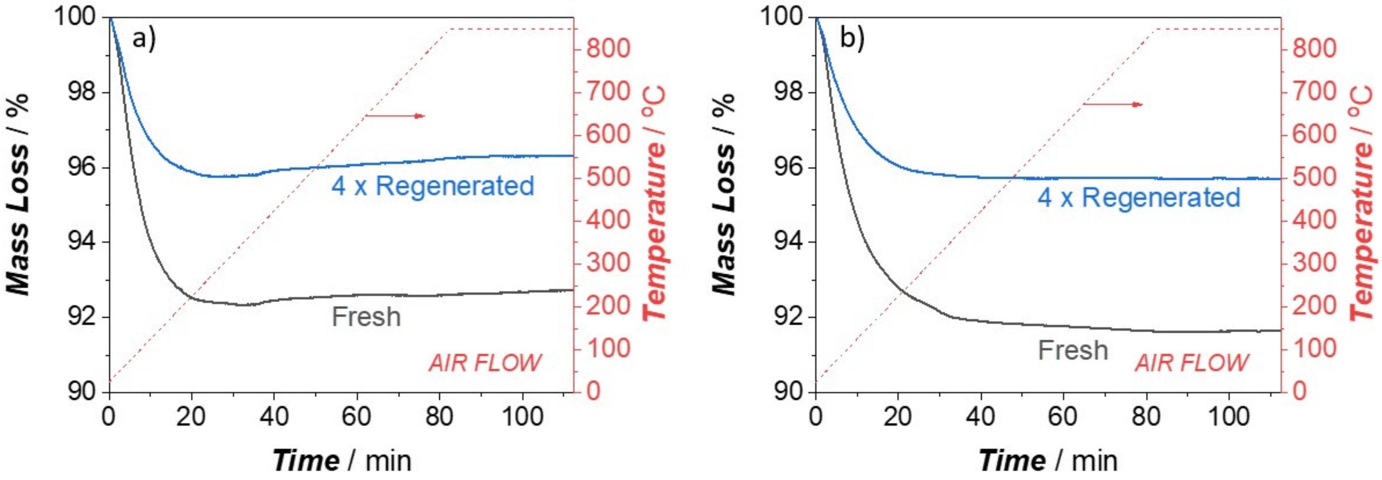

Figure S24. TPO analysis (under air flow) for fresh and four times regenerated samples: a) 2W-Z26 and b) 2Mo-Z26

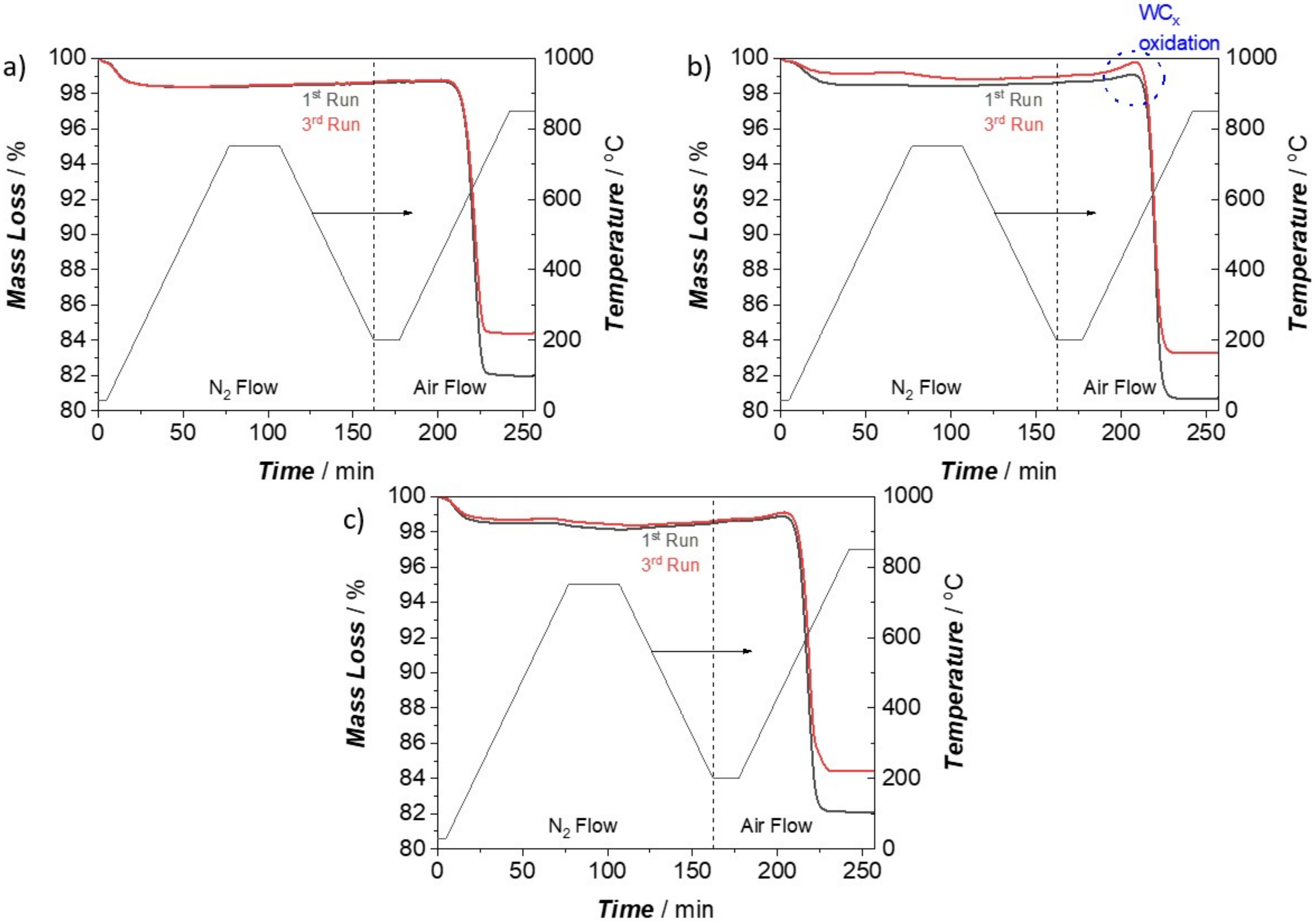

Figure S25. TPO analysis for spent catalysts after 1st and 3rd reaction steps during the reaction-regeneration cycles: a) 2W-Z26, b) 6W-Z26, and c) 2Mo-Z26

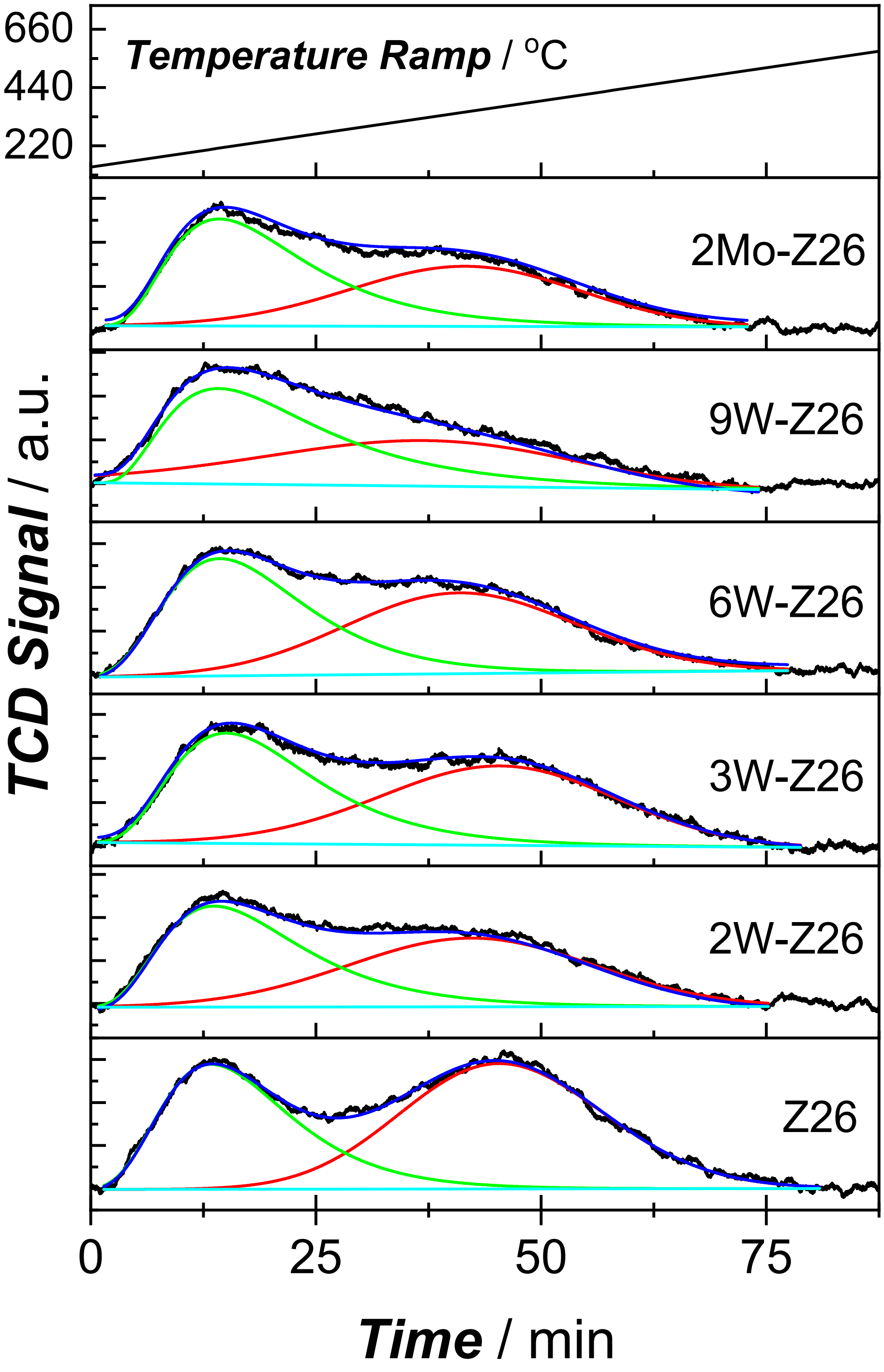

Figure S26. NH_3 TPD curves of pristine ZSM-5, W and Mo loaded ZSM-5 catalysts

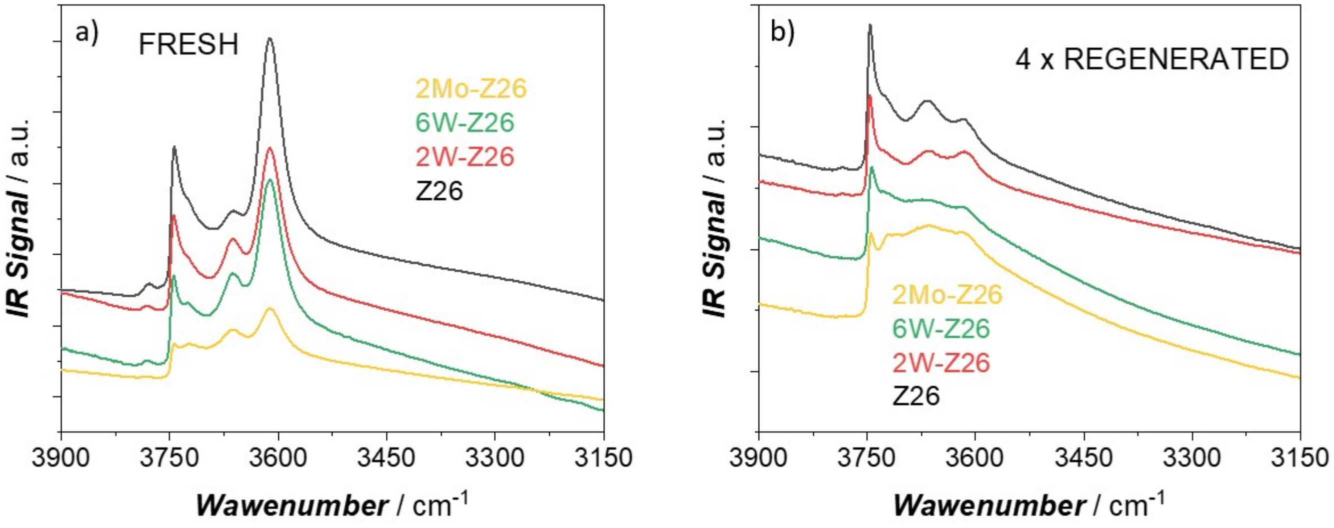

Figure S27. FTIR spectra (hydroxyl region) before pyridine chemisorption: a) fresh and b) four times regenerated samples

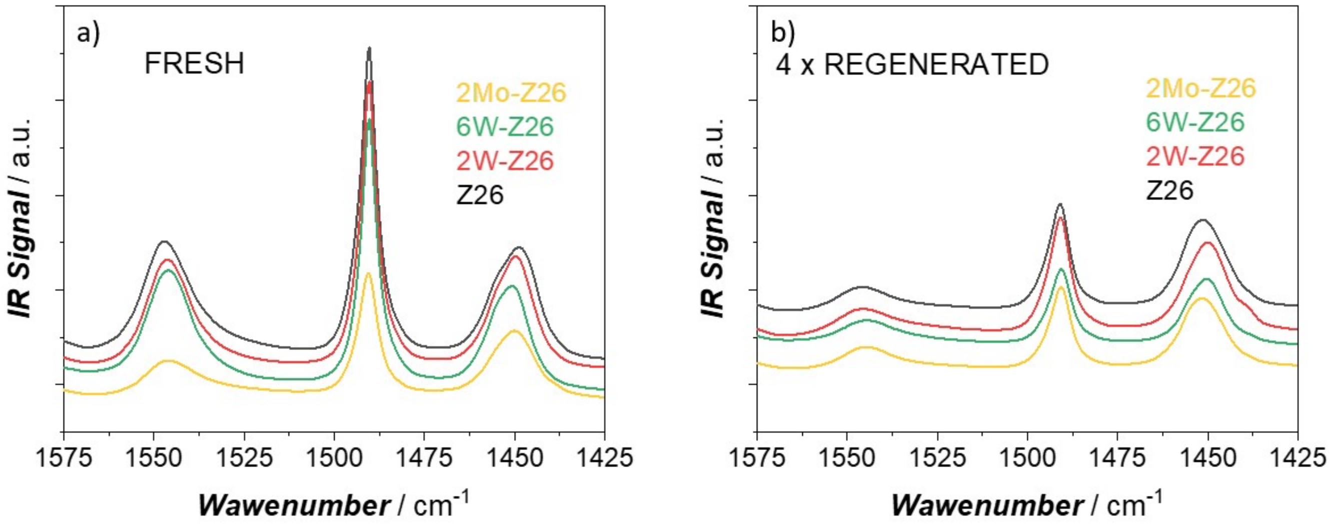

Figure S28. FTIR spectra of chemisorbed pyridine after treatment at 150 °C

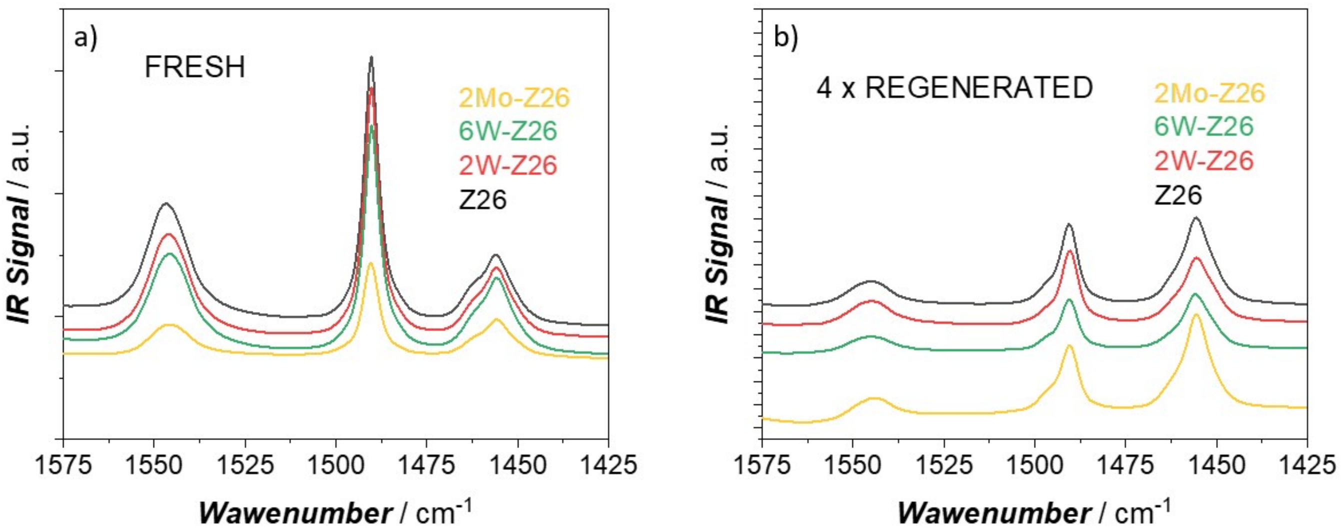

Figure S29. FTIR spectra of chemisorbed pyridine after treatment at 350 °C

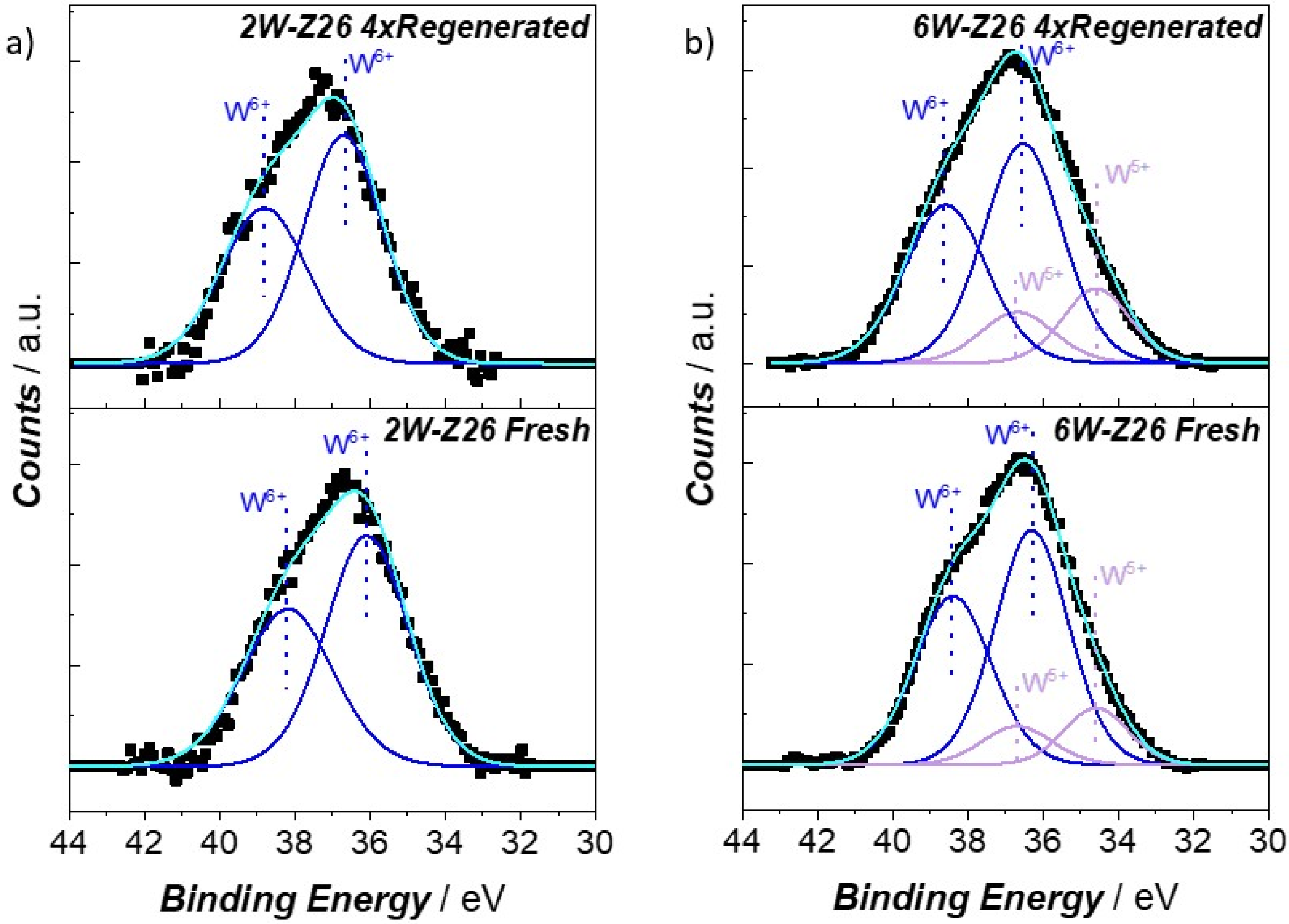

Figure S30. XPS spectra of 2W-Z26 (a) and 6W-Z26 (b) before and after reaction-regeneration cycles

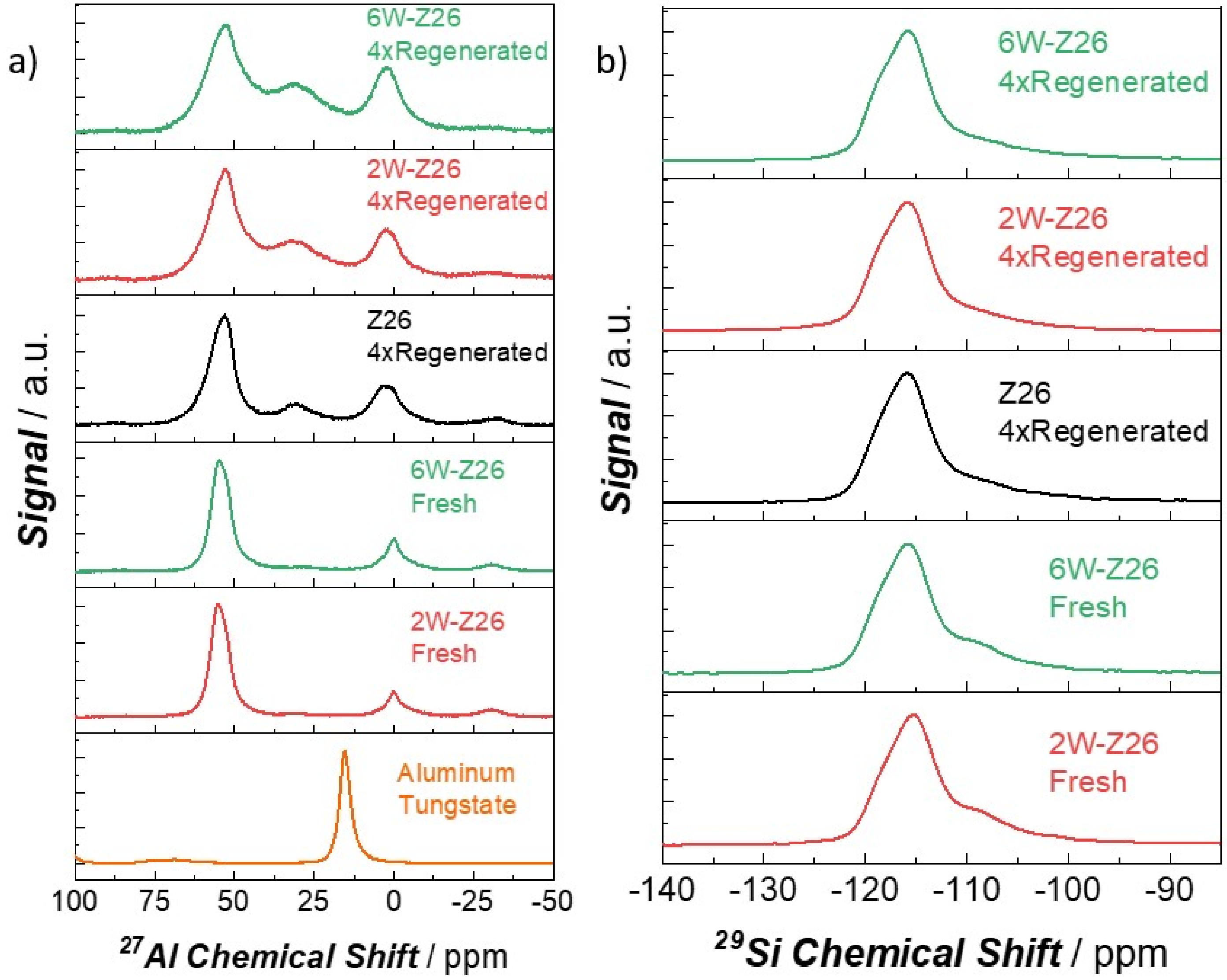

Figure S31. Solid-state a) 1D ^{27}Al NMR and b) 1D ^{29}Si NMR spectra of the fresh and regenerated Z26, 2W-Z26 and 6W-Z26 catalysts; and aluminum tungstate

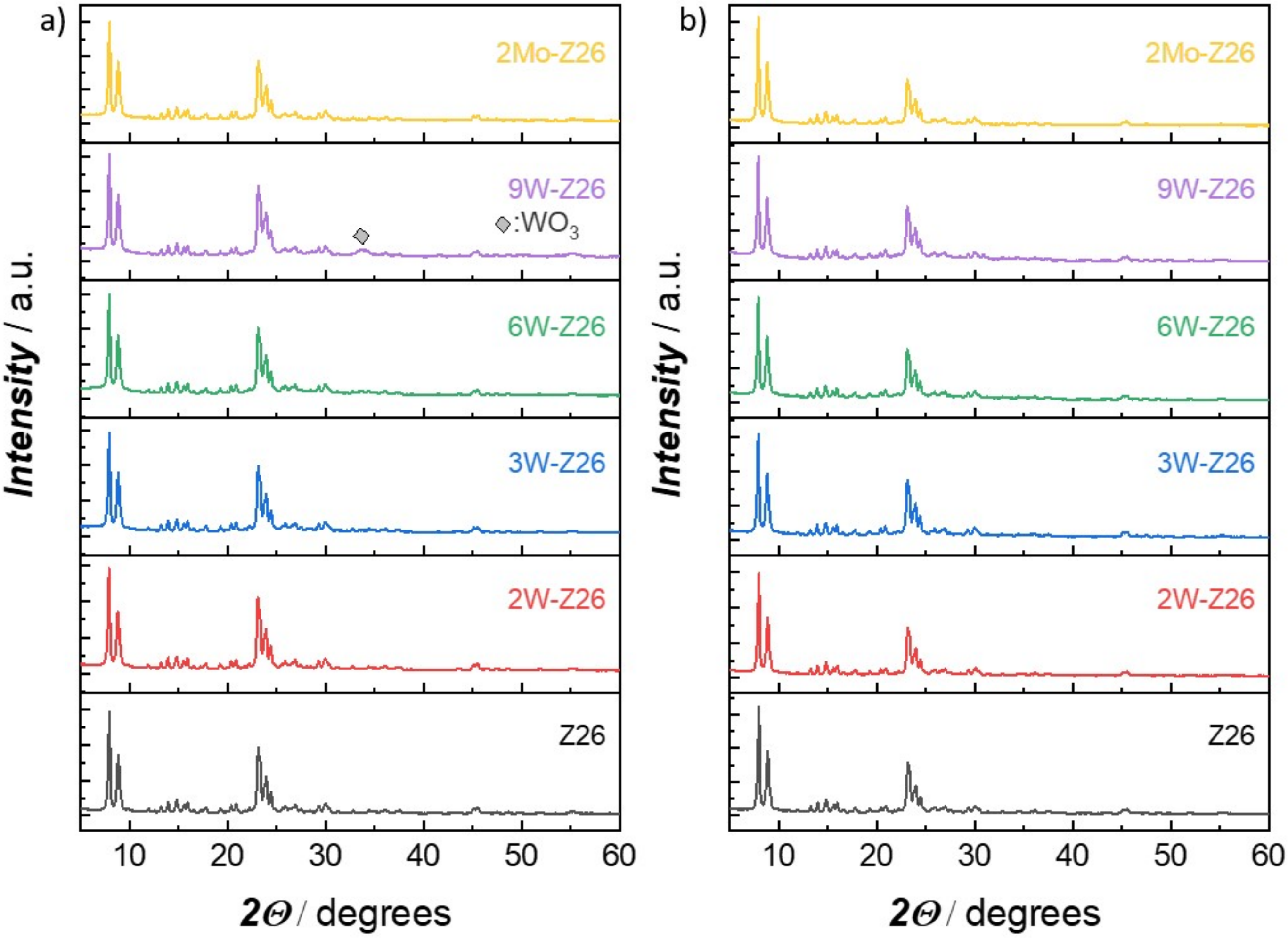

Figure S32. PXRD patterns before (a) and after (b) reaction-regeneration cycles for Z26, 2W-Z26, 3W-Z26, 6W-Z26, 9W-Z26, and 2Mo-Z26

Table S5. Crystallographic parameters and pattern characteristics derived from PXRD for fresh pristine, Mo- and W-modified zeolites and their regenerated after catalytic run counterparts. The variation in an intensity of (011) and (200) peaks strongly depends on the aluminum content meanwhile the (501) diffraction line shows to be less sensitive to the framework composition.[23] Our results suggest that the dealumination takes place during regeneration cycles and the magnitude of that event varies to a small extent depending on the W-content in the catalysts.

Sample	*a* [Å]	*b* [Å]	*c* [Å]	*V* [Å^3]	(*a*-*b*) [Å]	FWHM [°]	X_c [%]	$\frac{I^{(011)}}{I^{(501)}}$	$\frac{I^{(200)}}{I^{(501)}}$
Z26 – Fresh	20.0515(11)	19.7806(12)	13.2997(9)	5275.1(6)	0.271	0.204	88.5	1.52	0.88
Z26 – 4 x Regenerated	19.9898(15)	19.774(14)	13.2428(10)	5234.6(7)	0.216	0.214	88.2	2.06	1.22
2W-Z26 – Fresh	19.9715(13)	19.7159(13)	13.2210(8)	5205.9(6)	0.255	0.208	83.3	1.38	0.82
2W-Z26 – 4 x Regenerated	20.0076(4)	19.7484(5)	13.20017(16)	5215.62(17)	0.259	0.209	87.4	2.30	1.20
3W-Z26 – Fresh	19.9836(16)	19.7679(17)	13.2708(12)	5242.4(8)	0.216	0.211	82.1	1.47	0.91
3W-Z26 – 4 x Regenerated	20.0265(12)	19.7777(12)	13.2810(10)	5260.3(6)	0.249	0.212	83.0	1.76	1.11
6W-Z26 – Fresh	19.9700(12)	19.7311(14)	13.2492(11)	5220.6(6)	0.239	0.207	81.1	1.47	0.89
6W-Z26 – 4 x Regenerated	19.9905(2)	19.74076(19)	13.20322(13)	5210.35(9)	0.250	0.214	80.8	1.97	1.24
9W-Z26 – Fresh	20.0068(15)	19.7661(16)	13.2845(12)	5253.4(8)	0.241	0.210	80.4	1.42	0.88
9W-Z26 – 4 x Regenerated	20.0346(13)	19.7935(14)	13.2972(11)	5273.0(7)	0.241	0.214	74.8	1.84	1.15
2Mo-Z26 – Fresh	20.0466(11)	19.7789(11)	13.2856(9)	5267.7(5)	0.268	0.212	88.0	1.62	0.99
2Mo-Z26 – 4 x Regenerated	20.0332(12)	19.7900(12)	13.2880(10)	5268.1(6)	0.243	0.215	87.3	2.30	1.35

FWHM [° 2θ] – full width at half maximum of the 8.0° 2θ peak corresponding to (011) diffraction;

X_c [%] – crystallinity over 5 – 40° 2θ range;

$I^{(011)}/I^{(501)}$ and $I^{(200)}/I^{(501)}$ – relative intensities of (011) and (200) diffraction peaks to (501)

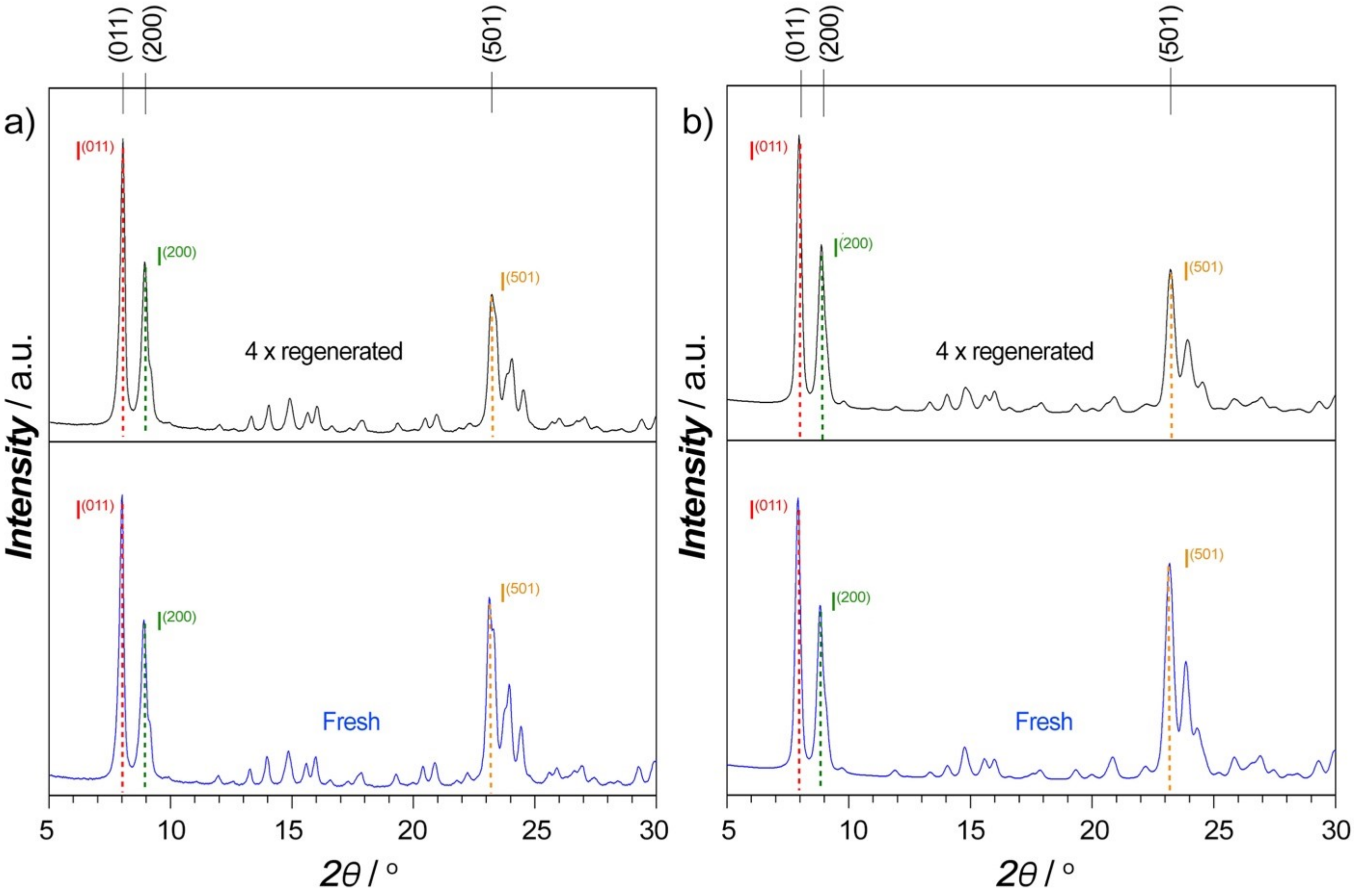

Figure S33. Comparison of relative intensity changes in (011) and (200) diffraction peaks to (501) one for fresh and 4-times regenerated catalysts: (a) Z26 and (b) 2W-Z26

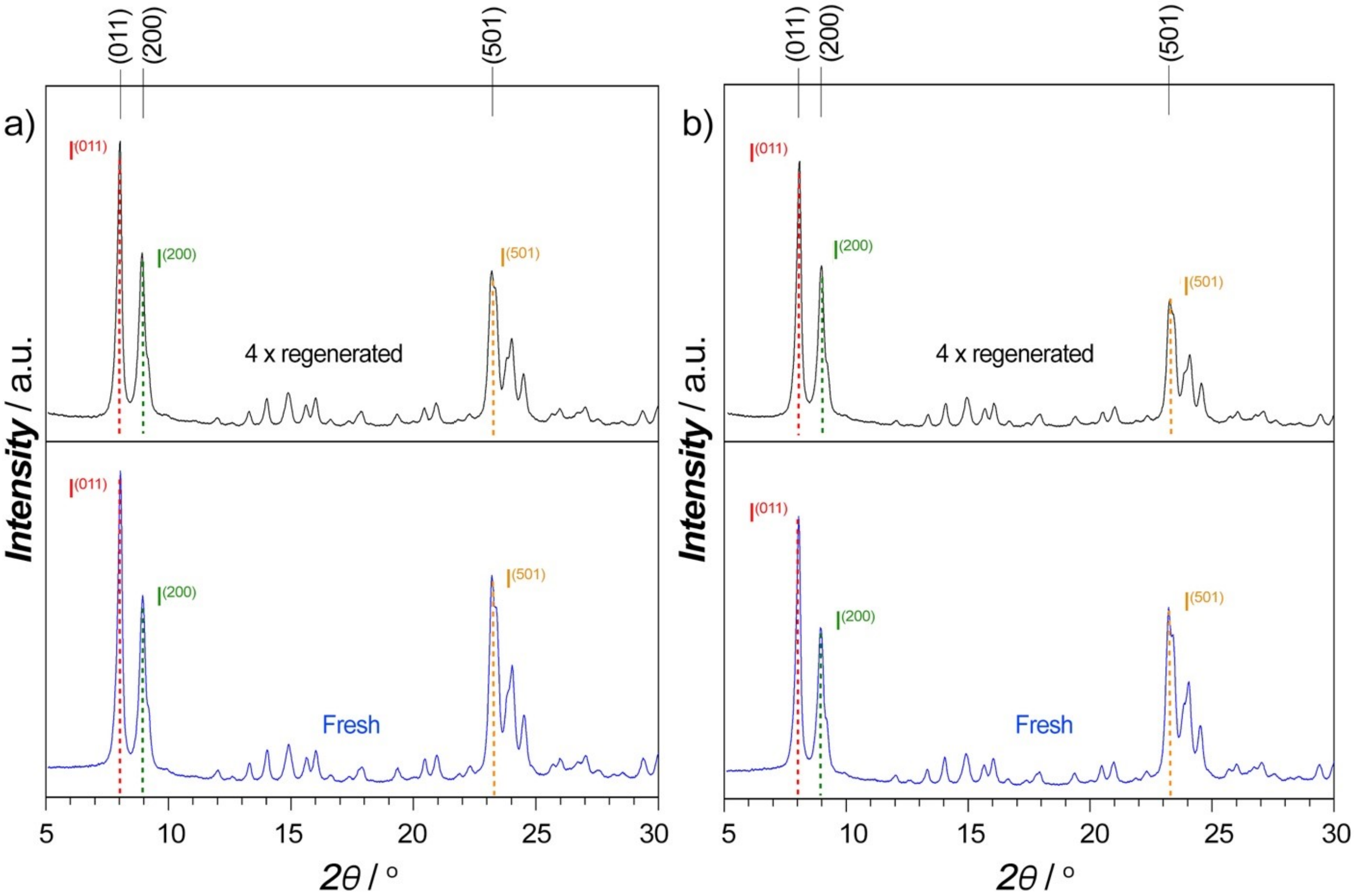

Figure S34. Comparison of relative intensity changes in (011) and (200) diffraction peaks to (501) one for fresh and 4-times regenerated catalysts: (a) 3W-Z26 and (b) 6W-Z26

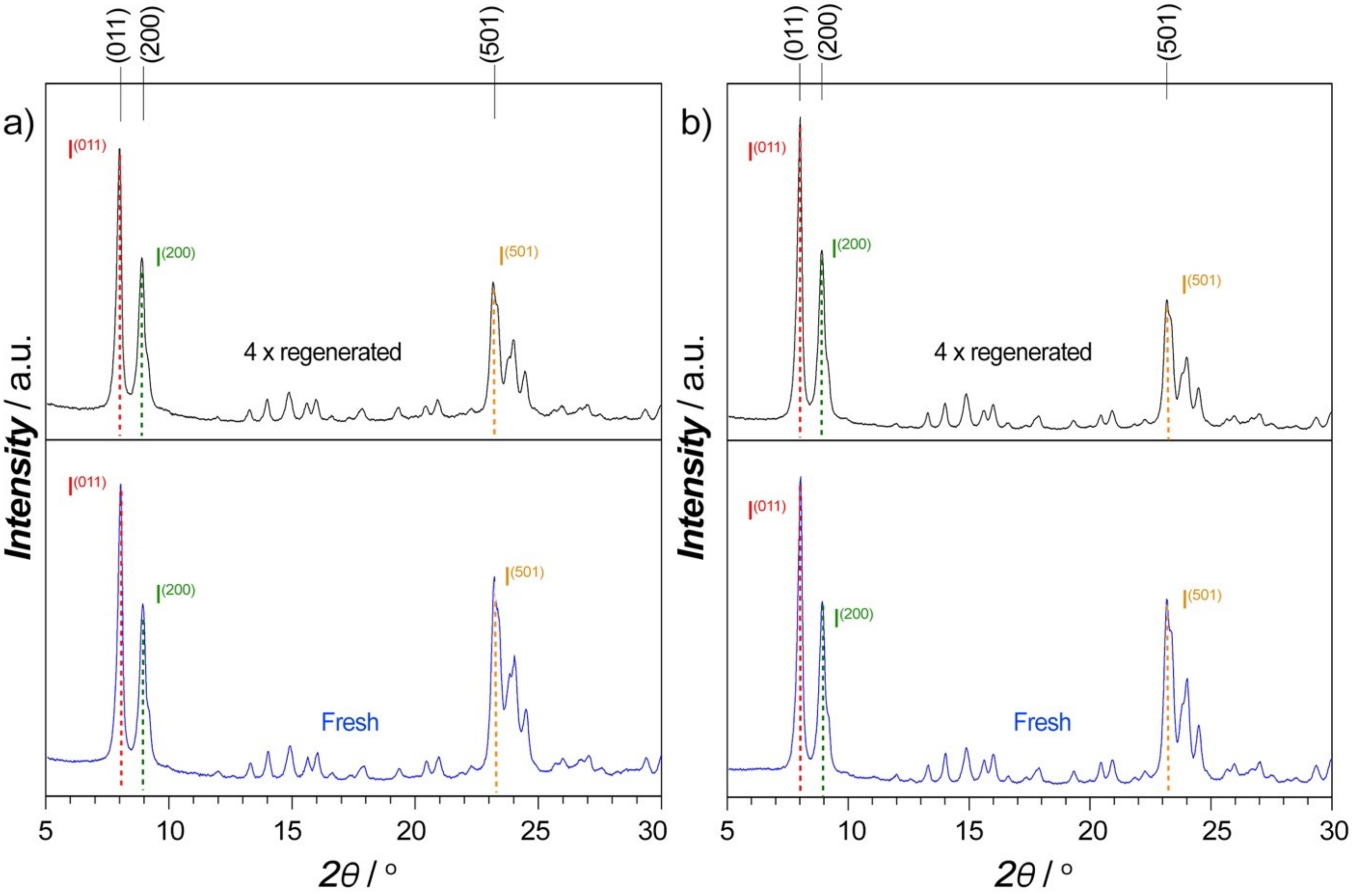

Figure S35. Comparison of relative intensity changes in (011) and (200) diffraction peaks to (501) one for fresh and 4-times regenerated catalysts: (a) 9W-Z26 and (b) 2Mo-Z26

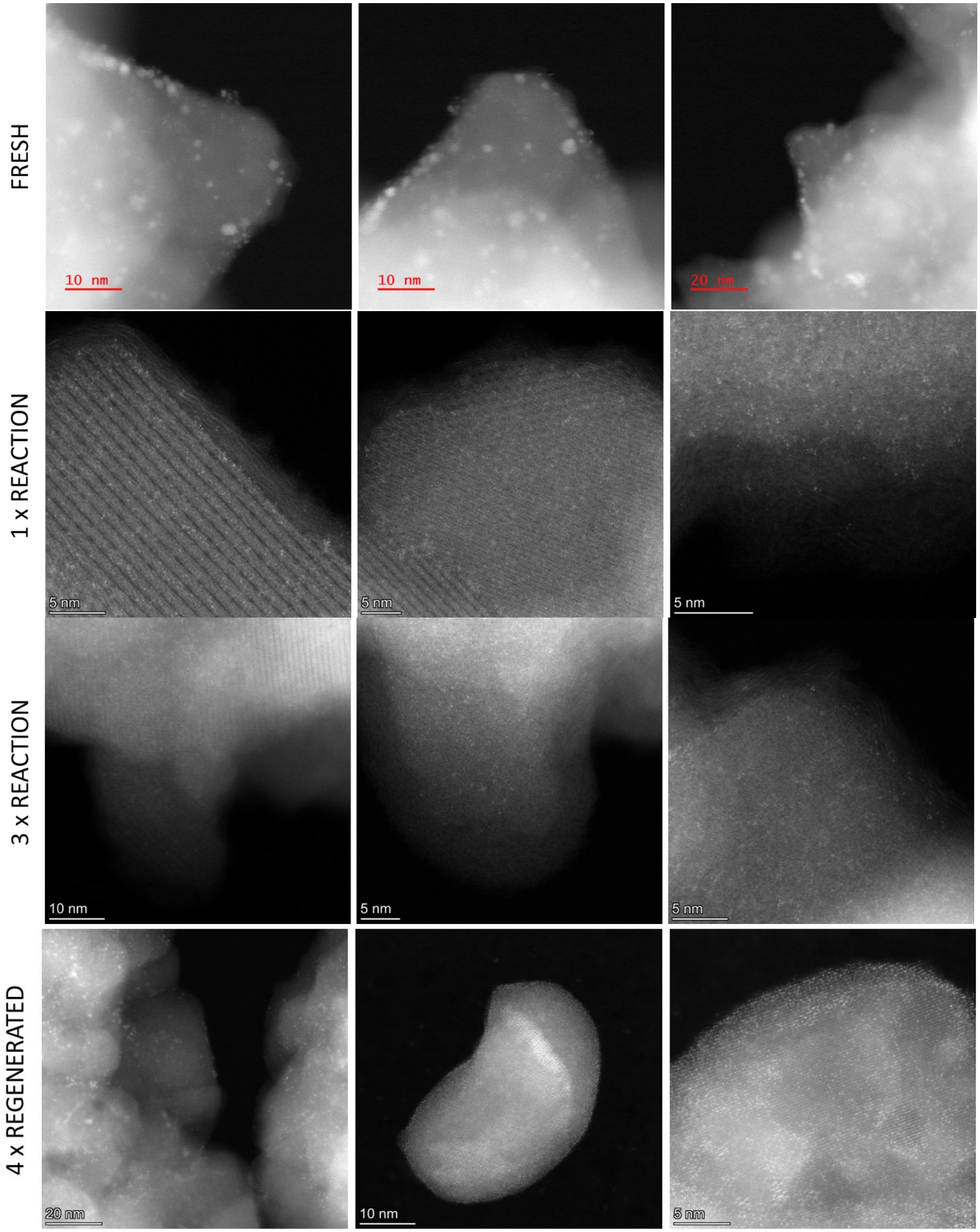

Figure S36. Ex-situ High-angle annular dark field scanning transmission electron microscopy (HAADF-STEM) images of 2W-Z26 catalyst at different stage of catalytic cycle.

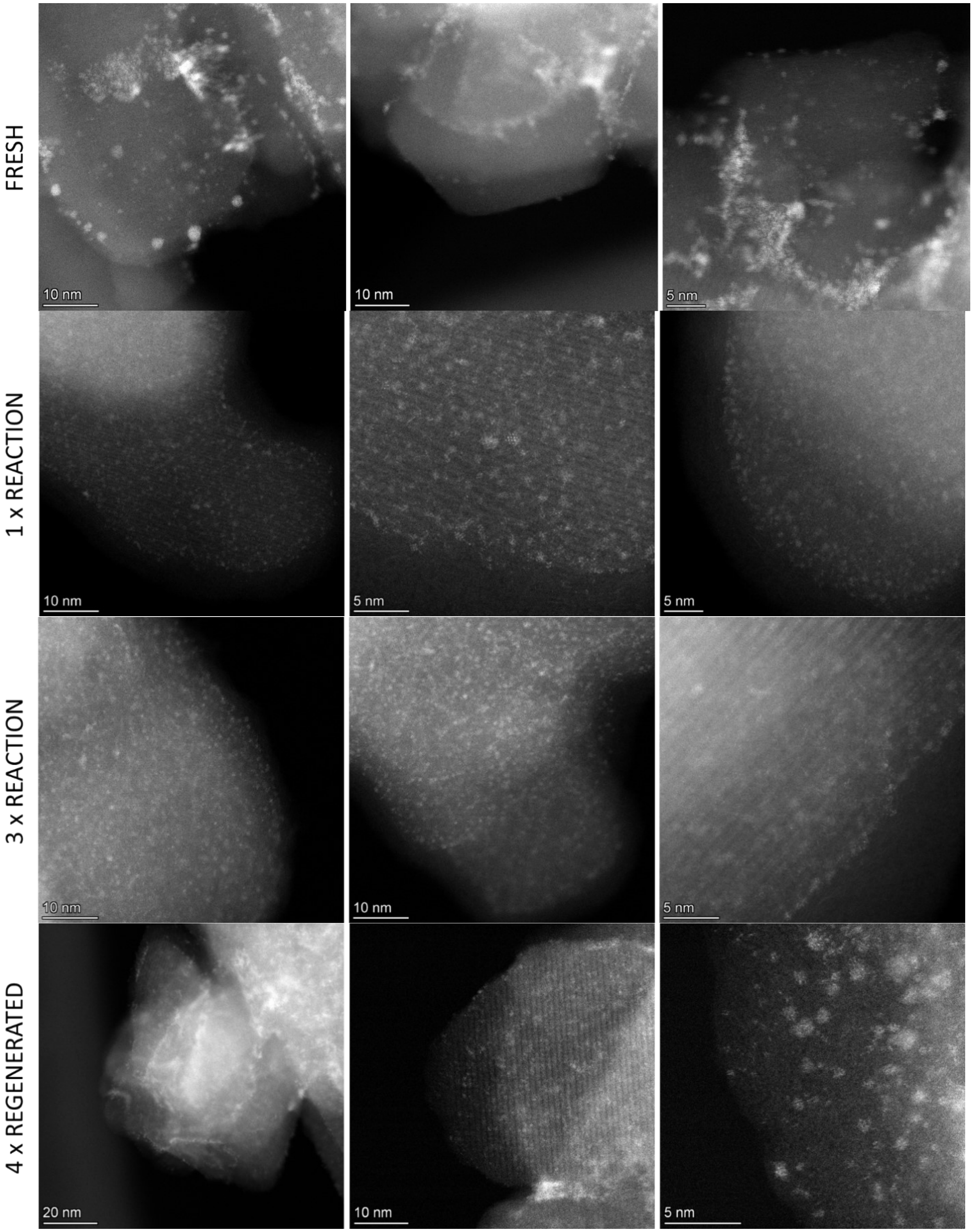

Figure S37. Ex-situ High-angle annular dark field scanning transmission electron microscopy (HAADF-STEM) images of 6W-Z26 catalyst at different stage of catalytic cycle.

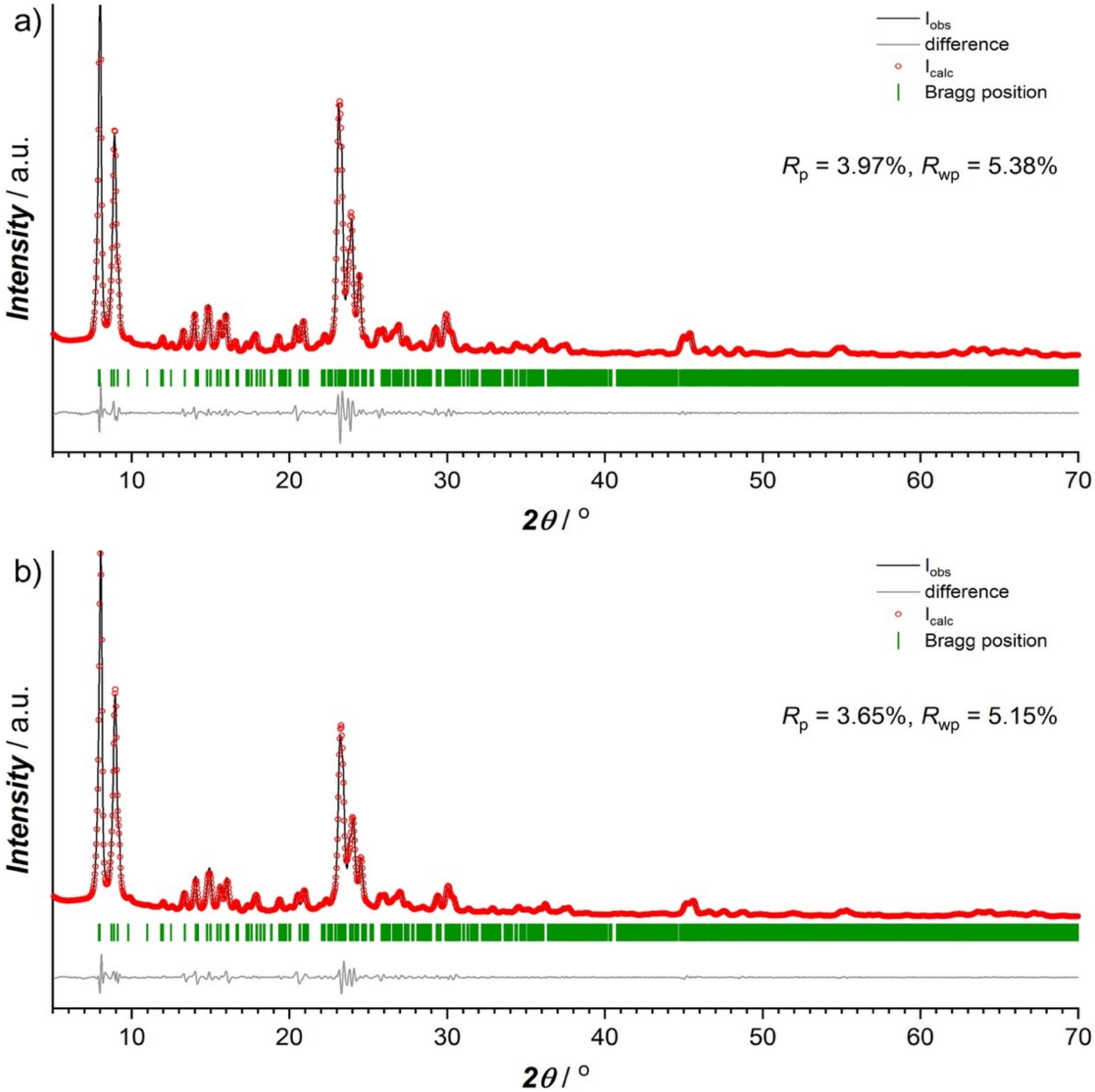

Figure S38. Le Bail refinement plot for parent (a) fresh and (b) regenerated 4-times Z26 catalyst

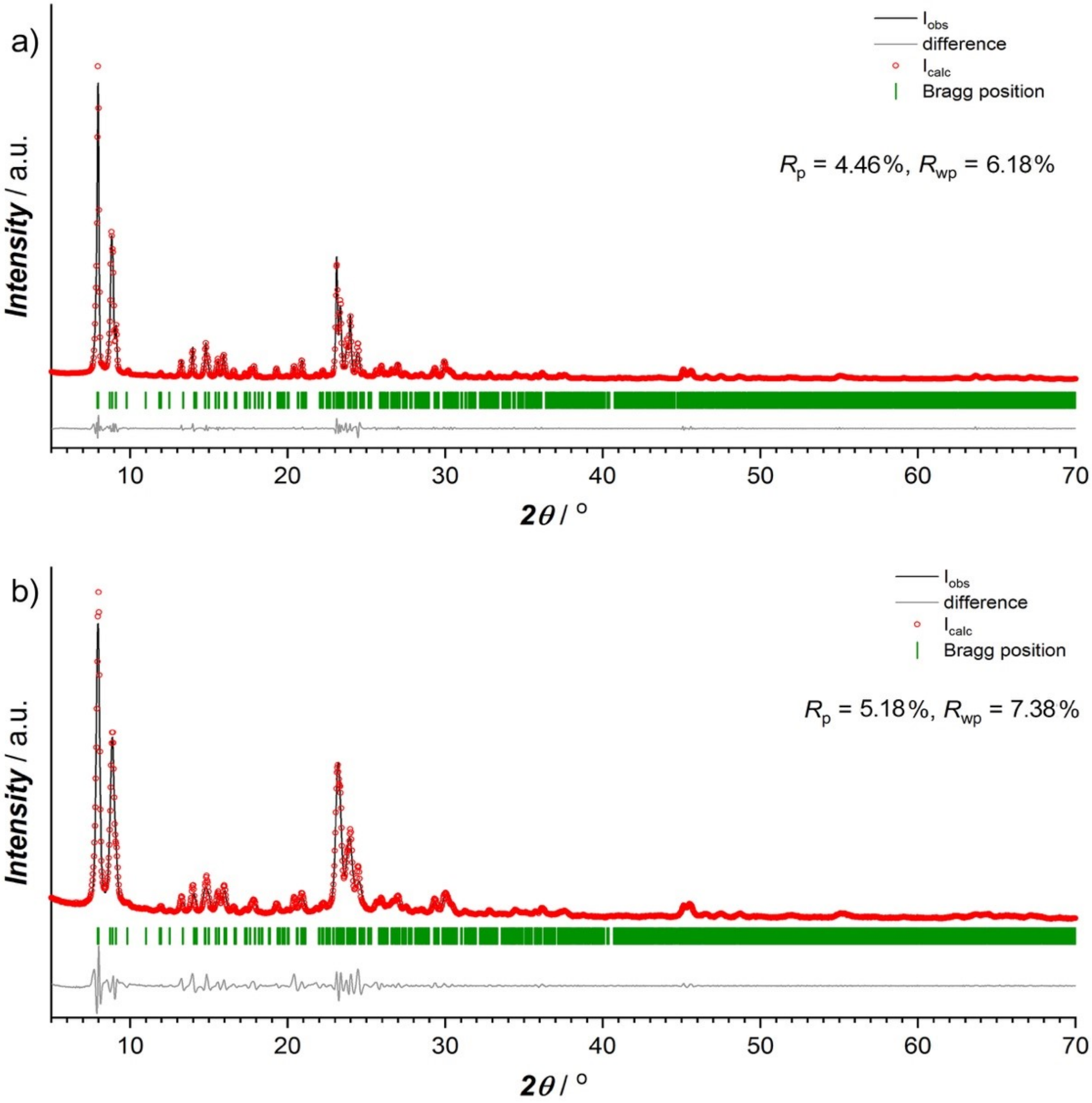

Figure S39. Le Bail refinement plot for parent (a) fresh and (b) regenerated 4-times 2W-Z26 catalyst

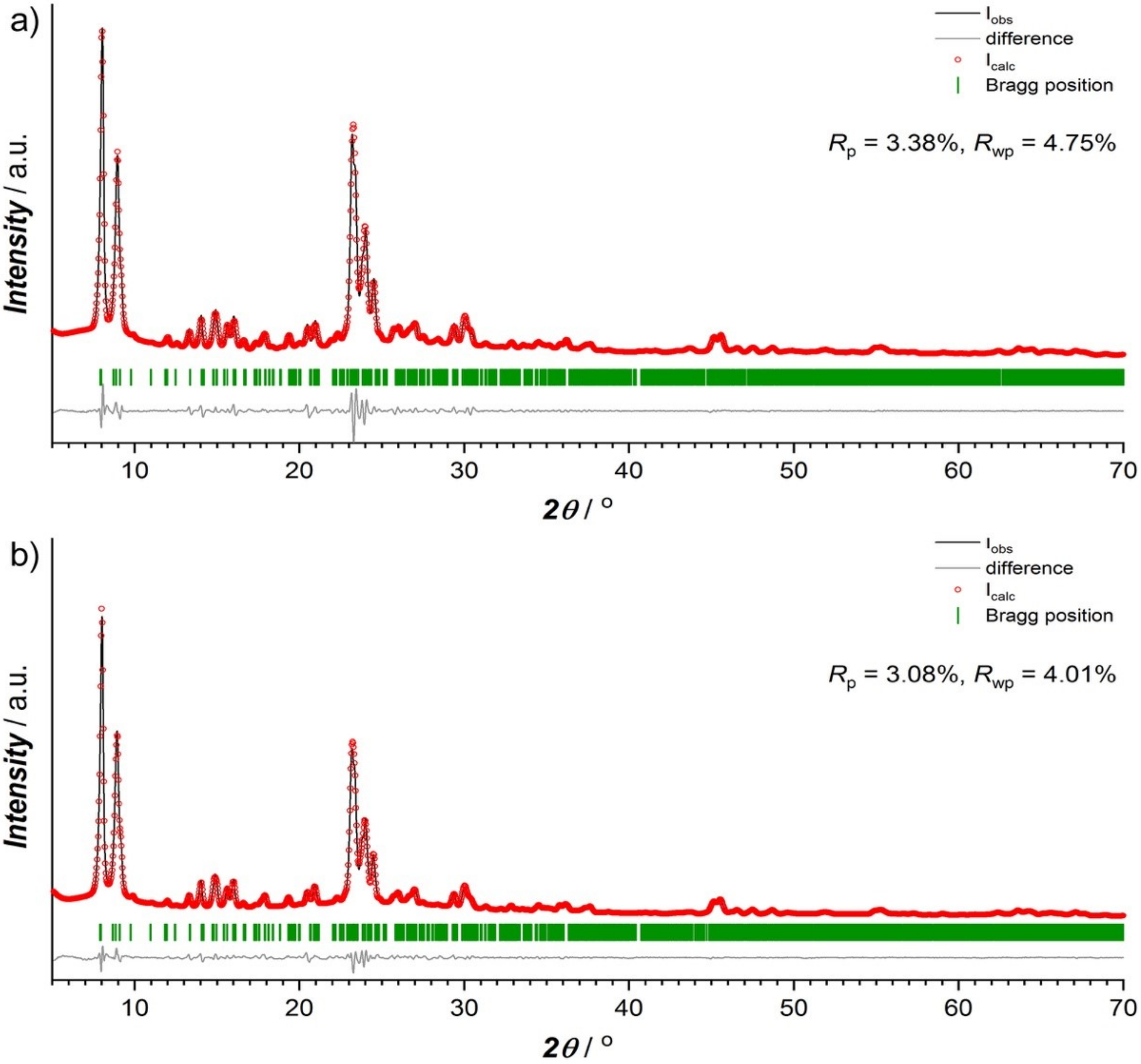

Figure S40. Le Bail refinement plot for parent (a) fresh and (b) regenerated 4-times 3W-Z26 catalyst

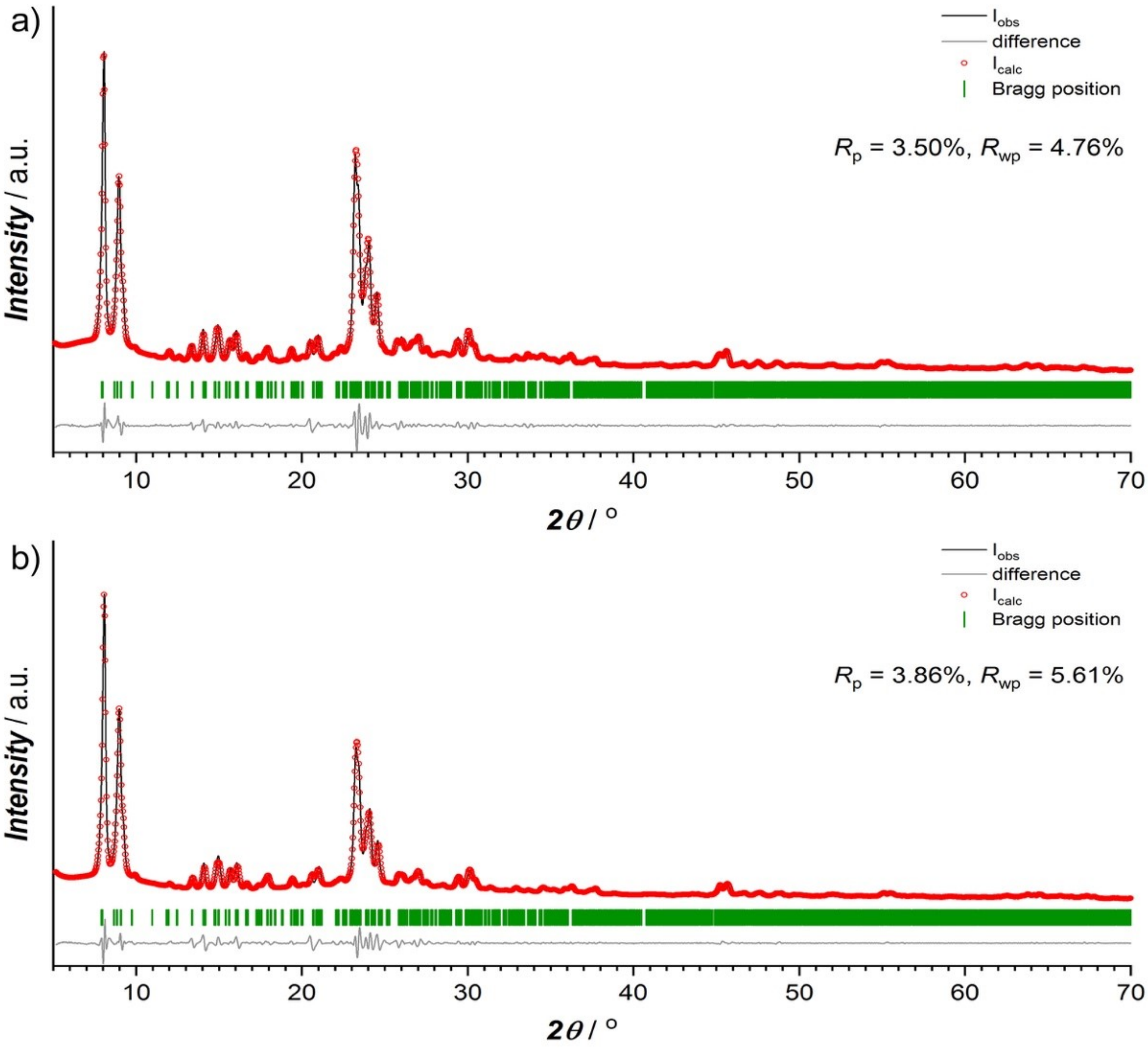

Figure S41. Le Bail refinement plot for parent (a) fresh and (b) regenerated 4-times 6W-Z26 catalyst

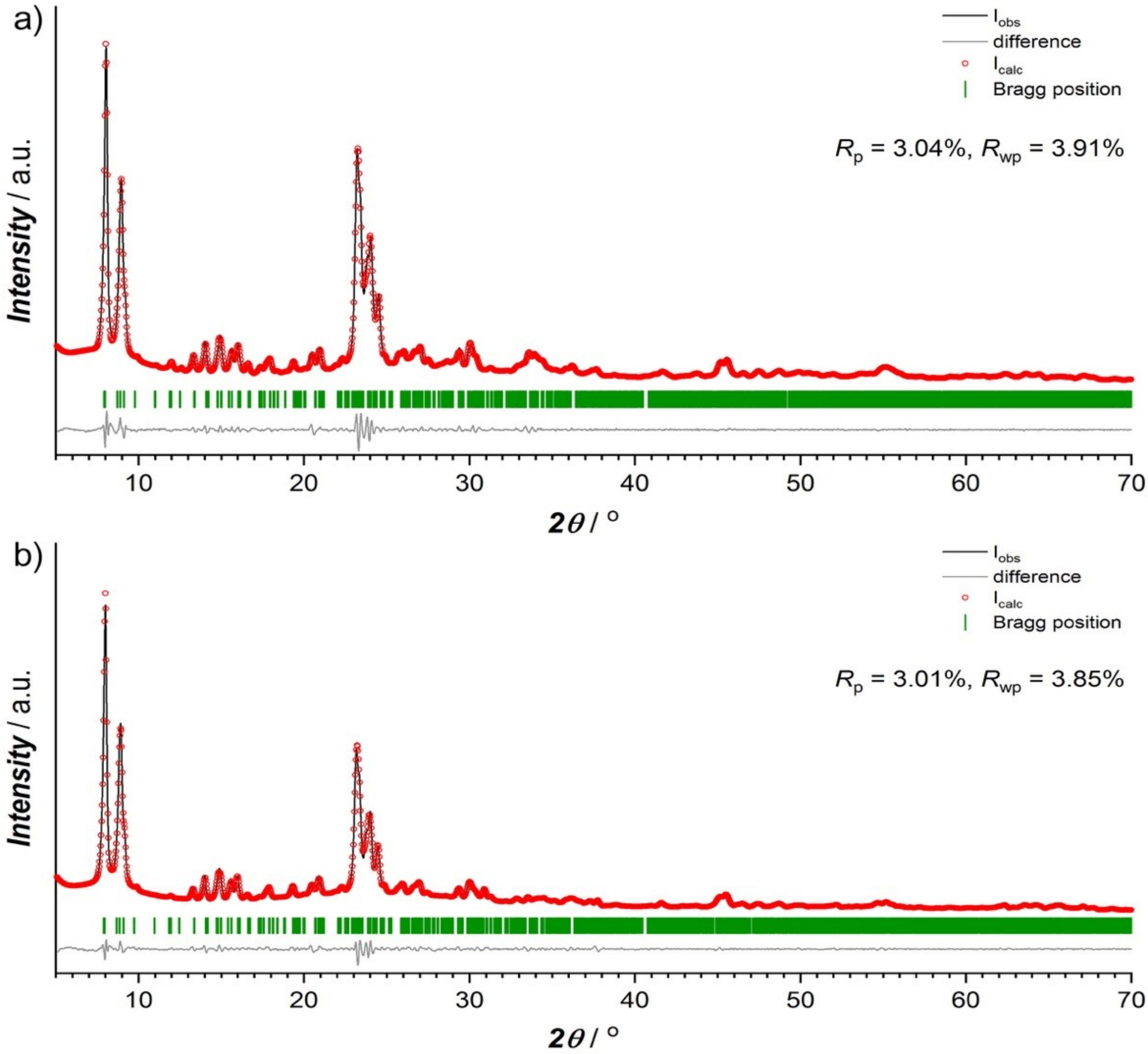

Figure S42. Le Bail refinement plot for parent (a) fresh and (b) regenerated 4-times 9W-Z26 catalyst

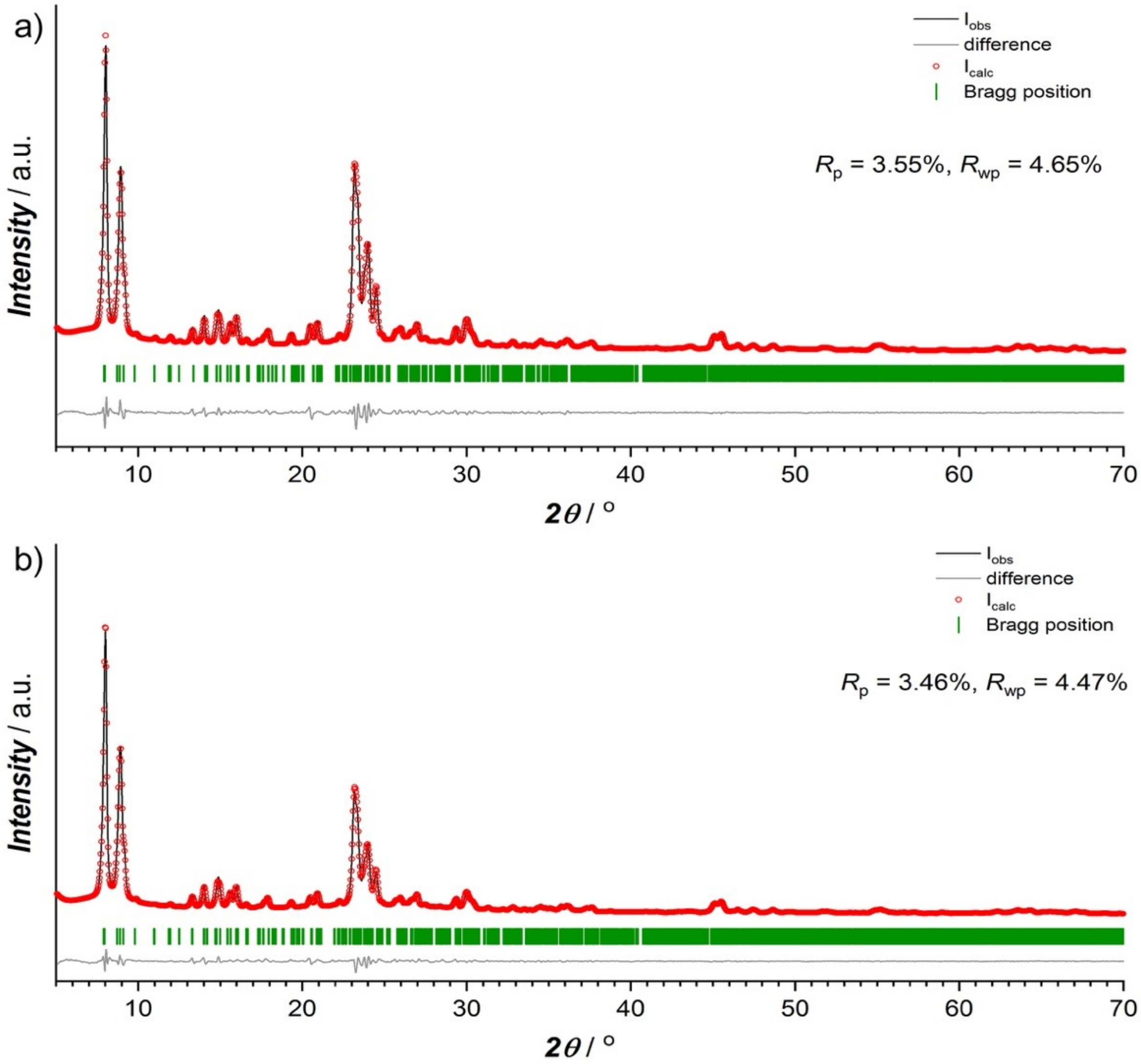

Figure S43. Le Bail refinement plot for parent (a) fresh and (b) regenerated 4-times 2Mo-Z26 catalyst

S4. *OPERANDO* XAS CATALYSIS

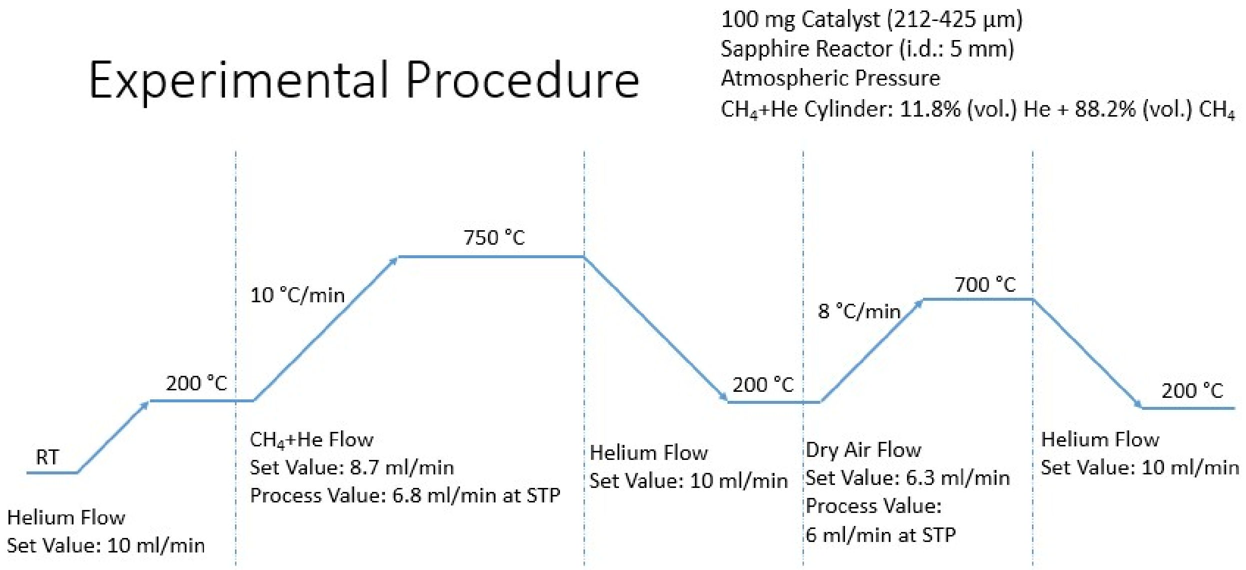

Figure S44. Reaction-Regeneration cycles and experimental parameters followed during *operando* XAS experiments

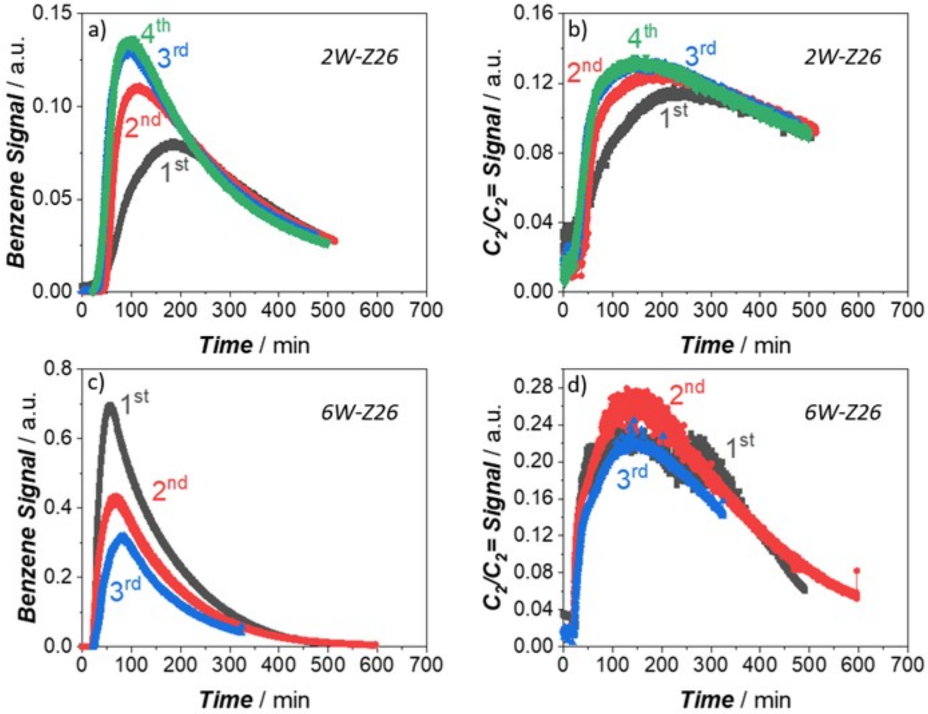

Figure S45. Benzene (a, c) and ethane/ethylene (b, d) signals at the reactor effluent during the *operando* XAS measurements: a, b) 2W- Z26, and c, d) 6W-Z26 (100 mg catalysts - Reaction at

750 °C: *11.8 mol% He and 88.2 mol%* CH_4 *in the inlet, Total Gas Flow= 8.7 ml/min at STP* – Regeneration at 700 °C: *Dry Air Flow= 6 ml/min at STP*)

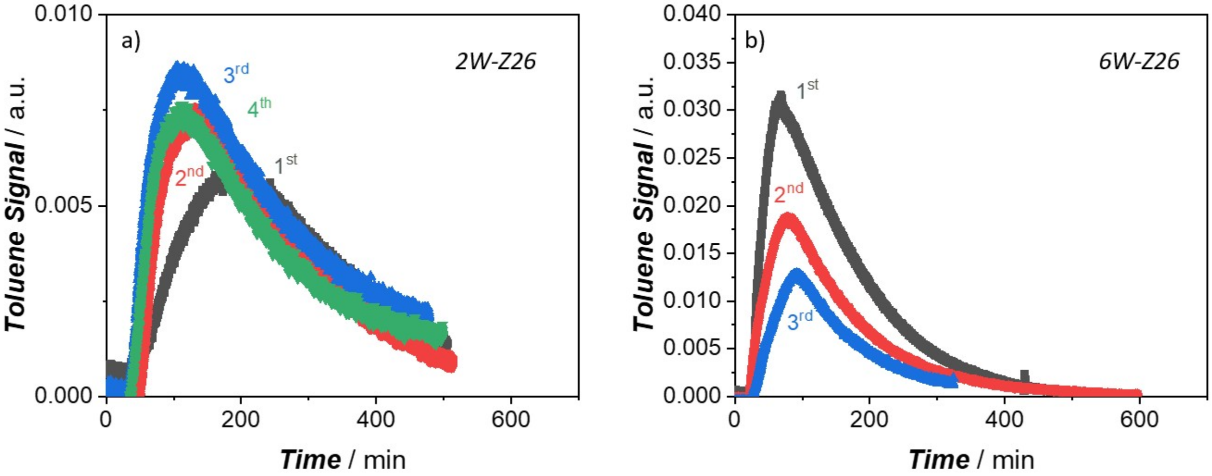

Figure S46. Toluene signals at the reactor effluent during the *operando* XAS measurements: a) 2W- Z26, and b) 6W-Z26 (100 mg catalysts - Reaction at 750 °C: *11.8 mol% He and 88.2 mol%* CH_4 *in the inlet, Total Gas Flow= 8.7 ml/min at STP* – Regeneration at 700 °C: *Dry Air Flow= 6 ml/min at STP*)

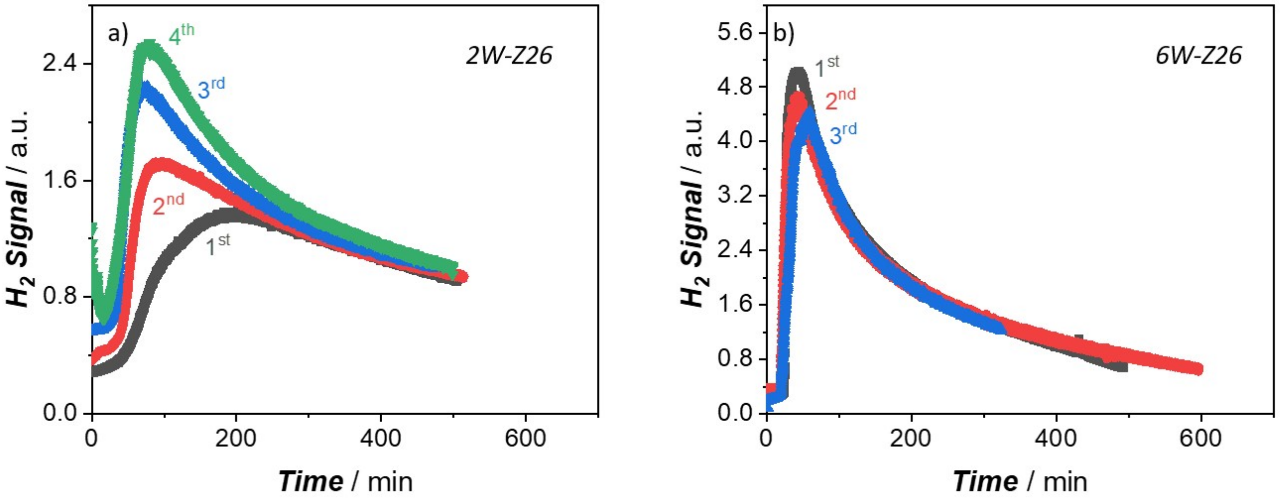

Figure S47. Hydrogen signals at the reactor effluent during the *operando* XAS measurements: a) 2W-Z26, and b) 6W-Z26 (100 mg catalysts - Reaction at 750 °C: *11.8 mol% He and 88.2 mol% CH_4 in the inlet, Total Gas Flow= 8.7 ml/min at STP* – Regeneration at 700 °C: *Dry Air Flow= 6 ml/min at STP*)

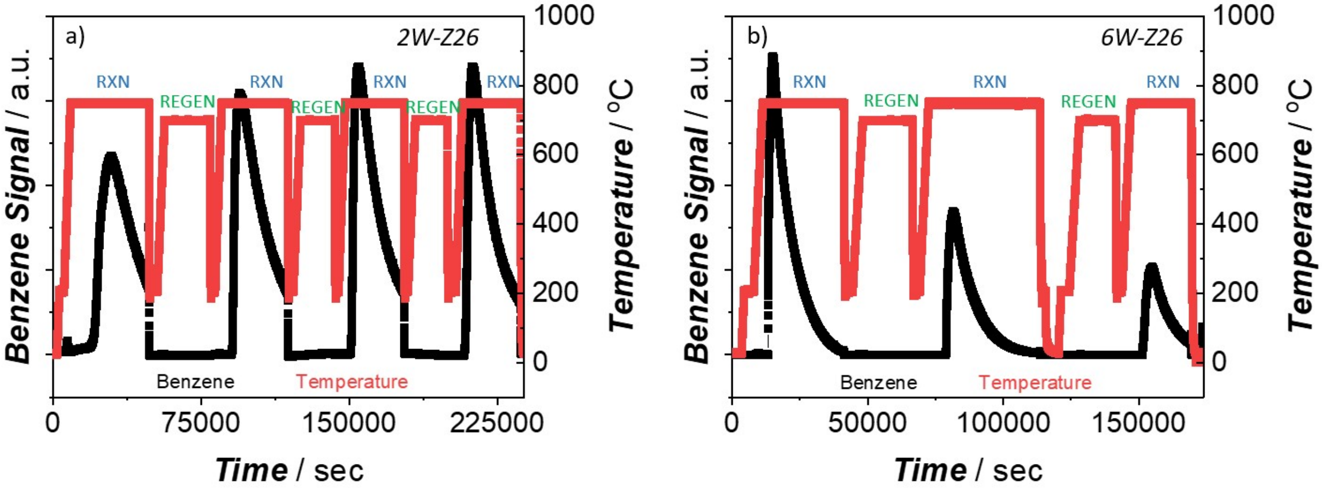

Figure S48. Comparison of cycles: benzene signals at the reactor effluent and the reactor temperature profiles during the *operando* XAS measurements: a) 2W-Z26, and b) 6W-Z26 (100 mg catalysts - Reaction at 750 °C: *11.8 mol% He and 88.2 mol% CH_4 in the inlet, Total Gas Flow= 8.7 ml/min at STP* – Regeneration at 700 °C: *Dry Air Flow= 6 ml/min at STP*): While the activation-induction period gets shorter along with the catalytic activity enhancement in the case of 2W-Z26 after each regeneration cycle, it gets longer in the case of 6W-Z26 sample with the decline in the catalytic activity.

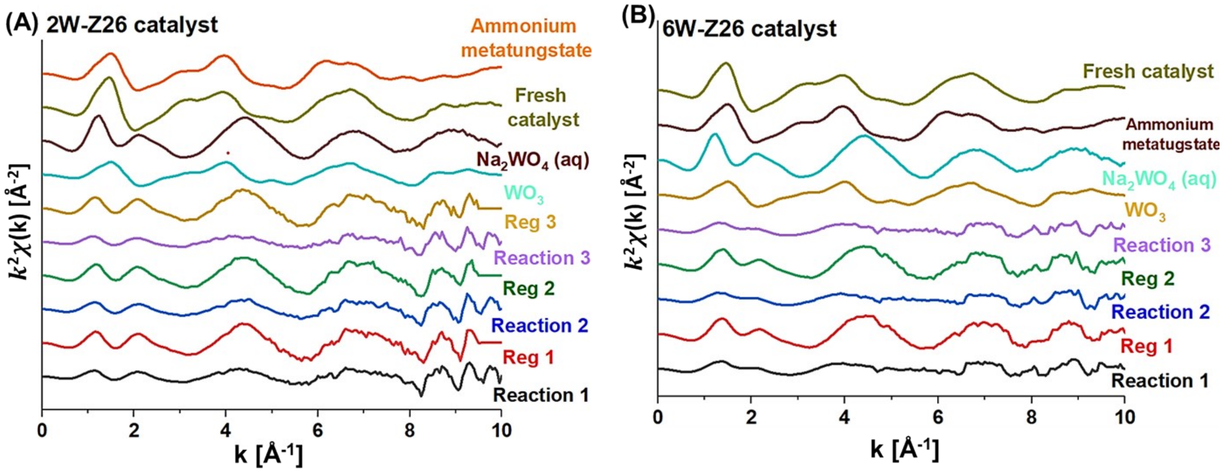

Figure S49. W L_3-edge EXAFS $k^3 \cdot \chi(k)$ functions of the experimental spectrum of 2W-Z26 and 6W-Z26 catalysts and W reference materials (WO_3, Na_2WO_4(aq), Ammonium meta tungstate $(NH_4)_6H_2W_{12}O_{40}$).

Continuous Cauchy wavelet transform was applied to decompose the EXAFS signal in reciprocal and real space simultaneously.[24] The wavelet transformation analysis was applied to the EXAFS data (WT-EXAFS) to perform relevant next nearest-neighbors. The backscattering amplitude from neighboring atoms shows a significant k-dependence that determines the envelope of EXAFS oscillations $\chi(k)$:[25] Lighter elements have their maximum backscattering amplitude at low wavenumbers while with increasing atomic number causes the maximum to shift towards higher k values. The WT correlates with the backscattering amplitudes of individual paths in k-space and with their interatomic distances in R-space without phase correction. Thus, it is a useful signal-processing tool for the qualitative assignment of the backscatter identity.

The wavelet transforms of the Fourier-filtered EXAFS for the a) WO_3, b) Na_2WO_4(aq), c) ammonium meta tungstate ($(NH_4)_6H_2W_{12}O_{40}$) and d) WC are shown in Figure S50. Here, all FT-EXAFS data are not corrected for scattering phase shift.

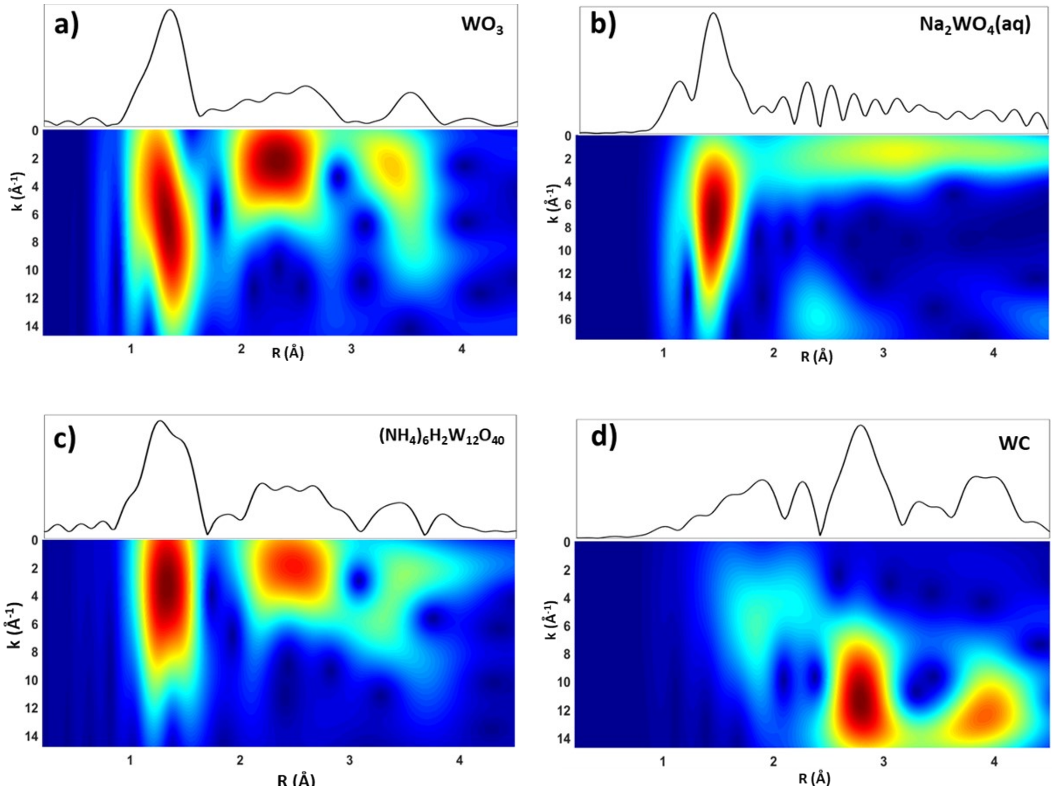

Figure S50. W L_3-edge for the references a) WO_3, b) Na_2WO_4*, c) Ammonium meta tungstate ($(NH_4)_6H_2W_{12}O_{40}$) and d) WC. *Obtained from the Solid Spectroscopy Hosting Architecture of Databases and Expertise database: https://www.sshade.eu/

Figure S51 shows the WT-EXAFS for the as-prepared 2W-Z26 (a) and 6W-Z26 (b) samples assigned as “fresh”.

The spectra of the fresh 2W-Z26 and 6W-Z26, (Figure S51a and b) exhibit a common feature: a peak with a maximum in the WT-EXAFS plot at the approximate coordinates (R ~ 1.3 Å, k ~ 5.5 Å-1). This WT maximum is assigned to oxygen by direct comparison with the FT-EXAFS $(NH_4)_6H_2W_{12}O_{40}$ in Figure S50c. This indicates that the initial state of W in both catalyst remains mostly in the form of polytungstates from the precursor ammonium according to the XANES spectra from Figure 7.

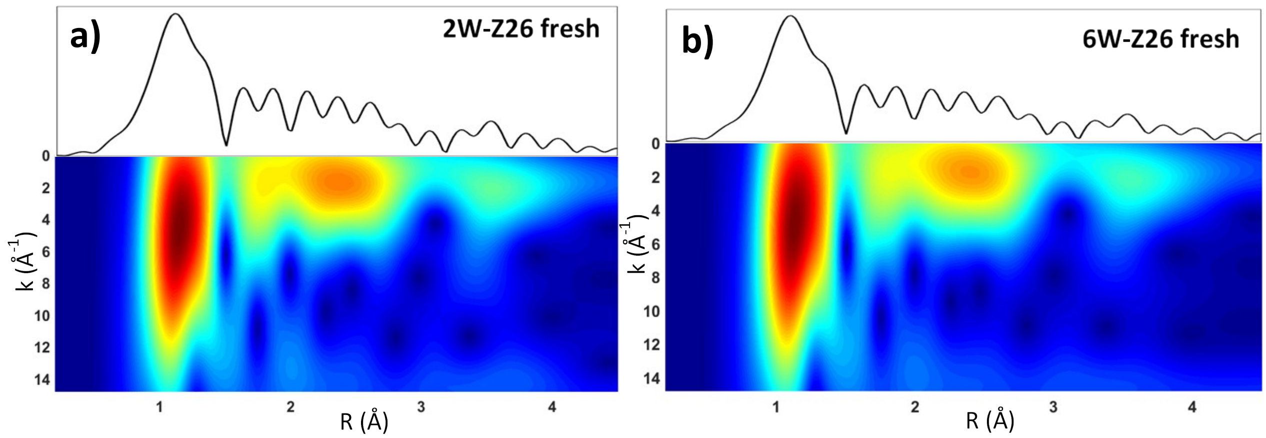

Figure S51. Contour plots of the wavelet transform magnitude showing the (k,R) localization of each FT-EXAFS contribution measured at the W L_3-edge for the a) 2W-Z26 and b) 6W-Z26 fresh catalysts.

The wavelet transform of the Fourier-filtered EXAFS during the different reaction-activation cycles for the 2W-Z26 and 6W-Z26 samples in Figures S52 and S53 respectively.

The WT-EXAFS spectra of the 2W-Z26 during the three reaction cycles (Figure S52a-c) exhibit a common feature: one prominent maxima in the WT-EXAFS plot at the approximate coordinates (R ~ 1.4 Å, k ~ 5.5 Å^{-1}) assigned to oxygen. During the regeneration cycles (Figure S52d-f) it is possible to observe the contribution to oxygen which can be related to mono tungstate species (Figure S50b) and accordingly with XANES in Figure 8a.

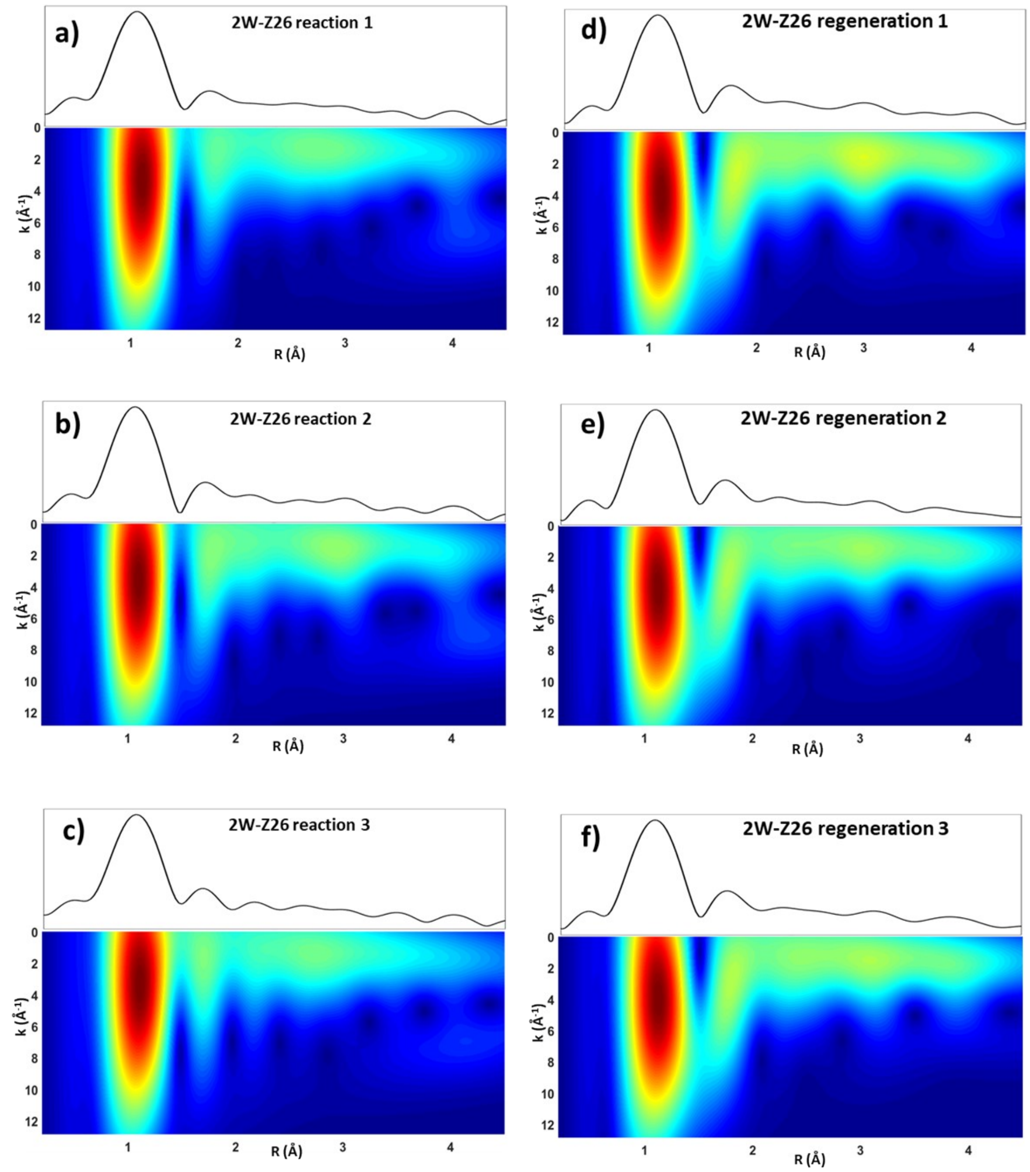

Figure S52. Contour plots of the wavelet transform magnitude showing the (k,R) localization of each FT-EXAFS contribution measured at the W L_3-edge for 2W-Z26 at a) Reaction 1, b) Reaction 2, c) Reaction 3, d) Regeneration 1, e) Regeneration 2 and f) Regeneration 3

The spectra of the 6W-Z26 during the three reaction 1, reaction 2 and reaction 3 steps are shown in Figure S53a-c. Under reaction conditions, the spectra exhibit peak with a maximum in the WT-EXAFS plot at the approximate coordinates (R ~ 1.4 Å, k ~ 5.5 $Å^{-1}$) assigned to oxygen and a second feature at the coordinates (R ~ 2 Å, k ~ 8 $Å^{-1}$) which could be associated to carbon comparing to the reference WC from Figure S50d. This may indicate the formation of coke in the sample during the reaction.

The spectra of the 6W-Z26 during the regeneration 1 and regeneration 2 steps are shown in Figure S53d and f. During the regeneration under air at 700 °C, the spectra exhibit a common peak with a maximum in the WT-EXAFS plot at the approximate coordinates (R ~ 1.4 Å, k ~ 5.5 Å-1) assigned to oxygen indicating the regeneration of the catalyst to mono tungstate species accordingly to XANES in Figure 8b.

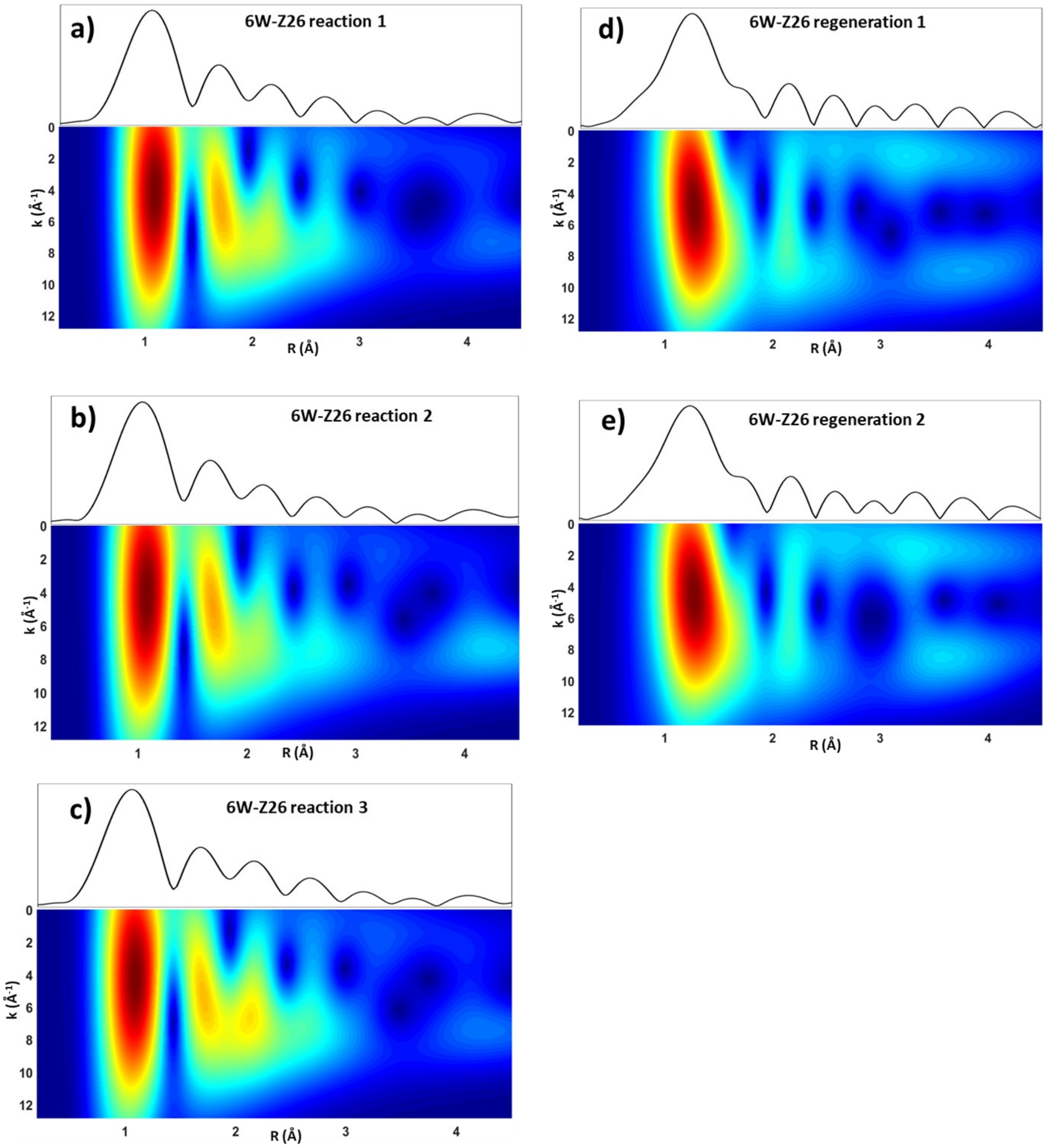

Figure S53. Contour plots of the wavelet transform magnitude showing the (k,R) localization of each FT-EXAFS contribution measured at the W L_3-edge for 6W-Z26 at a) Reaction 1, b) Reaction 2, c) Reaction 3, d) Regeneration 1 and e) Regeneration 2.

S5. COMPUTATIONAL ANALYSIS

S5.1. Computational Method:

The tungsten oxide doped ZSM-5 zeolites were simulated using a 137 atoms cluster model cut from a ZSM-5 unit cell and capped with hydrogen atoms to main a neutral charge, as previously employed.[7] To limit the computational expense, the initial geometric optimization was conducted with density functional theory using the generalized-gradient approximation (GGA) PBE functional[26] with Becke-Johson damped D3[27] dispersion correction as implemented in Gaussian 09[28] and an automatic density fitting set generated by the Gaussian program. In addition, the SVP basis set[29] was used for Al, Si, C, H, O atoms whereas the SDD[30] pseudopotential and its associated double-ζ basis set was employed for W atom (BS1 level). During the optimization process, all atoms were relaxed apart from the valence capping hydrogens that were kept fixed to simulate the bulk aspect of the zeolite lattice. Afterwards, the energy of the optimized models was further refined by doing single point calculations with PBE0-D3 using TZVP basis set[29] for Al, Si, C, H, O atoms and SDD basis set for W (BS2 level). In parallel, the local energy minimum was validated by analytic computation of vibrational frequencies at 998 K and 1073 K, which were also employed for the computation of thermochemical quantities. All minima were characterized by zero imaginary frequencies, while all frequencies below 50 cm^{-1} were replaced by 50 cm^{-1} when computing vibrational partition functions. Finally, Gibbs free energies were computed by adding Gibbs free energy contributions to single-point energies computed at BS2 level.

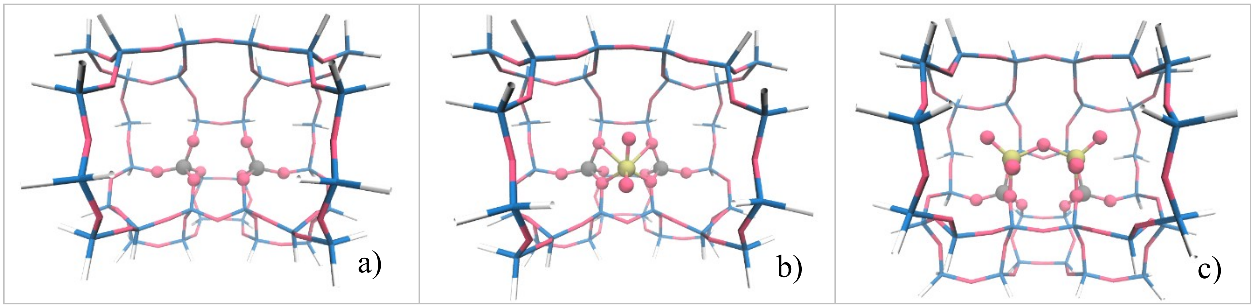

Figure S54. Illustrations of a) non-doped cluster model of ZSM-5 used for DFT calculations. b) Monomeric $[WoO_2]^{2+}$ inside the ZSM-5 framework. c) Dimeric $[W_2O_5]^{2+}$ inside the ZSM-5 framework, with color scheme as: Al atoms in grey, Si atoms in blue, W atom in yellow, O atoms in pink and H atoms in white.

S5.2. Thermodynamic Analysis: Following equations were used as we did in our previous publication[7].

The chemical potentials of gas-phase CH_4, CO, and H_2 are calculated assuming the ideal-gas behavior and given by:

$$\mu(T,p) = G(T,p_0) + \Delta\mu(T,p) \tag{1}$$

$$\Delta\mu(T,p) = \Delta\mu(T,p_0) + RTIn(\frac{p}{p_0}) \tag{2}$$

$$\Delta\mu(T,p) = \left(H(T,p_0) - H(T_0,p_0)\right) - T\left(S(T,p_0) - S(T_0,p_0)\right) + RTIn(\frac{p}{p_0}) \tag{3}$$

where R is the gas constant, T = 725 (or 800) °C and p is the corresponding partial pressure, T_0 = 298.15 K and p_0 = 1 atm.

The methane-reduction reactions for different chemical compositions between oxidized and reduced metal species (Mo or W) are indicated in equations (4) and (5) for monomeric and dimeric complexes, respectively. We considered a total pressure of 1 atm and thus partial pressure of CH_4 is calculated for varying H_2 with CO partial pressure fixed at either $P_{CO} = 10^{-1.5}$ or $P_{CO} = 10^{-15}$ atm so as to evaluate the impact of CO at both high and low concentrations (where $P_{N2} = 0.11$ atm) as shown in equation (6).

$$MO_2 + (2 - x + y)CH_4 \leftrightarrow MO_xC_yH_z + (2 - x)CO + 2(2 - x + y - \frac{z}{4})H_2 \tag{4}$$

$$M_2O_5 + (5 - x + y)CH_4 \leftrightarrow M_2O_xC_yH_z + (5 - x)CO + 2(5 - x + y - \frac{z}{4})H_2 \tag{5}$$

$$P_{CH4} = 1.0 - P_{N2} - P_{CO} - P_{H2} \qquad (6)$$

The standard-state Gibbs free energy of reaction *ΔG(T,p)* for monomeric and dimeric reduction reactions with respect to the initial state is calculated as follows :

$$\Delta G(T{,}p) = G_{MO_xC_yH_z} + (2-x) * \mu_{CO}^{g} + 2\left(2-x+y-\frac{z}{4}\right) * \mu_{H_2}^{g} - G_{MO_2} - (2-x+y) * \mu_{CH_4}^{g} \qquad (7)$$

$$\Delta G(T{,}p) = G_{M_2O_xC_yH_z} + (5-x) * \mu_{CO}^{g} + 2\left(5-x+y-\frac{z}{4}\right) * \mu_{H_2}^{g} - G_{M_2O_5} - (5-x+y) * \mu_{CH_4}^{g} \qquad (8)$$

In this study, we also showed the Gibbs free energy values for each reaction step.

In the case of carbene coupling to ethylene, we didn't include the gas phase composition in equation (2).

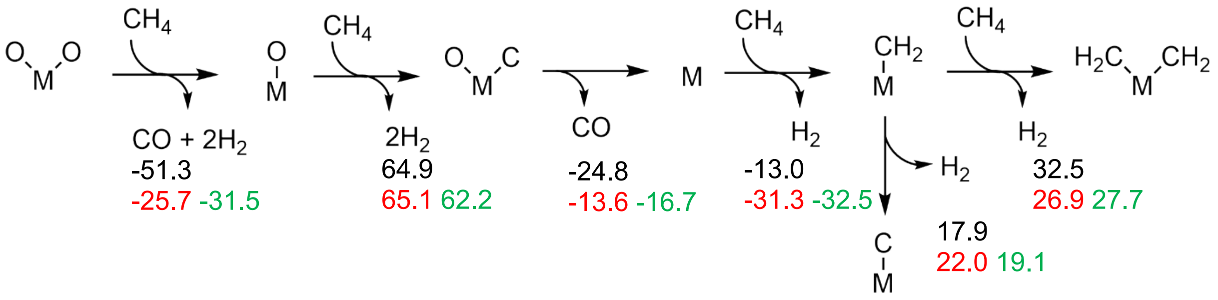

Figure S55. Illustration of methane activation over monomeric oxide species of Mo (top) and W (bottom), with Gibbs reaction free energies provided in kcal/mol at 998 K (Mo - black, W - red) and 1073 K (W - green) and partial pressures as P_{CO}: $10^{-1.5}$ atm, P_{H2}: $10^{-1.5}$ atm, P_{N2}: 0.11 atm, and P_{CH4}: 1 - P_{CO} - P_{H2} - P_{N2} atm

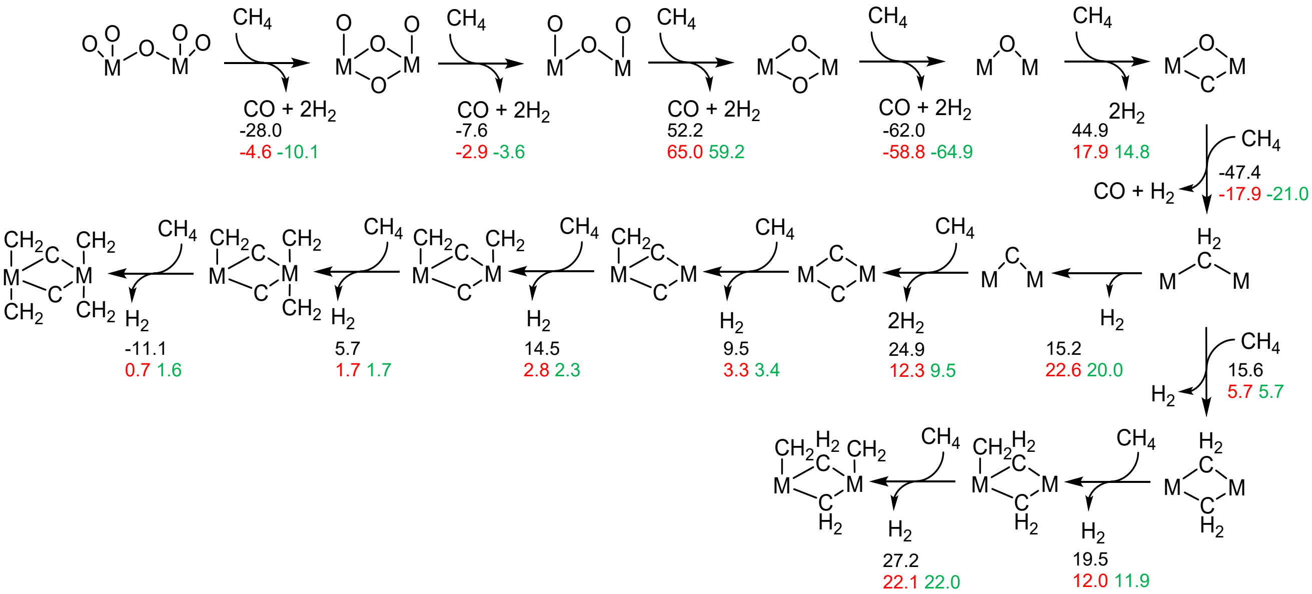

Figure S56. Illustration of methane activation over dimeric oxide species of Mo (top) and W (bottom), with Gibbs reaction free energies provided in kcal/mol at 998 K (Mo - black, W - red) and 1073 K (W - green) and partial pressures as P_{CO}: $10^{-1.5}$ atm, P_{H2}: $10^{-1.5}$ atm, P_{N2}: 0.11 atm, and P_{CH4}: 1 - P_{CO} - P_{H2} - P_{N2} atm

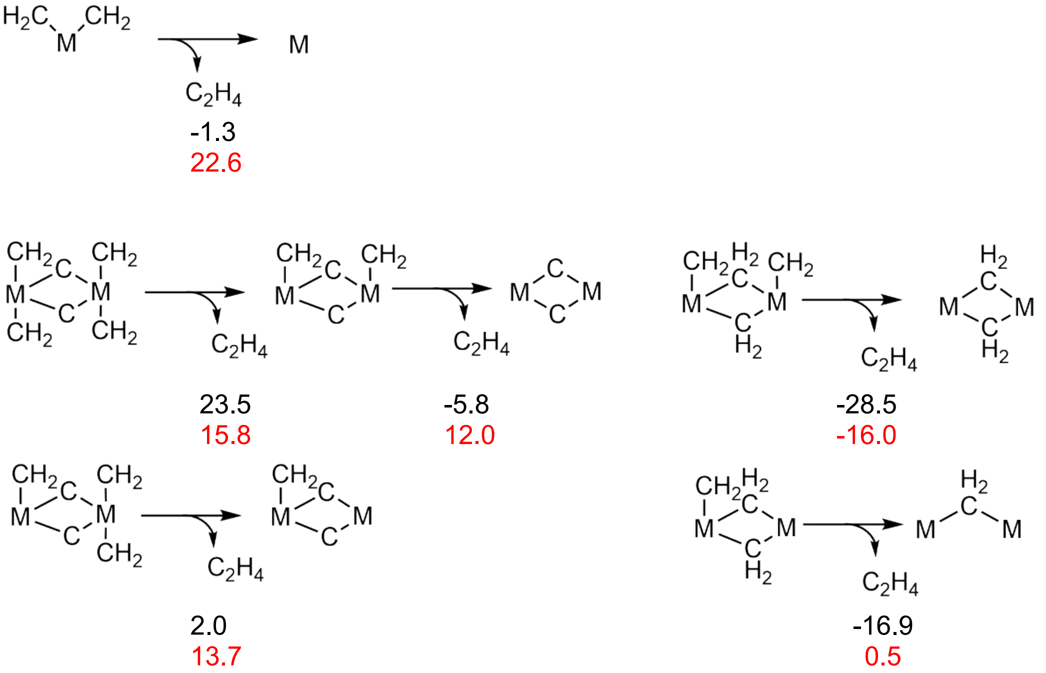

Figure S57. Illustration of ethylene formation via carbene species on Mo (black) and W (red), with Gibbs reaction free energies provided in kcal/mol at 998 K.

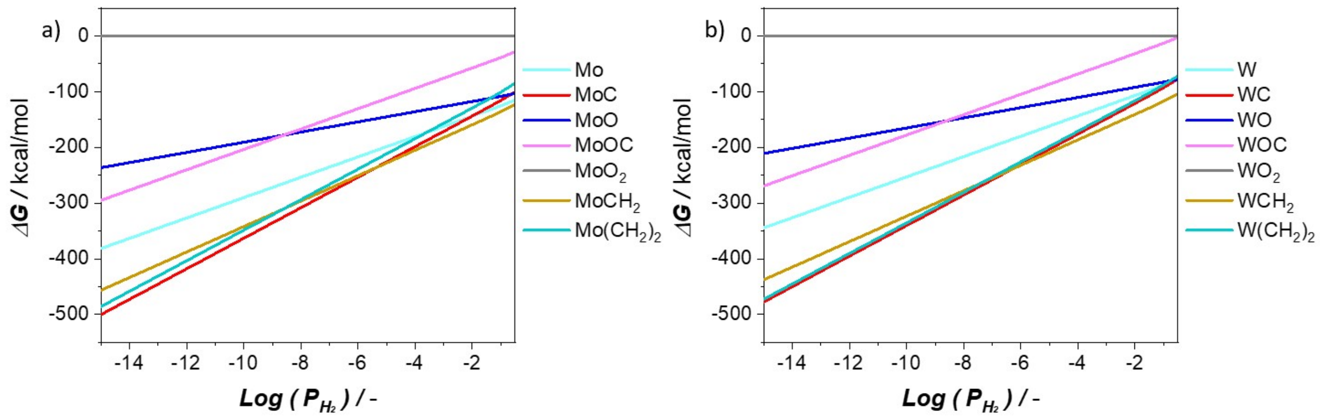

Figure S58. Reduction/carburization free energies of monomeric Mo (a) and W (b) species with respect to MO_2 as a function of H_2 partial pressures ($P_{CO} = 10^{-15}$) at 725 °C

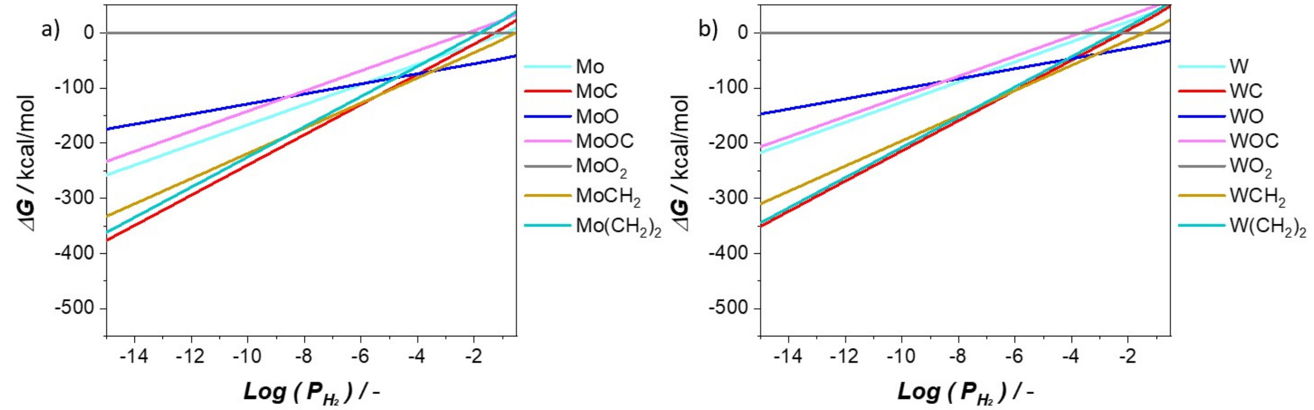

Figure S59. Reduction/carburization free energies of monomeric Mo (a) and W (b) species with respect to MO_2 as a function of H_2 partial pressures ($P_{CO} = 10^{-1.5}$) at 725 °C

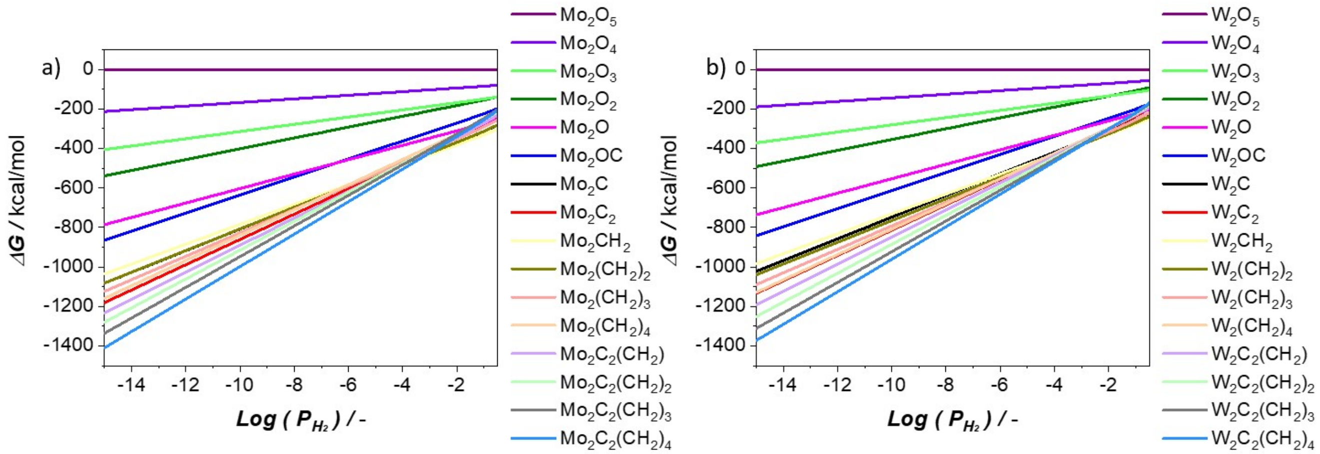

Figure S60. Reduction/carburization free energies of dimeric Mo (a) and W (b) species with respect to M_2O_5 as a function of H_2 partial pressures ($P_{CO} = 10^{-15}$) at 725 °C

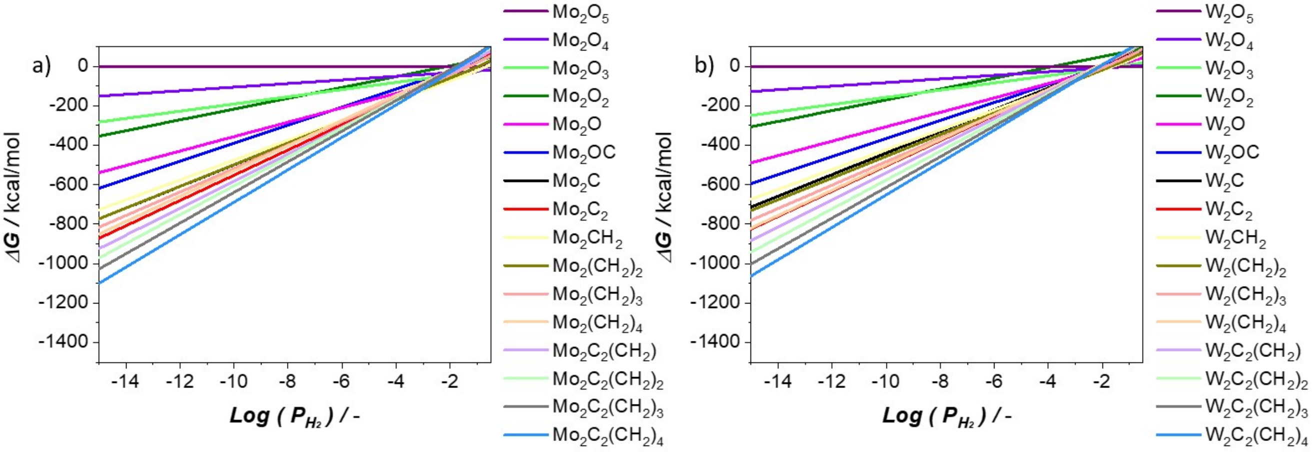

Figure S61. Reduction/carburization free energies of dimeric Mo (a) and W (b) species with respect to M_2O_5 as a function of H_2 partial pressures ($P_{CO} = 10^{-1.5}$) at 725 °C

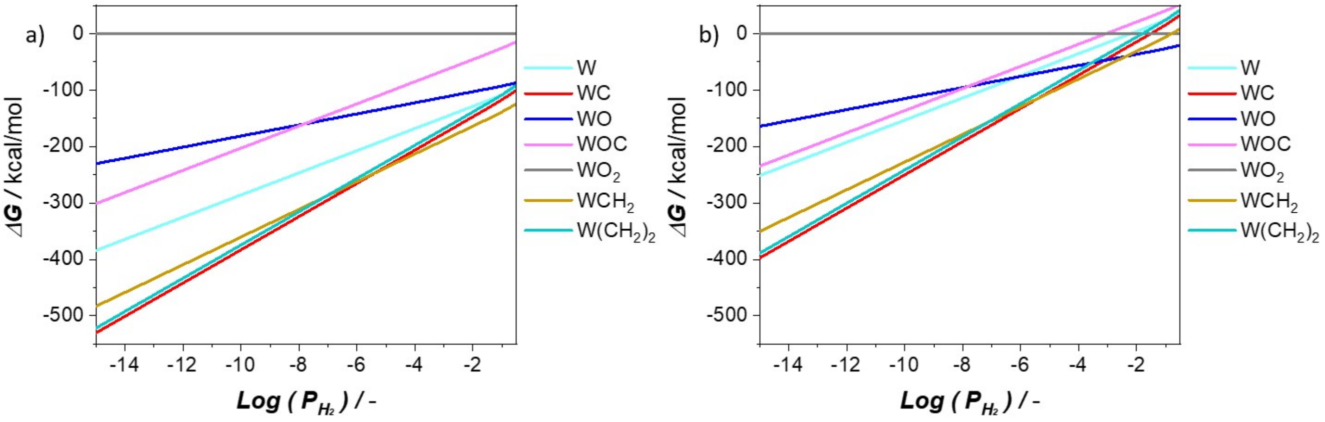

Figure S62. Reduction/carburization free energies of monomeric W species with respect to MO_2 as a function of H_2 partial pressures (a: $P_{CO} = 10^{-15}$ and b: $P_{CO} = 10^{-1.5}$) at 800 °C

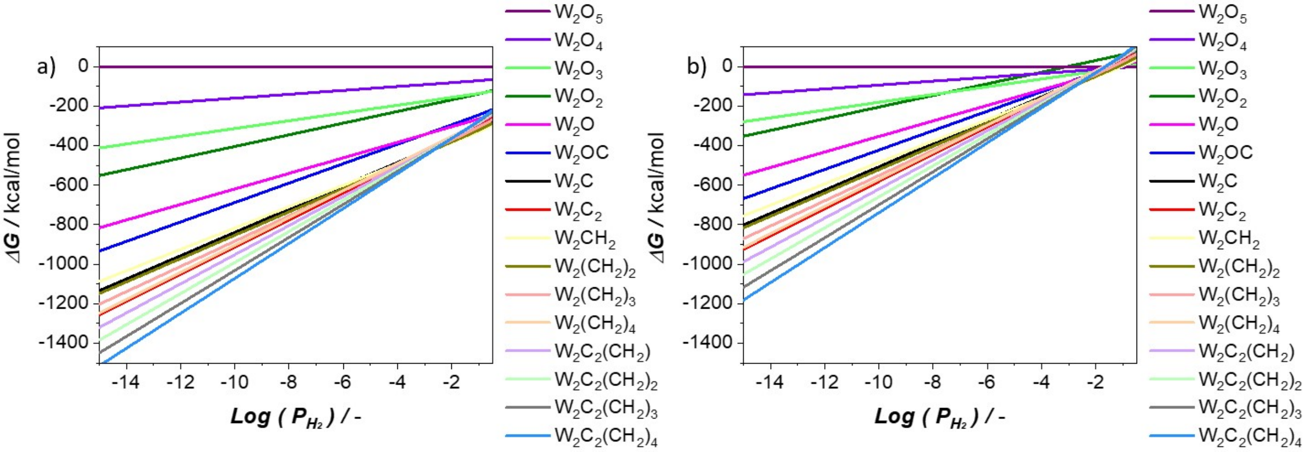

Figure S63. Reduction/carburization free energies of dimeric W species with respect to M_2O_5 as a function of H_2 partial pressures (a: $P_{CO} = 10^{-15}$ and b: $P_{CO} = 10^{-1.5}$) at 800 °C

Table S6. Energies for monomeric species in Hartrees.

Species	E(BS2)[a]	G_{corr} (BS1)[b]	G_{corr} (BS1)[c]
MoO_2	-15137.93296	-0.572375	-
WO_2	-15136.86343	-0.575485	-0.693416
MoO	-15062.77928	-0.561395	-
WO	-15061.66975	-0.563757	-0.680032
MoOC	-15100.73468	-0.569129	-
WOC	-15099.62542	-0.570856	-0.688445
MoC	-15025.52454	-0.564659	-
WC	-15024.423	-0.563432	-0.681585
Mo	-14987.47543	-0.555001	-
W	-14986.3473	-0.557694	-0.672724
$MoCH_2$	-15026.7879141	-0.548893	-
WCH_2	-15025.69084	-0.549704	-0.668862
$Mo(CH_2)_2$	-15066.0265412	-0.544083	-
$W(CH_2)_2$	-15064.93846	-0.544911	-0.664891

[a] E(BS2) : electronic energy at BS2 level, [b] G_{corr} (BS1) : Gibbs free energy correction at 725 °C at BS1 level, [c] G_{corr} (BS1) : Gibbs free energy correction at 800 °C at BS1 level.

Table S7. Energies for dimeric species in Hartrees.

Species	E(BS2)[a]	G_{corr} (BS1)[b]	G_{corr} (BS1)[c]
Mo_2O_5	-15431.82324	-0.610084	-
W_2O_5	-15429.68551	-0.613995	-0.73788
Mo_2O_4	-15356.64053	-0.590952	-
W_2O_4	-15354.46455	-0.595896	-0.717669
Mo_2O_3	-15281.40401	-0.593197	-
W_2O_3	-15279.21175	-0.597684	-0.718799
Mo_2O_2	-15206.08608	-0.581556	-
W_2O_2	-15203.87263	-0.586775	-0.706249
Mo_2O	-15130.94189	-0.578203	-
W_2O	-15128.72402	-0.582619	-0.701028
Mo_2OC	-15168.92352	-0.591574	-
W_2OC	-15166.75257	-0.592096	-0.712017
Mo_2C	-15093.74376	-0.576356	-
W_2C	-15091.51013	-0.580556	-0.698826
Mo_2C_2	-15131.76371	-0.583252	-
W_2C_2	-15129.55139	-0.586224	-0.705688
Mo_2CH_2	-15094.99839	-0.564949	-
W_2CH_2	-15092.77501	-0.570823	-0.690403
$Mo_2(CH_2)_2$	-15134.26832	-0.555849	-
$W_2(CH_2)_2$	-15132.0624	-0.560042	-0.681808
$Mo_2(CH_2)_3$	-15173.53393	-0.544858	-
$W_2(CH_2)_3$	-15171.33665	-0.552296	-0.676383
$Mo_2(CH_2)_4$	-15212.78245	-0.538654	-
$W_2(CH_2)_4$	-15210.59461	-0.544683	-0.671189

$Mo_2C_2(CH_2)$	-15171.04487	-0.572649	-
$W_2C_2(CH_2)$	-15168.84302	-0.574912	-0.696485
$Mo_2C_2(CH_2)_2$	-15210.30638	-0.573739	-
$W_2C_2(CH_2)_2$	-15208.12397	-0.575182	-0.69969
$Mo_2C_2(CH_2)_3$	-15249.59197	-0.564629	-
$W_2C_2(CH_2)_3$	-15247.418	-0.564079	-0.690775
$Mo_2C_2(CH_2)_4$	-15288.9302	-0.529774	-
$W_2C_2(CH_2)_4$	-15286.7355	-0.531101	-0.658506

[a] E(BS2) : electronic energy at BS2 level, [b] G_{corr} (BS1) : Gibbs free energy correction at 725 °C at BS1 level, [c] G_{corr} (BS1) : Gibbs free energy correction at 800 °C at BS1 level.

S3. REFERENCES

1 J. Rodríguez-Carvajal, *Newsl. Comm. Powder Diffr. IUCr*, 2001, 26.

2 S. Sartipi, K. Parashar, M. J. Valero-Romero, V. P. Santos, B. van der Linden, M. Makkee, F. Kapteijn and J. Gascon, *J Catal*, , DOI:10.1016/j.jcat.2013.05.012.

3 C. A. Emeis, *J Catal*, , DOI:10.1006/jcat.1993.1145.

4 O. Proux, X. Biquard, E. Lahera, J. J. Menthonnex, A. Prat, O. Ulrich, Y. Soldo, P. Trévisson, G. Kapoujyan, G. Perroux, P. Taunier, D. Grand, P. Jeantet, M. Deleglise, J. P. Roux and J. L. Hazemann, *Physica Scripta T*, 2005, **T115**, 970–973.

5 A. Aguilar-Tapia, S. Ould-Chikh, E. Lahera, A. Prat, W. Delnet, O. Proux, I. Kieffer, J. M. Basset, K. Takanabe and J. L. Hazemann, *Review of Scientific Instruments*, , DOI:10.1063/1.4998929.

6 B. Ravel and M. Newville, *J Synchrotron Radiat*, 2005, **12**, 537–541.

7 M. Çağlayan, A. L. Paioni, B. Dereli, G. Shterk, I. Hita, E. Abou-Hamad, A. Pustovarenko, A.-H. Emwas, A. Dikhtiarenko, P. Castaño, L. Cavallo, M. Baldus, A. D. Chowdhury and J. Gascon, *ACS Catal*, 2021, **11**, 11671–11684.

8 S. Lwin, Y. Li, A. I. Frenkel and I. E. Wachs, *ACS Catal*, 2016, **6**, 3061–3071.

9 E. I. Ross-Medgaarden and I. E. Wachs, *Journal of Physical Chemistry C*, 2007, **111**, 15089–15099.

10 C. Y. Su, H. C. Lin, T. K. Yang, C. H. Chang and C. K. Lin, *Mater Trans*, 2009, **50**, 2593–2597.

11 J. J. Wiesfeld, R. Gaquere and E. J. M. Hensen, *ACS Sustain Chem Eng*, 2019, **7**, 7552–7562.

12 S. Boonpai, S. Wannakao, J. Panpranot, B. Jongsomjit and P. Praserthdam, *The Journal of Physical Chemistry C*, 2020, **124**, 15935–15943.

13 S. Watmanee, K. Suriye, P. Praserthdam and J. Panpranot, *Top Catal*, , DOI:10.1007/s11244-018-1020-4.

14 M. A. Alvarez-Merino, F. Carrasco-Marín, J. L. G. Fierro and C. Moreno-Castilla, *J Catal*, 2000, **192**, 363–373.

15 T. Kim, A. Burrows, C. J. Kiely and I. E. Wachs, *J Catal*, 2007, **246**, 370–381.

16 A. A. Costa, P. R. S. Braga, J. L. De MacEdo, J. A. Dias and S. C. L. Dias, *Microporous and Mesoporous Materials*, 2012, **147**, 142–148.

17 A. Guntida, K. Suriye, J. Panpranot and P. Praserthdam, *Catal Today*, 2020, **358**, 354–369.

18 N. Liu, S. Ding, Y. Cui, N. Xue, L. Peng, X. Guo and W. Ding, *Chemical Engineering Research and Design*, 2013, **91**, 573–580.

19 A. I. Olivos-Suarez, À. Szécsényi, E. J. M. Hensen, J. Ruiz-Martinez, E. A. Pidko and J. Gascon, *ACS Catal*, 2016, **6**, 2965–2981.

20 M. Çağlayan, A. Lucini Paioni, E. Abou-Hamad, G. Shterk, A. Pustovarenko, M. Baldus, A. D. Chowdhury and J. Gascon, *Angewandte Chemie - International Edition*, 2020, **59**, 16741–16746.

21 S. Bordiga, C. Lamberti, F. Bonino, A. Travert and F. Thibault-Starzyk, *Chem Soc Rev*, 2015, **44**, 7262–7341.

22 S. M. T. Almutairi, B. Mezari, E. A. Pidko, P. C. M. M. Magusin and E. J. M. Hensen, *J Catal*, 2013, **307**, 194–203.

23 A. S. Al-Dughaither and H. De Lasa, *Ind Eng Chem Res*, 2014, **53**, 15303–15316.

24 M. Munoz, P. Argoul and F. Farges, *American Mineralogist*, 2003, **88**, 694–700.

25 D. Friebel, D. J. Miller, C. P. O'Grady, T. Anniyev, J. Bargar, U. Bergmann, H. Ogasawara, K. T. Wikfeldt, L. G. M. Pettersson and A. Nilsson, *Physical Chemistry Chemical Physics*, 2011, **13**, 262–266.

26 J. P. Perdew, K. Burke and M. Ernzerhof, *Phys Rev Lett*, 1996, **77**, 3865–3868.

27 S. Grimme, S. Ehrlich and L. Goerigk, *J Comput Chem*, 2011, **32**, 1456–1465.

28 G. M. J. Frisch, W. Trucks, H. B. ; Schlegel, G. E. ; Scuseria, M. A. ; Robb, J. R. Cheeseman, G. Scalmani, V. ; Barone, B. ; Mennucci, G. A. Petersson, H. Nakatsuji, M. ; Caricato, X. ; Li, H. P. ; Hratchian, A. F. ; Izmaylov, J. ; Bloino, G. ; Zheng, J. L. ; Sonnenberg, M. J. Frisch, G. W. ; Trucks, H. B. ; Schlegel, G. E. ; Scuseria, M. A. ; Robb, G. ; Cheeseman, J. R.; Scalmani, V. ; Barone, B. ; Mennucci, H. ; Petersson, G. A.; Nakatsuji, M. ; Caricato, X. ; Li, H. P. ; Hratchian, A. F. ; Izmaylov, J. ; Bloino, G. ; Zheng, J. L. ; Sonnenberg, K. ; Hada, M.; Ehara, M.; Toyota, R. ; Fukuda, J. ; Hasegawa, M. ; Ishida, T. ; Nakajima, Y. ; Honda, O. ; Kitao, H. ; Nakai, T. ; Vreven, J. E. ; Montgomery, J. A., Jr.; Peralta, F. ; Ogliaro, M. ; Bearpark, J. J. ; Heyd, E. ; Brothers, K. N. ; Kudin, R. ; Staroverov, V. N.; Kobayashi, K. ; Normand, J.; Raghavachari, A. ; Rendell, J. C. ; Burant, S. S. ; Iyengar, J. ; Tomasi, M. ; Cossi, N. ; Rega, J. M. ; Millam, M. ; Klene, J. E. ; Knox, J. B. ; Cross, V. ; Bakken, C. ; Adamo, J. ; Jaramillo, R. ; Gomperts, R. E. ; Stratmann, O. ; Yazyev, A. J. ; Austin, R. ; Cammi, C. ; Pomelli, J. W. ; Ochterski, R. L. ; Martin, K. ; Morokuma, V. G. ; Zakrzewski, G. A. ; Voth, P. ; Salvador, S. ; Dannenberg, J. J.; Dapprich, A. D. ; Daniels, Ö. ; Farkas, J. B. ; Foresman, J. V. ; Ortiz, J. ; Cioslowski and D. J. Fox, *Gaussian, Inc.: Wallingford, CT*, 2009.

29 A. Schäfer, H. Horn and R. Ahlrichs, *J Chem Phys*, 1992, **97**, 2571–2577.

30 D. Andrae, U. Häußermann, M. Dolg, H. Stoll and H. Preuß, *Theor Chim Acta*, 1990, **77**, 123–141.